

O(N) PARALLEL TIGHT-BINDING MOLECULAR-DYNAMICS COMPUTER
SIMULATION: APPLICATION TO CARBON NANOTUBES

A THESIS SUBMITTED TO
THE GRADUATE SCHOOL OF NATURAL AND APPLIED SCIENCES
OF
THE MIDDLE EAST TECHNICAL UNIVERSITY

119 468
BY

CEM ÖZDOĞAN

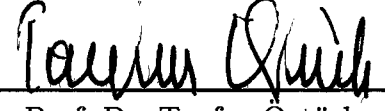
119468

**T.C. YÜKSEKÖĞRETİM KURULU
DOKÜMANTASYON MERKEZİ**

IN PARTIAL FULFILLMENT OF THE REQUIREMENTS FOR THE DEGREE OF
DOCTOR OF PHILOSOPHY
IN
THE DEPARTMENT OF PHYSICS

June 2002

Approval of the Graduate School of Natural and Applied Sciences.



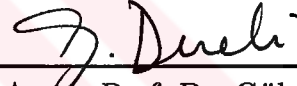
Prof. Dr. Tayfur Öztürk
Director

I certify that this thesis satisfies all the requirements as a thesis for the degree of Doctor of Philosophy.



Prof. Dr. Sinan Bilikmen
Head of Department

This is to certify that we have read this thesis and that in our opinion it is fully adequate, in scope and quality, as a thesis for the degree of Doctor of Philosophy.



Assoc. Prof. Dr. Gülay Dereli
Supervisor

Examining Committee Members

Assoc. Prof. Dr. Gülay Dereli



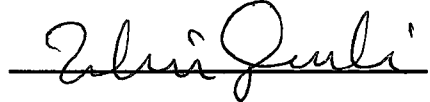
Prof. Dr. Şinasi Ellialtıođlu



Prof. Dr. Tacettin Altanhan



Prof. Dr. Tekin Dereli



Prof. Dr. Demet Gülen



ABSTRACT

O(N) PARALLEL TIGHT-BINDING MOLECULAR-DYNAMICS
COMPUTER SIMULATION: APPLICATION TO CARBON NANOTUBES

Özdoğan, Cem

Ph. D., Department of Physics

Supervisor: Assoc. Prof. Dr. Gülay Dereli

June 2002, 119 pages

It is aimed to develop an $O(N)$ Parallel Tight-Binding Molecular Dynamics (TBMD) algorithm in the simulations of Single Wall Carbon Nanotubes (SWCNT). Traditional TB solves the Schrödinger equation by direct matrix diagonalization, which results in cubic scaling with respect to the number of atoms, namely, Order- N^3 ($O(N^3)$) TBMD. The main limitation of this method is the increasing simulation time with system size. It is needed to speed up the simulations by applying some computational techniques. We have applied $O(N)$ (Divide and Conquer scheme) technique in Carbon nanotube simulation and parallelized our $O(N)$ TBMD program. We have approved that parallelization technique is beneficial by obtaining speed up and efficiency values

for different number of processors. Benchmark tests have been performed on distributed memory system having 8 PCs using Parallel Virtual Machine (PVM) library.

We have applied our developed $O(N)$ parallel TBMD technique to 10x10 and 17x0 structured CNTs. These tube structures are chosen because they have different chirality but similar diameter. We have found the Fermi energy (around 3.7 eV) very similar for both tube structures since they have the same radii. On the other hand density of states (DOS) results show that 10x10 tube has metallic behavior and 17x0 tube has semiconductor behavior as expected. Next, the structural stability and energetics of 10x10 and 17x0 tubes are investigated. Elastic properties under uniaxial strain are studied at room temperature. The Young's modulus, tensile strength, Poisson ratio and frequency of vibrations are calculated. We have observed disintegrations under large strains. These are shown in graphs of total energy, radial distribution function, bond-length and bond-angle distribution functions. Also geometrical structures after simulations are displayed in figures.

Keywords: Carbon, Nanotube, $O(N)$, Parallel, Tight-Binding, Molecular-Dynamics Simulation, Verlet Algorithm, Maxwell Velocity Distribution.

ÖZ

N-MERTEBELİ PARALEL SIKI-BAĞ MOLEKÜLER-DİNAMİK
BİLGİSAYAR SİMÜLASYONU:
KARBON NANOTÜB ÇALIŞMASI

Özdoğan, Cem

Doktora, Fizik Bölümü

Tez Yöneticisi: Assoc. Prof. Dr. Gülay Dereli

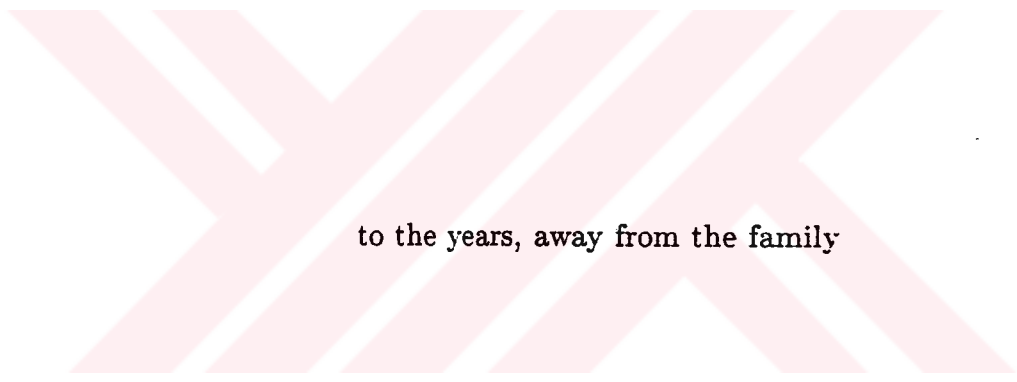
Haziran 2002, 119 sayfa

Karbon nanotüblerin simülasyonlarında kullanılmak üzere N-mertebeli paralel sıkı-bağ moleküler-dinamik bilgisayar simülasyonu yöntemi geliştirilmesi hedeflenmiştir. Geleneksel SB Schrödinger denklemini Hamilton matrisinin köşegenleştirilmesi ile çözer. Bu da atom sayısı ile kübik orantılı olarak bir çözüm zamanıdır, $O(N^3)$ SBMD. $O(N^3)$ SBMD yönteminin Karbon nanotüplerine uygulanmasıyla, bu yöntemin temel sınırlamasının çalışılan sistemin boyutu ile artan simülasyon zamanı olduğu görülmüştür. Bu da simülasyonları hızlandırmak için çeşitli yöntemler uygulanması gerektiğini gösterir. Hesap zamanını azaltmak için kullanılan bu tekniklerden birisi atom sayısı ile doğru

orantılı bir çözüm zamanıdır, $O(N)$ SBMD. Bir diğer yöntem ise paralel hesap yöntemidir. $O(N)$ SBMD (Böl ve Kullan (Divide and Conquer) yaklaşımı ile) yöntemi Karbon nanotüb simülasyonu programımıza uygulanmış ve daha sonra $O(N)$ SBMD programımızda paralelleştirilmiştir. Sonuçlar paralel hesap tekniğinin uygulanmasının gerekli olduğunu göstermiştir. Hız testleri 8 bilgisayar ve PVM kütüphanesi içeren dağıtık bir sistemde yapılmıştır.

Geliştirdiğimiz $O(N)$ Paralel SBMD programını 10×10 ve 17×0 yapısındaki Karbon nanotüplerinin çalışılmasında kullandık. Bu tüb yapılarının seçilmesindeki neden farklı 'chirality'e sahip olmalarına rağmen çap büyüklüklerinin benzer olmasıdır. Fermi enerji seviyesi değeri ($\approx 3.7 \text{ eV}$) her iki tüb yapısının değişik 'chirality'i fakat aynı yarıçap değerine sahip olmalarından dolayı çok yakın bulunmuştur. Öte yandan durum yoğunlukları sonuçları beklenildiği gibi 10×10 tüb için iletken 17×0 tüb için de yarıiletken yapı göstermiştir. Daha sonra 10×10 ve 17×0 tüplerinin yapısal dengeleri ve enerjileri incelendi. Elastik özelliklerinin eksen boyunca yapılan baskı ile değişmesi oda sıcaklığında çalışılmıştır. Young modülüsü, germe şiddeti, Poisson oranı ve salınım frekansı değerleri hesaplanmıştır. Yüksek baskı oranlarında kopmalar gözlemlendi. Bütün bu sonuçlar toplam enerji, radyal dağılım fonksiyonu, bağ-açısı ve bağ-uzunluğu fonksiyonu grafiklerinde görülmektedir. Ayrıca simülasyonlar sonunda elde edilen geometrik yapılar da resimlendirilmiştir.

Anahtar Kelimeler: Karbon, Nanotüp, N-Mertebe, Sıkı-Bağ, Moleküler-Dinamik Simülasyonu, Verlet Yöntemi, Maxwell Hız Dağılımı.



to the years, away from the family

ACKNOWLEDGMENTS

I am thankful to Assoc. Prof. Dr. Gülay Dereli as a supervisor for her guidance and her continued encouragement throughout the stages of my Ph.D. study. I am also grateful to Prof. Dr. Tekin Dereli for companions, suggestions, worthy supports and encouragements during these stages.

The research reported here is supported by TÜBİTAK through the project TBAG-1877 and by METU through the project AFP-2000-07-02-11. Tahir Çağın's visit to METU was made possible by a grant within the TOKTEN/Unistar program.

TABLE OF CONTENTS

ABSTRACT	ii
ÖZ	v
DEDICATION	vii
ACKNOWLEDGMENTS	viii
TABLE OF CONTENTS	ix
LIST OF TABLES	xi
LIST OF FIGURES	xii
CHAPTER	
I INTRODUCTION	1
II STRUCTURE OF SINGLE-WALL CARBON NANOTUBES	7
II.1 Classification of Carbon Nanotubes	8
II.2 Chiral Vector: \vec{C}_h	9
II.3 Translational Vector: \vec{T}	11
II.4 Unit Cells and Brillouin Zones	14
II.5 Electronic structure of nanotubes	15
III METHOD	19
III.1 Tight-Binding Formalism	19
III.2 Tight-Binding Molecular Dynamics	21
III.3 Hamiltonian Matrix	22
III.4 Hellmann–Feynman forces	25
III.5 Repulsive Pair Potential	26
III.6 Molecular–Dynamics Scheme	28
III.7 MD Time Step	29

III.8	Parallelization	33
III.9	Example about PVM	35
IV	RESULTS	36
IV.1	O(N) Tight Binding MD Simulations	36
IV.1.1	The Periodic Boundary Condition (PBC) and the Effect of the Buffer Size on O(N) TBMD, Carbon Nanotube Simulation	40
IV.1.2	The Effect of the Electronic Temperature ($k_B T$) on O(N) TBMD	43
IV.1.3	The Effect of the Electronic Temperature ($k_B T$) on Fermi–Dirac Distribution and on Local Den- sity of States	47
IV.1.4	Discussion	55
IV.2	Parallel O(N) TBMD	58
IV.2.1	Algorithm	59
IV.2.2	Discussion	60
IV.3	Structural Stability and Energetics Under Uniaxial Strain	74
IV.3.1	Method	74
IV.3.2	Results	76
IV.3.3	Discussion	79
V	CONCLUSION	95
	REFERENCES	100
	APPENDICES	105
A	ACRONYMS	105
B	MAXWELL–BOLTZMANN VELOCITY DISTRIBUTION . . .	107
B.1	The Distribution of Molecular Velocities	107
B.2	Algorithm for Maxwell Velocity Distribution	111
C	DETERMINATION OF ΔT	114
D	FLOWCHARTS OF THE PROGRAM	115
D.1	Sequential O(N) TBMD	115
D.2	Parallel O(N) TBMD	117
VITA	118

LIST OF TABLES

TABLE

II.1	Values for the characterization parameters for carbon nanotubes labeled by the chiral vector $\vec{C}_h = (n, n)$ and $\vec{C}_h = (n, 0)$	12
II.2	Parameters for Carbon Nanotubes; symbols are namely; a : length of unit vector, \vec{a}_1, \vec{a}_2 : unit vectors, \vec{b}_1, \vec{b}_2 : reciprocal lattice vectors, \vec{C}_h : chiral vector, L : length of \vec{C}_h , d_t : diameter, θ : chiral angle, d : $\gcd(n, m)$, d_R : $\gcd(2n+m, 2m+n)$, \vec{T} : translational vector, T : length of \vec{T} , N : Number of hexagons in the nanotube unit cell	13
IV.1	Speed Up values are listed for varying system size and processor number (np) for (10x10) CNT structure.	64
IV.2	Efficiency with respect to for varying system size and processor number (np)	65
IV.3	Comparison of Dsyevd and Dsyev Lapack routines on the cases; total run time for $O(N^3)$ TBMD and diagonalization time $O(N)$ TBMD per MD Step (in sec).	65

LIST OF FIGURES

FIGURES

II.1	The unrolled honeycomb lattice of a nanotube. The figure corresponds to $\vec{C}_h = (4, 2)$, $d = d_R = 2$, $\vec{T} = (4, -5)$, $N = 28$	9
II.2	The Brillouin zone of a carbon nanotube is represented by the line segment WW' which is parallel to \vec{K}_2 . The vectors \vec{K}_1 and \vec{K}_2 are reciprocal lattice vectors corresponding to \vec{C}_h and \vec{T} , respectively. The figure corresponds to $\vec{C}_h = (4, 2)$, $\vec{T} = (4, -5)$, $N = 28$, $\vec{K}_1 = \frac{(5\vec{b}_1 + 4\vec{b}_2)}{28}$, $\vec{K}_2 = \frac{(4\vec{b}_1 - 2\vec{b}_2)}{28}$	14
II.3	The condition for metallic energy bands: if the ratio of the length of the vector $Y\vec{K}$ to that of \vec{K}_1 is an integer, metallic energy bands are obtained.	17
III.1	The Total Energy versus MD Steps for the tube 10x10 (20 layers, T=300 K, electronic temperature is 0.005 eV) for the Δt values of 0.02 and 0.06 fs, respectively.	30
III.2	The Total Energy versus MD Steps for the tube 10x10 (20 layers, T=300 K, electronic temperature is 0.005 eV) for the Δt values of 0.5 and 1 fs, respectively.	31
III.3	The Total Energy versus MD Steps for the tube 10x10 (20 layers, T=300 K, electronic temperature is 0.005 eV) for the Δt values of 2 and 3 fs, respectively.	32
IV.1	The difference of $O(N^3)$ total energy result (-8.350497775) with $O(N)$ total energy result for the variation of $O(N)$ parameter (Buffer Size) for the 24 Layers and 18 Layers 10x10 Tube with box size is equal to 1.229 Å , the electronic temperature is $k_B T = 0.005 eV$	42
IV.2	The effect of electronic temperature on the total energy (Tube 10x10 no strain T= 300 K) for the values $k_B T = 0.025 eV$ and $k_B T = 0.05 eV$, respectively.	44
IV.3	The effect of Buffer Size for the Total Energy value for the tube structure 10x10, with different electronic temperature values, respectively.	45
IV.4	The effect of Buffer Size for the Total Energy value for the tube structure 17x0, with different electronic temperature values, respectively.	46
IV.5	Fermi-Dirac Distribution Function vs Energy for various electronic temperatures for the Tube Structure 10x10.	49

IV.6	Fermi-Dirac Distribution Function vs Energy for various electronic temperatures for the Tube Structure 17x0.	50
IV.7	Local DOS vs Energy for different electronic temperatures for the Tube Structure 10x10..	51
IV.8	Local DOS vs Energy for different electronic temperatures for the Tube Structure 10x10	52
IV.9	Local DOS vs Energy for different electronic temperatures for the Tube Structure 17x0.	53
IV.10	Local DOS vs Energy for different electronic temperatures for the Tube Structure 17x0.	54
IV.11	Physical Properties; Radial Distribution Function, Pair Correlation Function, Bond-Angle Distribution Function, Bond-Length Distribution Function for the Tube Structure 10x10 and T= 300 K with the electronic temperature 0.005 eV (MD Time Step \equiv 1 fs); respectively.	66
IV.12	Physical Properties; Atomic Coordination Number, Repulsive Energy, Band Structure Energy, and Total Energy for the Tube Structure 10x10 and T=300 K with the electronic temperature 0.005 eV (MD Time Step \equiv 1 fs); respectively.	67
IV.13	Run Time per MD Step (sec) vs Number of Atoms for $O(N^3)$ TBMD and $O(N)$ TBMD	68
IV.14	Run Time per MD Step (sec) vs Number of Atoms for different number of processors (np)	69
IV.15	Run Time per MD Step (sec) vs Number of Processors for varying size of atoms (N)	70
IV.16	Communication Time per MD Step (sec) vs Number of Atoms for different number of processors (np)	71
IV.17	Communication Time per MD Step (sec) vs Number of Processors for different number of atoms (N)	72
IV.18	Contribution of Communication Time to Run Time (%) per MD Step vs Number of Atoms for different number of processors	73
IV.19	The geometrical structure of 10x10 pristine Carbon nanotube after simulation.	82
IV.20	Total energy curve as a function of strain ϵ	83
IV.21	The variation of total energy of deformed 10x10 Carbon nanotube during MD simulation for the strains 0.22 and -0.07 (negative sign corresponds for the compression), respectively.	84
IV.22	The geometrical structure of 10x10 Carbon Nanotube with 0.22 strain (elongation)after simulation.	85
IV.23	The geometrical structure of 10x10 Carbon Nanotube with 0.07 strain (contraction)after simulation.	86
IV.24	Radial Distribution Functions for the Tube Structure 10x10 under strains 0.22 and -0.07, respectively.	87
IV.25	Bond-length Distribution Functions for the Tube Structure 10x10 under strains 0.22 and -0.07, respectively.	88

IV.26	Bond-angle Distribution Functions for the Tube Structure 10x10 under strains 0.22 and -0.07, respectively.	89
IV.27	The geometrical structure of 10x10 Carbon Nanotube with 0.23 strain (elongation)after simulation.	90
IV.28	The geometrical structure of 10x10 Carbon Nanotube with 0.08 strain (contraction)after simulation.	91
IV.29	The variation of total energy of deformed 10x10 Carbon nanotube during MD simulation for the strains 0.23 and -0.08, respectively.	92
IV.30	The uniaxial stress applied to the tube versus the strain ϵ (elongation) and the variation of radius of pristine (10x10) Carbon nanotube as a function of MD steps; respectively. . .	93
IV.31	The variation of radius of (10x10) Carbon nanotube as a function of MD steps with strain rates 22% and -7%; respectively.	94
B.1	Diagram of velocity space.	109
B.2	Graph of Maxwell-Boltzmann speed distribution function. . .	110
B.3	Most probable (v_m), arithmetic mean (\bar{v}), and the root-mean-square (v_{rms}) speeds.	111

CHAPTER I

INTRODUCTION

Nanotechnology is predicted to spark a series of industrial revolutions in the next two decades that will transform our lives to a far greater extent than silicon microelectronics did in the 20th century. Carbon nanotubes could play a pivotal role in this upcoming revolution if their remarkable electrical and mechanical properties can be exploited. Nanotubes have an impressive list of attributes. They can behave like metals or semiconductors, can conduct electricity better than copper, can transmit heat better than diamond, and they rank among the strongest materials known – not bad for structures that are just a few nanometers across. Several decades from now we may see integrated circuits with components and wires made from nanotubes, and may be even buildings that can snap back into shape after earthquake [1].

Carbon nanotubes were first observed in 1991 by Sumio Iijima at NEC in Japan. These so-called multiwall nanotubes consisted of several concentric tubes of carbon nested inside each other. Two years later Iijima, Donald Bethune at IBM in the US and others observed single-wall nanotubes just 1–2 nm in diameter. But the field really took off a few years later when various

groups found ways to mass-produce high-quality nanotubes. A nanotube can be either a metal or a semiconductor depending on the way the graphite sheet is rolled up. Metallic nanotubes are also ideal systems in which to explore electron transport in one dimension thanks to their near-perfect structures. Researchers expect to find more complex behavior for multiwall nanotubes due to their interactions between adjacent layers.

Industry has begun to notice the unique properties of carbon nanotubes. The first commercial device that uses multiwall nanotubes may be a lamp that operates on the field-emission principle. Moreover, the field-emitting characteristics of carbon-nanotube films have attracted serious interest from the giants of the display industry. Samsung, for example, plans to market a flat-panel color display made from multiwall nanotubes within two years. Meanwhile, research at IBM indicates that nanotube transistors should be competitive with state-of-the-art silicon devices. Nanotubes could also be used to store hydrogen to power electric vehicles.

However, many technological hurdles need to be overcome before large-scale applications reach the marketplace. For example, the techniques that are used to build electronic components from nanotubes are painstaking and utterly inappropriate for mass production. But perhaps the most severe limitation is that high-quality nanotubes can only be produced in very limited quantities—commercial nanotube soot costs 10 times as much as gold. Although there are many challenges ahead, nanotubes appear destined to open up a host of new practical applications and improve our understanding of basic

physics at the nanometer scale.

Carbon nanotubes were discovered in 1991 by Iijima of NEC Corporation [2]. Since then, efforts in synthesis, characterization and theoretical investigation on nanotubes has grown exponentially. This is mostly due to their perceived novel mechanical and electronic properties and their tremendous potential for future technological applications. In 1993, the simplest kind of carbon nanotubes, single walled carbon nanotubes, were discovered independently by Iijima group [3] and an IBM team headed by Bethune [4]. These SWNTs can be regarded as a rolled-up graphite sheet in the cylindrical form. Some specific defect-free forms of these SWNT show remarkable mechanical properties and metallic behavior [48]. These materials present tremendous potential as components for use in nano-electronic and nano-mechanical device applications or as structural elements in various devices . Various properties and applications of nanotubes can be found in literature [5, 69].

Using classical molecular dynamics techniques with well parameterized empirical potentials to study the structural, thermal and mechanical properties of these novel materials is possible. Various researchers have performed such studies [6]–[11]. However, understanding the electronic properties of these systems require the use of quantum mechanical description of the system. There are two possible levels of theory could be used, density functional theory and tight binding theory.

Starting with the work of Slater and Koster [12], the tight-binding theory of electronic structure has played an increasingly important role in computational

material science. It has developed as an effective tool for calculations of atomic and electronic structures, total energies, diffusion barriers, and interatomic forces of large condensed-matter and molecular systems. The benefits of TB theory include ease of implementation, low computational workload, robust transferability as well as relatively good reliability. Yet these features are obtained by maintaining the underlying formalism at the level of the simplest quantum-mechanical treatment of condensed-matter systems and within a rather intuitive chemical and physical conceptual framework.

The TB theory has been established as a good compromise between *ab initio* simulations and model-potential ones, bridging the gap between them, either as far as the overall numerical efficiency and as far as accuracy concerned. Although original Slater and Koster scheme was originally addressed to investigate the electronic spectra of crystalline materials only, the TB theory was later generalized to the level of a theoretical scheme for total energy calculations [13, 14]. Finally, the true foundation of TB theory was established in the context of the density-functional theory [15].

Molecular dynamics (MD) [16, 17] is a very powerful technique for the study of materials. This technique can be used to simulate material systems at different conditions of temperature, pressure etc., including materials at extreme thermodynamic conditions. It is also useful technique to analyze complex processes (e.g. kinetic processes) that take place at the atomic scale in the material. Moreover, MD is a convenient tool for determining the ground state (i.e. minimize the total energy with respect to the atomic coordinates)

of a given material. The main problem in the application of this technique to the study of real materials is the determination of the forces, \vec{f}_α , between the atoms forming the system. Once these forces are known, it is straightforward to perform MD simulations of the material of interest.

TBMD [18] is a computational tool designed to run finite-temperature MD simulations within the semi-empirical tight-binding scheme. The electronic structure of the simulated system is calculated by a TB Hamiltonian so that the quantum mechanical many-body nature of interatomic forces is naturally taken into account.

TB theory and TB molecular dynamics (TBMD) can be considered as popular and valuable computational schemes available to material theorists. The applications range from semiconductors to metals and organic systems, from bulk to surfaces and interfaces, from ordered to defected and disordered materials. A wide range of physical properties are currently calculated in this framework, including structural properties, energetics of defects and surface reconstructions, cluster properties, diffusion rates, electronic spectra, light-matter interactions, transport properties of materials and devices, etc.

This thesis is organized as follows; in Chapter II, we have defined the terminology used in expressing the structure of carbon nanotubes. According to this terminology we have classified the CNTs. In Chapter III section 1-7 we have introduced the TB formalism and TBMD technique we have used during our simulations. Along with the parallelization algorithms in section 8 and 9. In Chapter IV in 3 sections we have displayed our results. In section 1 of this

chapter, the effect of the parameters such as buffer size, electronic temperature and Periodic Boundary Condition (PBC) on the accuracy of $O(N)$ TBMD is studied. In section 2 parallelization technique is applied to the developed $O(N)$ TBMD as further improvement in shortening the simulation time. In section 3 of this chapter, structured stability and energetics of CNTs under uniaxial strain are studied. In Chapter V conclusion part of the thesis is given. Appendices contains flowcharts of the programs together with interaction time and Maxwell–Boltzmann velocity distribution.



CHAPTER II

STRUCTURE OF SINGLE-WALL CARBON NANOTUBES

Solid-state devices in which electrons are confined to two dimensional planes have provided some of the most exciting scientific and technological breakthroughs of the last 50 years. From metal-oxide-silicon field effect transistors to high-mobility gallium-arsenide heterostructures, these devices have played a key role in the microelectronics revolution and are critical components in a wide array of products from computers to compact-disc players.

However, 1-D systems are also proving to be very exciting. For many years, studies of quasi 1-D systems, such as conducting polymers, have provided a fascinating insight into the nature of electronic instabilities in one dimension. In addition, 1-D devices such as 'electron waveguides' -in which electrons propagate through a narrow channel of material- have been created. Experiments on these devices have shown, for example, that the conductance of 'ballistic' 1-D systems -in which electrons travel the length of the channel without being scattered- is quantized in units of e^2/h , where e is the charge

on the electron and h is the Planck constant.

These systems, however, have been limited by the fact that they are inherently complex and/or difficult to make. What has been lacking is the perfect model system for exploring one-dimensional transport, a 1-D conductor that is cheap and easy to make, can be individually manipulated and measured, and has little structural disorder. Single-wall carbon nanotubes fit this bill remarkably well. Some nanotubes are semiconductors. They can therefore be used to construct devices that are one-dimensional analogues of metal-oxide-silicon field effect transistors, in which the electrons move along the surface of a thin two-dimensional layers. Other nanotubes, in contrast, are nearly perfect metallic conductors, and are a new 'laboratory' for studying the motion of electrons in one dimension.

II.1 Classification of Carbon Nanotubes

A single-wall nanotube is defined by a cylindrical graphene sheet with a diameter of about 0.7 – 10.0 nm, though most of the observed single-wall nanotubes have diameters < 2 nm. If we neglect the two ends of a carbon nanotube and focus on the large aspect ratio of the cylinder (i.e., length/ diameter which can be as large as $10^4 - 10^5$), these nanotubes can be considered as one-dimensional nanostructures.

The primary symmetry classification of a carbon nanotube is as either being achiral or chiral. An achiral carbon nanotube is defined by a carbon nanotube whose mirror image has an identical structure to the original one.

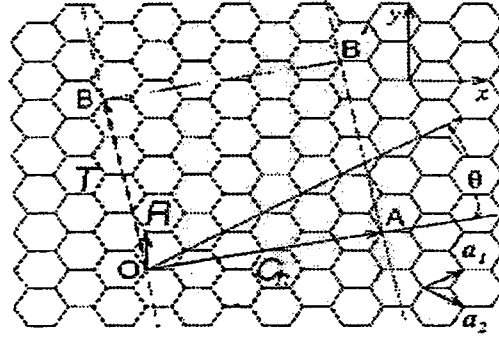


Figure II.1: The unrolled honeycomb lattice of a nanotube. The figure corresponds to $\vec{C}_h = (4, 2)$, $d = d_R = 2$, $\vec{T} = (4, -5)$, $N = 28$

There are only two cases of achiral nanotubes; armchair and zigzag nanotubes.

The names of armchair and zigzag arise from the shape of the cross-sectional ring at the edge of the nanotubes.

II.2 Chiral Vector: \vec{C}_h

The structure of a single-wall carbon nanotube is specified by the vector (\vec{OA} in Fig. II.1) which corresponds to a section of the nanotube perpendicular to the nanotube axis (the equator of the nanotube). In Figure II.1, the unrolled honeycomb lattice of the nanotube is shown, in which \vec{OB} is the direction of the nanotube axis, and the direction of \vec{OA} corresponds to the equator. By considering the crystallographically equivalent sites O, A, B, and B', and by rolling the honeycomb sheet so that point O and A coincide (and points B and B' coincide), a paper model of a carbon nanotube can be constructed. The vectors \vec{OA} and \vec{OB} define the chiral vector \vec{C}_h and the translational vector \vec{T} of a carbon nanotube, respectively, as further explained below. The chiral

vector \vec{C}_h can be expressed by the real space unit vectors a_1 and a_2 (see Figure II.1) of the hexagonal lattice defined in Eqn. II.1:

$$\vec{C}_h = n\vec{a}_1 + m\vec{a}_2 \equiv (n, m) \quad (n, m \text{ are integers, } 0 \leq |m| \leq n) \quad (\text{II.1})$$

An armchair nanotube corresponds to the case of $n = m$, that is $\vec{C}_h = (n, n)$, and a zigzag nanotube corresponds to the case of $m = 0$, or $\vec{C}_h = (n, 0)$. All other (n, m) chiral vector correspond to chiral nanotubes. Because of the hexagonal symmetry of the honeycomb lattice, we need to consider only $0 < |m| < n$ in $\vec{C}_h = (n, m)$ for chiral nanotubes.

The diameter of the carbon nanotube, d_t , is given by L/π , in which L is the circumferential length of the carbon nanotube:

$$d_t = L/\pi, \quad L = |\vec{C}_h| = \sqrt{\vec{C}_h \cdot \vec{C}_h} = a\sqrt{n^2 + m^2 + nm} \quad (\text{II.2})$$

It is noted here that \vec{a}_1 and \vec{a}_2 are not orthogonal to each other and that the inner products between \vec{a}_1 and \vec{a}_2 yield:

$$\vec{a}_1 \cdot \vec{a}_1 = \vec{a}_2 \cdot \vec{a}_2 = a^2, \quad \vec{a}_1 \cdot \vec{a}_2 = \frac{a^2}{2} \quad (\text{II.3})$$

where the lattice constant $a = 1.44\text{\AA} \sqrt{3}$ of the honeycomb lattice.

The chiral angle θ (see Figure II.1) is defined as the angle between the vectors \vec{C}_h and \vec{a}_1 , with values of θ in the range $0 \leq |\theta| \leq 30^\circ$, because of the hexagonal symmetry of the honeycomb lattice. The chiral angle θ denotes the tilt angle of the hexagons with respect to the direction of the nanotube axis, and the angle θ specifies the spiral symmetry. The chiral angle θ yields for an

expression for $\cos\theta$:

$$\cos\theta = \frac{\vec{C}_h \cdot \vec{a}_1}{|\vec{C}_h||\vec{a}_1|} = \frac{2n+m}{2\sqrt{n^2+m^2+nm}} \quad (\text{II.4})$$

thus relating θ to the integers (n,m) defined in Eqn.II.1. In particular, zigzag and armchair nanotubes corresponds to $\theta = 0^\circ$ and $\theta = 30^\circ$, respectively.

II.3 Translational Vector: \vec{T}

The translational vector \vec{T} is defined to be unit vector of a 1D carbon nanotube. The vector \vec{T} is parallel to the nanotube axis and is normal to the chiral vector \vec{C}_h in the unrolled honeycomb lattice in Figure II.1. The lattice vector \vec{T} shown as \vec{OB} in Figure II.1 can be expressed in terms of the basis vectors as:

$$\vec{T} = t_1\vec{a}_1 + t_2\vec{a}_2 \equiv (t_1, t_2) \quad (t_1, t_2 \text{ are integers}) \quad (\text{II.5})$$

The vector \vec{T} corresponds to the first lattice point of the 2D graphene sheet through which the vector \vec{OB} passes. From this fact, it is clear that t_1 and t_2 do not have a common divisor except for unity. Using $\vec{C}_h \cdot \vec{T} = 0$ and Eqns. II.1, II.3, and II.5:

$$t_1 = \frac{2m+n}{d_R}, \quad t_2 = -\frac{2n+m}{d_R} \quad (\text{II.6})$$

where d_R is the greatest common divisor (gcd) of $(2m+n)$ and $(2n+m)$. Also by introducing d as the greatest common divisor of n and m , then d_R can be related to d by,

$$d_R = \begin{cases} d & \text{if } n-m \text{ is not a multiple of } 3d \\ 3d & \text{if } n-m \text{ is a multiple of } 3d. \end{cases} \quad (\text{II.7})$$

The length of the translation vector, T , is given by:

$$T = |\vec{T}| = \sqrt{3}L/d_R \quad (\text{II.8})$$

where the circumferential nanotube length L is given by Eqn. II.2. The length T is greatly reduced when (n,m) have a common divisor or when $(n-m)$ is a multiple of $3d$.

The unit cell of the 1D carbon nanotube is the rectangle $OAB'B$ defined by the vectors \vec{C}_h and \vec{T} , while the vectors \vec{a}_1 and \vec{a}_2 define the area of the unit cell of 2D graphite. When the area of the nanotube unit cell $|\vec{C}_h \times \vec{T}|$ is divided by the area of a hexagon $|\vec{a}_1 \times \vec{a}_2|$, the number of hexagons per unit cell N is obtained as a function of n and m as:

$$N = \frac{|\vec{C}_h \times \vec{T}|}{|\vec{a}_1 \times \vec{a}_2|} = \frac{2(m^2 + n^2 + nm)}{d_R} = \frac{2L^2}{a^2 d_R} \quad (\text{II.9})$$

where L and d_R are given by Eqns. II.2 and II.7, respectively; and each hexagon contains two carbon atoms. Thus there are $2N$ carbon atoms (or $2p_z$ orbitals) in each unit cell of the carbon nanotube.

In Table II.1, it is listed the characteristic parameters of carbon nanotubes specified by (n, n) and $(n, 0)$.

Table II.1: Values for the characterization parameters for carbon nanotubes labeled by the chiral vector $\vec{C}_h = (n, n)$ and $\vec{C}_h = (n, 0)$

\vec{C}_h	d	d_R	d_t (Å)	L/a	\vec{T}	T/a	N
(n,n)	n	$3n$	$\sqrt{3}na/\pi$	$\sqrt{3}n$	$(1,-1)$	1	$2n$
$(n,0)$	n	n	na/π	n	$(1,-2)$	$\sqrt{3}$	$2n$

All parameters defined are summarized in Table II.2. The values of all parameters listed depend on two integers, n , and m , of the chiral vector \vec{C}_h .

Table II.2: Parameters for Carbon Nanotubes; symbols are namely; a : length of unit vector, \vec{a}_1, \vec{a}_2 : unit vectors, \vec{b}_1, \vec{b}_2 : reciprocal lattice vectors, \vec{C}_h : chiral vector, L : length of \vec{C}_h , d_t : diameter, θ : chiral angle, d : $\gcd(n,m)$, d_R : $\gcd(2n+m, 2m+n)$, \vec{T} : translational vector, T : length of \vec{T} , N : Number of hexagons in the nanotube unit cell .

symbol	formula	value
a	$a = \sqrt{3}a_{C-C} = 2.49\text{\AA}$	$a_{C-C} = 1.44\text{\AA}$
\vec{a}_1, \vec{a}_2	$\left(\frac{\sqrt{3}}{2}, \frac{1}{2}\right) a, \left(\frac{\sqrt{3}}{2}, -\frac{1}{2}\right) a$	x,y coordinate
\vec{b}_1, \vec{b}_2	$\left(\frac{1}{\sqrt{3}}, 1\right) \frac{2\pi}{a}, \left(\frac{1}{\sqrt{3}}, -1\right) \frac{2\pi}{a}$	x,y coordinate
\vec{C}_h	$\vec{C}_h = n\vec{a}_1 + m\vec{a}_2 \equiv (n, m)$	$(0 \leq m \leq n)$
L	$L = \vec{C}_h = a\sqrt{n^2 + m^2 + nm}$	
d_t	$d_t = L/\pi m$	
θ	$\sin \theta = \frac{\sqrt{3}m}{2\sqrt{n^2 + m^2 + nm}}$ $\cos \theta = \frac{2n+m}{2\sqrt{n^2 + m^2 + nm}}$	$0 \leq \theta \leq 30^\circ$ $\tan \theta = \frac{\sqrt{3}m}{2n+m}$
d	$\gcd(n,m)$	
d_R	$d_R = \begin{cases} d \\ 3d \end{cases}$	if $n-m$ is not a multiple of $3d$ if $n-m$ is a multiple of $3d$.
\vec{T}	$\vec{T} = t_1\vec{a}_1 + t_2\vec{a}_2 \equiv (t_1, t_2)$ $t_1 = \frac{2m+n}{d_R}, t_2 = -\frac{2n+m}{d_R}$	$\gcd(t_1, t_2) = 1$
T	$T = \vec{T} = \sqrt{3}L/d_R$	
N	$N = \frac{2(m^2 + n^2 + nm)}{d_R}$	

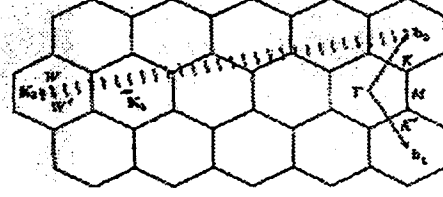


Figure II.2: The Brillouin zone of a carbon nanotube is represented by the line segment WW' which is parallel to \vec{K}_2 . The vectors \vec{K}_1 and \vec{K}_2 are reciprocal lattice vectors corresponding to \vec{C}_h and \vec{T} , respectively. The figure corresponds to $\vec{C}_h = (4, 2)$, $\vec{T} = (4, -5)$, $N = 28$, $\vec{K}_1 = \frac{(5\vec{b}_1 + 4\vec{b}_2)}{28}$, $\vec{K}_2 = \frac{(4\vec{b}_1 - 2\vec{b}_2)}{28}$

II.4 Unit Cells and Brillouin Zones

The unit cell for a carbon nanotube in the real space is given by the rectangle generated by the chiral vector \vec{C}_h and the translational vector \vec{T} , is shown in OAB'B in Figure II.2. Since there are $2N$ carbon atoms in this unit cell, we will have N pairs of bonding π and anti-bonding π^* electronic energy bands.

Expressions for the reciprocal lattice vectors \vec{K}_2 along the nanotube axis and \vec{K}_1 in the circumferential direction (since nanotubes are one-dimensional materials, only \vec{K}_2 is a reciprocal lattice vector. \vec{K}_1 gives discrete k values in the direction of \vec{C}_h .) are obtained from the relation $\vec{R}_i \cdot \vec{K}_j = 2\pi\delta_{ij}$, where \vec{R}_i and \vec{K}_j are, respectively, the lattice vectors in real and reciprocal space. Then using Eqns. II.6, II.9, and the relations,

$$\vec{C}_h \cdot \vec{K}_1 = 2\pi, \quad \vec{T} \cdot \vec{K}_1 = 0, \quad \vec{C}_h \cdot \vec{K}_2 = 0, \quad \vec{T} \cdot \vec{K}_2 = 2\pi, \quad (\text{II.10})$$

we get expressions for \vec{K}_1 and \vec{K}_2 :

$$\vec{K}_1 = \frac{1}{N}(-t_2\vec{b}_1 + t_1\vec{b}_2), \quad \vec{K}_2 = \frac{1}{N}(m\vec{b}_1 - n\vec{b}_2) \quad (\text{II.11})$$

where \vec{b}_1 and \vec{b}_2 are the reciprocal lattice vectors of two-dimensional graphite. In Figure II.2, the first Brillouin zone of this one-dimensional material is the line segment WW' . Since $N\vec{K}_1$ corresponds to a reciprocal lattice vector of 2D graphite, two wave vectors differ by $N\vec{K}_1$ are equivalent. Since t_1 and t_2 do not have a common divisor except for unity, none of the $N - 1$ vectors $\mu\vec{K}_1$ (where $\mu = 1, \dots, N - 1$) are reciprocal lattice vectors of 2D graphite. Thus the N wave vectors $\mu\vec{K}_1$ ($\mu = 0, \dots, N - 1$) give rise to N discrete k vectors, N one-dimensional energy bands will appear. Because of the translational symmetry of \vec{T} , we have continuous wave vectors in the direction of \vec{K}_2 for a carbon nanotube of infinite length. However, for a nanotube of finite length L_t , the spacing between wave vectors is $2\pi/L_t$; this spacing between wave vectors has been observed experimentally [19].

II.5 Electronic structure of nanotubes

The remarkable electrical properties of single-wall carbon nanotubes stem from the unusual electronic structure of 'graphene', the 2D material from which they are made. Graphene is simply a single atomic layer of graphite, the material that makes up pencil lead. Graphene has a two-dimensional honeycomb structure, made up of sp^2 -bonded carbon atoms, see Figure II.1. Its conducting properties are determined by the nature of the electronic states near the Fermi energy, E_F , which is the energy of the highest occupied electronic state at zero temperature. The energy of the electronic states as a function of their wavevector, k , near E_F ; 'band structure', which is determined by the way in

which electrons scatter from the atoms in the crystal lattice, is quite unusual. It is not like that of a metal, which has many states that freely propagate through the crystal at E_F . Nor is the band structure like that of a semiconductor, which has an energy gap with no electronic states near E_F due to the backscattering of electrons from the lattices.

The band structure of graphene is instead somewhere in between these extremes. In most directions, electrons moving at the Fermi energy are backscattered by atoms in the lattice, which gives the material an energy band gap like that of a semiconductor. However, in other directions, the electrons that scatter from different atoms in the lattice interfere destructively, which suppresses the backscattering and leads to metallic behavior. Graphene is therefore called a 'semimetal', since it is metallic in the special directions and semiconducting in the others.

To make a 1D conductor from this 2D world, it is followed the lead of string theorists and curl up one of the extra dimensions to form a tube. The resulting periodic boundary conditions on the wavefunction quantizes k_n , the component of k perpendicular to the axis of the tube: in the simplest case, $k_n = 2\pi n/C$, where C is the circumference of the tube and n is an integer. The component of k along the length of the tube, meanwhile, remains a continuous variable. The bottom line is that a nanotube can be either a metal or a semiconductor, depending on how the tube is rolled up. This remarkable theoretical prediction prediction has been verified using a number of measurement techniques [20].

The electronic structure of a single wall nanotube can be obtained simply

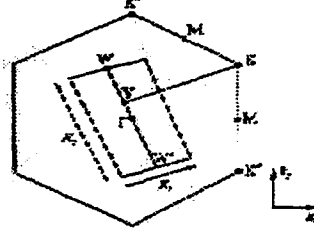


Figure II.3: The condition for metallic energy bands: if the ratio of the length of the vector $Y\vec{K}$ to that of \vec{K}_1 is an integer, metallic energy bands are obtained.

from that of 2D graphite. By using periodic boundary conditions in the circumferential direction denoted by the chiral vector \vec{C}_h , the wave vector associated with the \vec{C}_h direction becomes quantized, while the wave vector associated with the direction of the translational vector \vec{T} (or along the nanotube axis) remains continuous for a nanotube of infinite length (for a real carbon nanotubes, since the length of a nanotube (L_{CN}) is on the order of μm , discrete k vectors ($\Delta k = 2\pi/L_{CN}$) can be expected.) Thus the energy bands consist of a set of 1D energy dispersion relations which are cross sections of those for 2D graphite.

When the energy dispersion relations of 2D graphite, $E_{g2D}(\vec{k})$ at line segments shifted from WW' by $\mu\vec{K}_1$, ($\mu = 0, \dots, N - 1$) are folded so that the wave vectors parallel to \vec{K}_2 coincide with WW' as shown in Figure II.3, N pairs of 1D energy dispersion relations are given by

$$E_{\mu}(k) = E_{g2D} \left(k \frac{\vec{K}_2}{|\vec{K}_2|} + \mu\vec{K}_1 \right), \quad (\mu = 0, \dots, N - 1, \text{ and } -\frac{\pi}{T} < k < \frac{\pi}{T}) \quad (\text{II.12})$$

corresponding to the energy dispersion relations of a single wall carbon nan-

otube. The N pairs of energy dispersion curves given by Eqn. II.12 correspond to the cross sections of the 2D energy dispersion surface for 2D graphite, where cuts are made on the lines $k\vec{K}_2/|\vec{K}_2| + \mu\vec{K}_1$. If for a particular (n,m) nanotube, the cutting line passes through a K point of the 2D Brillouin zone, where the π and π^* energy bands of 2D graphite are degenerate by symmetry, the 1D energy bands have a zero energy gap. Further the density of states at the Fermi level has a finite value for these carbon nanotubes, and they therefore are metallic. If, however, the cutting line does not pass through a K point, the the carbon nanotube is expected to show semiconducting behavior, with a finite energy gap between the valance and the conduction bands.

The condition for obtaining a metallic energy band is that the ratio of the length of the vector $Y\vec{K}$ to that \vec{K}_1 in Figure II.3 is an integer. Since the vector $Y\vec{K}$ is given by

$$Y\vec{K} = \frac{2n+m}{3}\vec{K}_1 \quad (\text{II.13})$$

the condition for metallic nanotubes is that $(2n+m)$ or equivalently $(n-m)$ is a multiple of 3. Particularly, armchair nanotubes denoted by (n, n) are always metallic, the zigzag nanotubes $(n, 0)$ are only metallic when n is a multiple of 3.

CHAPTER III

METHOD

III.1 Tight-Binding Formalism

$$H_{tot} = T_i + T_e + U_{ee} + U_{ei} + U_{ii} \quad (\text{III.1})$$

where;

T_i : Kinetic energy of ions,

T_e : Kinetic energy of electrons,

U_{ee} : Electron–electron interaction energy,

U_{ei} : Electron–ion interaction energy,

U_{ii} : Ion–ion interaction energy.

The many–body Hamiltonian is reduced to the problem of one electron moving in average field due to the other electrons and to the ions.

$$H|\psi_n\rangle = \mathcal{E}_n|\psi_n\rangle \quad (\text{III.2})$$

where,

H :reduced one electron Hamiltonian

$|\psi_n\rangle$:its n^{th} eigenfunction

\mathcal{E}_n : the energy of the n^{th} single–particle state

In TB formulation, $|\psi_n\rangle$ are in the form LCAO (linear combination of atomic orbitals) $|\phi_{l\alpha}\rangle$, where l : quantum number index, α : labels the ions.

$|\phi_{l\alpha}\rangle$:basis set not orthogonal, use of non-orthogonal basis set is not numerically convenient in most cases. The evaluation of overlap integrals $\int \phi_{l'\beta}^* \phi_{l\alpha} d\vec{r}$ causes high workload.

It is possible to orthogonalize the atomic orbitals $|\phi_{l\alpha}\rangle$ in such a way that the new basis set functions still maintain their symmetry properties. New orthogonal basis $\{\varphi_{l\alpha}\}$: Löwdin orbitals [13, 21].

The Schrödinger equation for the single particle states is finally reduced to

$$\sum_{l'\beta} (\langle \varphi_{l'\beta} | H | \varphi_{l\alpha} \rangle - \varepsilon_n \delta_{l'l} \delta_{\alpha\beta}) C_{l'\beta}^n = 0 \quad (\text{III.3})$$

The matrix elements of the Hamiltonian are evaluated by fitting a suitable database obtained either from experiments or by first principle calculations. Typically, the fitting is operated onto the electronic energy bands.

TB parameters as low as possible, number of approximation

- a minimal basis set is selected (i.e. just sp^3 basis set is used for silicon and carbon)
- only two-center integrals are taken into account
- short-range interactions are assumed

Once the single-particle energies are known by solving the secular (III.3), the total energy E_{tot} of a system of ion cores and valance electrons can be

written as:

$$E_{tot} = \sum_n \mathcal{E}_n f(\mathcal{E}_n, T) + U_{ii} - U_{ee} \quad (\text{III.4})$$

where,

$f(\mathcal{E}_n, T)$: Fermi–Dirac Distribution Function

U_{ee} : corrects the double counting of ee interaction in the first term

The sum of over all the single–particle energies is commonly named band structure energy E_{bs} .

Effective repulsive potential; $U_{rep} = U_{ii} - U_{ee} = \sum_{\alpha, \beta > \alpha} \Phi(r_{\alpha\beta})$ can be expressed as a sum of suitable two–body potentials which contains the effects of both the overlap interaction originated by the non–orthogonality of the basis orbitals and the possible charge transfer effects.

III.2 Tight-Binding Molecular Dynamics

During an MD run we must calculate TB matrix elements $\langle \varphi_{l\beta} | H | \varphi_{l\alpha} \rangle$ between atoms which are not at their equilibrium positions. Consistently we need a scaling law $h(r_{\alpha\beta})$ for the variation of fitted $\langle \varphi_{l\beta} | H | \varphi_{l\alpha} \rangle$ against $r_{\alpha\beta}$ (Transferable TB). It is usually determined, along with $\Phi(r_{\alpha\beta})$, by fitting the zero temperature cohesive–energy curves of the system of interest, calculated from first principle for different phases.

The forces $\vec{f}_\alpha (\alpha = 1, \dots, N)$ needed to move atoms can now be straightforwardly evaluated from the TBMD Hamiltonian.

$$\mathcal{H}_{TBMD} = \sum_\alpha \frac{p_\alpha^2}{2m_\alpha} + \sum_n \mathcal{E}_n f(\mathcal{E}_n, T) + U_{rep} \quad (\text{III.5})$$

and are given by

$$\vec{f}_\alpha = - \sum_n \langle \psi_n | \frac{\partial H}{\partial \vec{r}_\alpha} | \psi_n \rangle f(\mathcal{E}_n, T) - \frac{\partial U_{rep}}{\partial \vec{r}_\alpha} \quad (\text{III.6})$$

Hellmann–Feynman contribution to the total force can be calculated as,

$$\sum_n \langle \psi_n | \frac{\partial H}{\partial \vec{r}_\alpha} | \psi_n \rangle f(\mathcal{E}_n, T) = -2 \sum_n f(\mathcal{E}_n, T) \sum_{l\gamma} \sum_{l'\beta} C_{l'\beta}^n \frac{\partial H_{l'\beta, l\gamma}(r_{\beta\gamma})}{\partial \vec{r}_\alpha} C_{l\gamma}^m \quad (\text{III.7})$$

where,

$$H_{l'\beta, l\gamma} = h(r_{\beta\gamma}) \langle \varphi_{l'\beta} | H | \varphi_{l\gamma} \rangle |_{r_{\beta\gamma}=r_0} \quad (\text{III.8})$$

we need the full spectrum of eigenvalues $\{\mathcal{E}_n\}$ and eigenvectors $\{C_{l\alpha}^n\}$ in order to calculate E_b , and Hellmann-Feynman forces.

The zero-temperature Fermi-Dirac distribution function is assumed everywhere.

III.3 Hamiltonian Matrix

Scaling functions for hopping integrals [22].

$$\begin{aligned} scale_{1,2,3,4} = h_\alpha(r) &= h_{\alpha_{1,2,3,4}}(r_0) \left(\frac{r_0}{r}\right)^n * \\ &exp \left\{ n \left[- \left(\frac{r}{r_{c_{1,2,3,4}}}\right)^{n_{c_{1,2,3,4}}} + \left(\frac{r_0}{d_{c_{1,2,3,4}}}\right)^{n_{c_{1,2,3,4}}}\right] \right\} \end{aligned} \quad (\text{III.9})$$

Four two-center integrals; $ss\sigma, sp\sigma, pp\sigma, pp\pi$ interactions, four scaling functions

with;

$$r_0 = 1.536329 \text{ \AA}$$

$n=2$

α	ss σ	sp σ	pp σ	pp π
$h_{\alpha}(r_0)$ eV	-5.0	4.7	5.5	-1.55
$n_{c,\alpha}$	6.5	6.5	6.5	6.5
$r_{c,\alpha}$ (Å)	2.18	2.18	2.18	2.18

There are four valance electrons in outermost shell in carbon, each electron is subject to four interactions with neighbor atom. There are n atoms in the interaction range for each atom. So, totally, n interactions for one electron and $4 * n$ interactions for one atom. Hamiltonian matrix is constructed in such a way; having dimension $h(4*N+1,4*N+1)$, first four rows correspond to interactions of the four electrons of 1st atom. There are N atoms in simulation box, so $4 * N$ rows in matrix. Columns represent the all neighbor atom interactions. There are n nonzero elements in each row. So first four rows contain $4 * n$ interactions ($4 * n$ nonzero term) for first atom.

$$H = \begin{bmatrix} \text{interactions of 1}^{st} \text{ electron of 1}^{st} \text{ atom with all neighbors} \\ \text{interactions of 2}^{nd} \text{ electron of 1}^{st} \text{ atom with all neighbors} \\ \vdots \\ \vdots \\ \vdots \\ \text{interactions of } 4 * N^{th} \text{ electron of } 4 * n^{th} \text{ atom with all neighbors} \end{bmatrix} \quad (\text{III.10})$$

This matrix is a upper triangle matrix, having nonzero terms only in upper triangle. This is necessary for diagonalization procedure. After diagonalization, band structure energy is computed.

For first atom (first four rows in matrix), interactions with one neighbor atom, first subscript gives the electron in atom, second subscript gives the electron in neighbor atom.

four elements in first row;

$$\begin{bmatrix} H_{1,1} = V_{ss\sigma} * scale1 \\ H_{1,2} = V_{sp\sigma} * xx * scale2 \\ H_{1,3} = V_{sp\sigma} * yy * scale2 \\ H_{1,4} = V_{sp\sigma} * zz * scale2 \end{bmatrix}$$

four elements in second row;

$$\begin{bmatrix} H_{2,1} = -V_{sp\sigma} * xx * scale2 \\ H_{2,2} = (V_{pp\sigma} * xx^2 * scale3 + V_{pp\pi} * (1 - xx^2) * scale4 \\ H_{2,3} = (V_{pp\sigma} * scale3 - V_{pp\pi} * scale4) * xx * yy \\ H_{2,4} = (V_{pp\sigma} * scale3 - V_{pp\pi} * scale4) * xx * zz \end{bmatrix}$$

four elements in third row;

$$\begin{bmatrix} H_{3,1} = -V_{sp\sigma} * yy * scale2 \\ H_{3,2} = (V_{pp\sigma} * scale3 - V_{pp\pi} * scale4) * xx * yy \\ H_{3,3} = (V_{pp\sigma} * scale3 * yy^2 + V_{pp\pi} * scale4 * (1 - yy^2)) \\ H_{3,4} = (V_{pp\sigma} * scale3 - V_{pp\pi} * scale4) * yy * zz \end{bmatrix}$$

four elements in fourth row;

$$\begin{bmatrix} H_{4,1} = -V_{sp\sigma} * zz * scale2 \\ H_{4,2} = (V_{pp\sigma} * scale3 - V_{pp\pi} * scale4) * xx * zz \\ H_{4,3} = (V_{pp\sigma} * scale3 - V_{pp\pi} * scale4) * yy * zz \\ H_{4,4} = (V_{pp\sigma} * scale3 * zz^2 + V_{pp\pi} * scale4 * (1 - zz^2)) \end{bmatrix}$$

where xx,yy,zz are $\frac{x_{ij}}{r_{ij}}, \frac{y_{ij}}{r_{ij}}, \frac{z_{ij}}{r_{ij}}$, respectively.

After diagonalization by using LAPACK (Linear Algebra PACKage [23], means that \mathcal{E}_n 's are found), \mathcal{H}_{TBMD} is found by Eq. III.5. Next step is to find forces arising from electronic interactions, namely Hellmann–Feynman forces.

III.4 Hellmann–Feynman forces

Hellmann–Feynman contribution to the total force can be calculated by taking derivatives of Hamiltonian matrix elements, see Eq. III.7.

For example, taking the derivative of $H_{1,2}$ with respect to x means the force between the 1st electron of atom with the 2nd electron of its neighbor in the x -direction. I will give only open form of $F_{1,2}^x$, since the other force elements can be calculated by the same way.

$$H_{1,2} = V_{sp\sigma} * xx * scale2$$

$$F_{1,2}^x = \frac{\partial H_{1,2}}{\partial x_{12}} \quad (III.11)$$

$$xx = \frac{x_{12}}{r_{12}}$$

$$x_{12} = x1 - x2$$

$$r_{12} = \sqrt{(x1 - x2)^2 + (y1 - y2)^2 + (z1 - z2)^2}$$

$$\frac{\partial r_{12}}{\partial x_{12}} = xx$$

$$F_{1,2}^x = V_{sp\sigma} * \left[\frac{\partial}{\partial x} \frac{x}{\sqrt{x^2 + y^2 + z^2}} * scale2 + xx * \frac{\partial scale2}{\partial r} \frac{\partial r}{\partial x} \right] \quad (III.12)$$

$$F_{1,2}^x = V_{sp\sigma} * \left[(1 - xx^2) * \frac{scale2}{r} + xx * xx * \frac{\partial scale2}{\partial r} \right]$$

$$\begin{aligned}
scale2 &= h_{\alpha}(r) = \left(\frac{r_0}{r^2}\right) \exp \left\{ 2 \left[-\left(\frac{r}{r_{c2}}\right)^{n_{c2}} + \left(\frac{r_0}{d_{c2}}\right)^{n_{c2}} \right] \right\} \\
\frac{\partial scale2}{\partial r} &= \frac{scale2}{r} * (-2) * \left[1 + n_{c2} * \left(\frac{r}{r_{c2}}\right)^{n_{c2}} \right] \\
dscalx2 &= xx * \frac{\partial scale2}{\partial r} \\
scale2' &= \frac{scale2}{r}
\end{aligned}$$

so, the final form is;

$$F_{1,2}^x = V_{sp\sigma} * [scale2' * (1 - xx^2) + xx * dscalx2] \quad (III.13)$$

III.5 Repulsive Pair Potential

The form of the repulsive potential is as follows [22]:

$$E_{rep} = \sum_i f \left(\sum_j \phi(r_{ij}) \right) ; f(x) = C_0 + C_1x + C_2x^2 + C_3x^3 + C_4x^4 \quad (III.14)$$

$$x \equiv \phi(r) = \left(\frac{r_0}{r}\right)^m \exp \left\{ m \left[-\left(\frac{r}{d_c}\right)^{m_c} + \left(\frac{r_0}{d_c}\right)^{m_c} \right] \right\} \quad (III.15)$$

where the parameters have the values;

$$m = 3.30304 ,$$

$$m_c = 8.6655 ,$$

$$d_c = 2.1052 \text{ \AA} ,$$

$$C_0 = -2.5909765118191 \text{ eV} ,$$

$$C_1 = 0.5721151498619 \text{ eV} ,$$

$$C_2 = -1.7896349903996E - 3 \text{ eV}$$

$$C_3 = 2.3539221516757E - 5 \text{ eV} ,$$

$$C_4 = -1.24251169551587E - 7 \text{ eV} ,$$

$$r_0 = 1.536329 \text{ \AA}$$

and derivative of the energy expression gives us the force expression

$$\begin{aligned} F_x^i &= -\frac{\partial}{\partial x} E_{rep} = -\frac{\partial}{\partial x} \sum_i f \left(\sum_j \phi(r_{ij}) \right) = \sum_i F_x^i = \sum_i -\frac{\partial}{\partial x} f \left(\sum_j \phi(r_{ij}) \right) \\ &= \sum_i -\frac{\partial}{\partial x} f \left(\sum_j \phi(r(x_{ij})) \right) \end{aligned} \quad (\text{III.16})$$

$$F_x^i = -\frac{\partial}{\partial x} [C_1 A + C_2 A^2 + C_3 A^3 + C_4 A^4]$$

with $A = \sum_j \phi(r_{ij})$;

$$= -\frac{\partial}{\partial \phi} \left[\frac{\partial \phi}{\partial r} \frac{\partial r}{\partial x} \right] \quad (\text{III.17})$$

$$\begin{aligned} F_x^i &= \frac{\partial}{\partial \phi} f \left(\sum_j \phi(r_{ij}) \right) \stackrel{\#ofneigh.}{\sum_{j=1}} \left(\frac{\partial \phi}{\partial r} \bigg|_{r=r_{ij}} \left(\frac{\partial r}{\partial x} \bigg|_{r=r_{ij}, x=x_{ij}} \right) + \right. \\ &\quad \left. \stackrel{\#ofneigh.}{\sum_{j=1}} \frac{\partial}{\partial \phi} f \left(\sum_k \phi(r_{jk}) \right) \left(\frac{\partial \phi}{\partial r} \bigg|_{r=r_{ij}} \left(\frac{\partial r}{\partial x} \bigg|_{r=r_{ij}, x=x_{ij}} \right) \right) \end{aligned} \quad (\text{III.18})$$

$$F_x^i = [C_1 + 2C_2 A + 3C_3 A^2 + 4C_4 A^3] \stackrel{\#ofneigh.}{\sum_{j=1}} \left\{ [B][D] \left[\frac{x_{ij}}{r_{ij}} \right] \right\} +$$

$$\stackrel{\#ofneigh.}{\sum_{j=1}} \left\{ [C_1 + 2C_2 E + 3C_3 E^2 + 4C_4 E^3] [B][D] \left[\frac{x_{ij}}{r_{ij}} \right] \right\} \quad (\text{III.19})$$

with;

$$A = \left(\sum_{j=1}^{\#ofneigh.} \phi(r_{ij}) \right),$$

$$B = \left(\frac{r_0}{r_{ij}} \right)^m \exp \left\{ m \left[-\left(\frac{r_{ij}}{d_c} \right)^{m_c} + \left(\frac{r_0}{d_c} \right)^{m_c} \right] \right\},$$

$$D = \left(1 + m_c \left(\frac{r_{ij}}{d_c} \right)^{m_c} \right) \frac{r_{ij}}{d_c},$$

$$\text{and } E = \left(\sum_{k=1}^{\#ofneigh.} \phi(r_{jk}) \right).$$

III.6 Molecular–Dynamics Scheme

Given the molecular positions, velocities, and other dynamic information at time t , we attempt to obtain the positions, velocities etc. at a later time $t + \delta t$.

If the classical trajectory is continuous, then estimate of the positions, velocities etc. at time $t + \delta t$ may be obtained by Taylor expansion about time t :

$$\vec{r}(t + \delta t) = \vec{r}(t) + \delta t \vec{v}(t) + \frac{1}{2} \delta t^2 \vec{a}(t) + \frac{1}{6} \delta t^3 \vec{b}(t) - \dots \quad (\text{III.20})$$

$$\vec{v}(t + \delta t) = \vec{v}(t) + \delta t \vec{a}(t) + \frac{1}{2} \delta t^2 \vec{b}(t) + \dots \quad (\text{III.21})$$

$$\vec{a}(t + \delta t) = \vec{a}(t) + \delta t \vec{b}(t) + \dots \quad (\text{III.22})$$

$$\vec{b}(t + \delta t) = \vec{b}(t) + \dots \quad (\text{III.23})$$

Velocity–Verlet algorithm takes the form;

$$\vec{r}(t + \delta t) = \vec{r}(t) + \delta t \vec{v}(t) + \frac{1}{2} \delta t^2 \vec{a}(t) \quad (\text{III.24})$$

$$\vec{v}(t + \delta t) = \vec{v}(t) + \frac{1}{2} \delta t [\vec{a}(t) + \vec{a}(t + \delta t)] \quad (\text{III.25})$$

For velocity by Eq. III.22;

$$\vec{a}(t + \delta t) - \vec{a}(t) = \delta t \vec{b}(t)$$

subs. into eq. III.21;

$$\vec{v}(t + \delta t) = \vec{v}(t) + \delta t \vec{a}(t) + \frac{1}{2} \delta t [\delta t \vec{b}(t)]$$

then it takes the form Eq. III.25.

After computing the total forces for each atom, calculating accelerations by;

$$\vec{a}_i(t) = \frac{\vec{f}_{tot,i}(t)}{mass}$$

Next to find new positions use these calculated accelerations on Eq. III.24.

Then again compute the total forces for each atom according to the new coordinates to find new accelerations by:

$$\vec{a}_i(t + \delta t) = \frac{\vec{f}_{tot,i}(t + \delta t)}{mass}$$

Last is to compute the new velocities by Eq. III.25.

III.7 MD Time Step

It is investigated for the optimal value of the time step during Molecular Dynamics Simulation. The scheme in the Appendix D is used for the value of time step and then multiples of this number is checked by doing simulations.

Several values are used, namely from 0.02 fs to 5 fs, see the figures III.1–III.3.

It is found that after the value of 2 fs the simulation becomes instable and for the value of 5 fs the structural stability of tube is not sustained any more. It is decided to use 1 fs value for the Molecular Dynamics Time Step (MD Time Step).

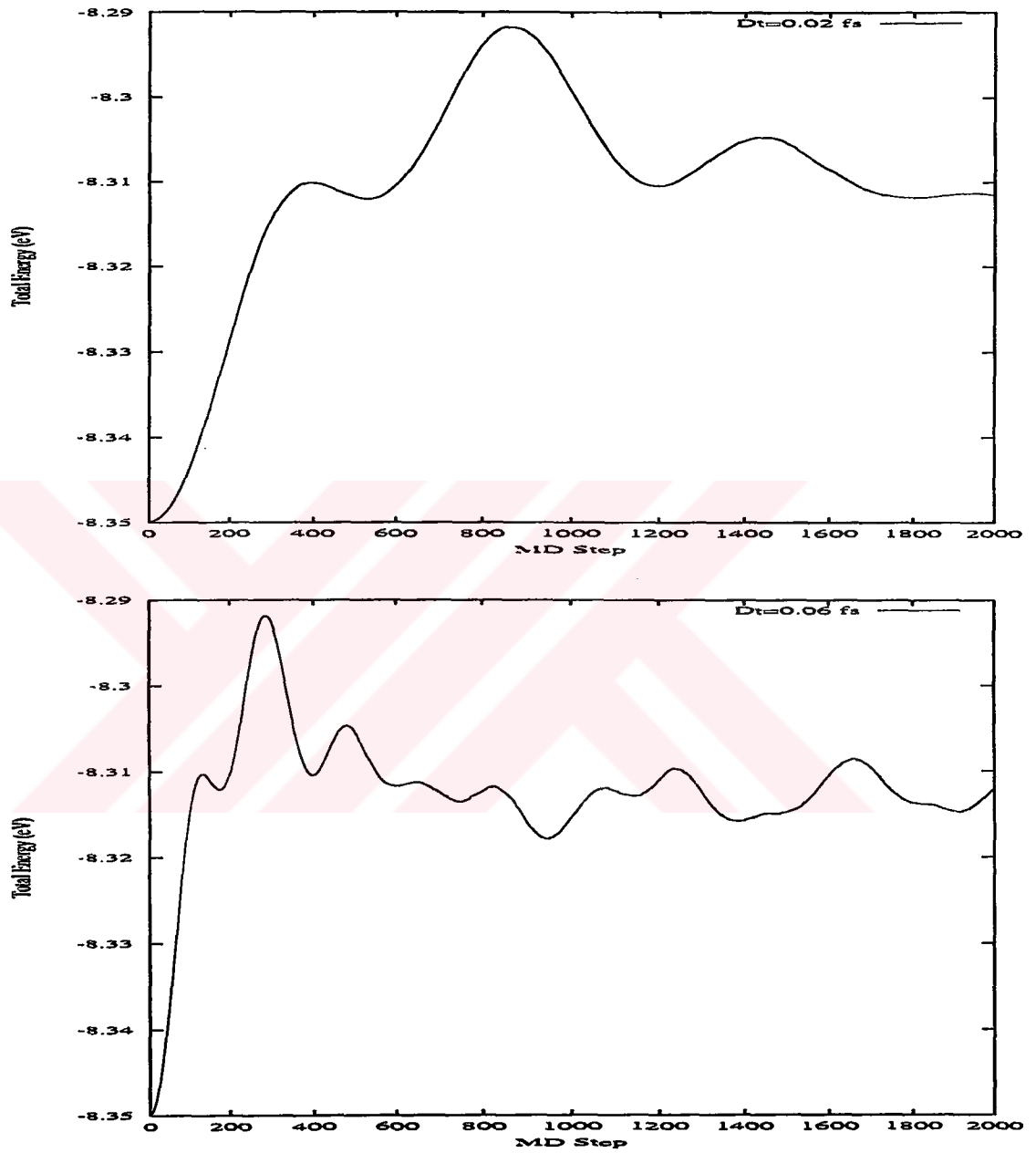


Figure III.1: The Total Energy versus MD Steps for the tube 10x10 (20 layers, $T=300$ K, electronic temperature is 0.005 eV) for the Δt values of 0.02 and 0.06 fs, respectively.

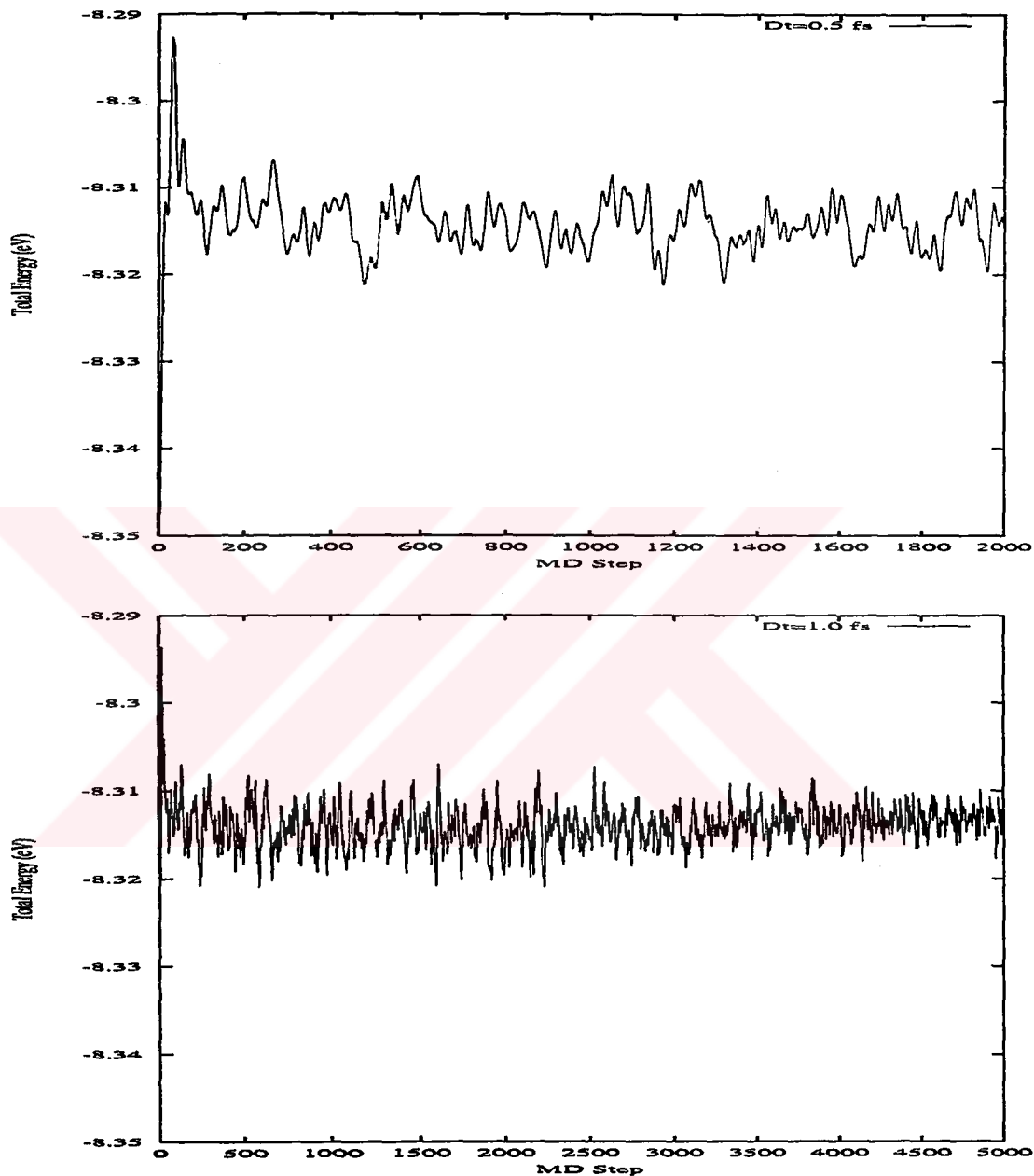


Figure III.2: The Total Energy versus MD Steps for the tube 10x10 (20 layers, $T=300$ K, electronic temperature is 0.005 eV) for the Δt values of 0.5 and 1 fs, respectively.

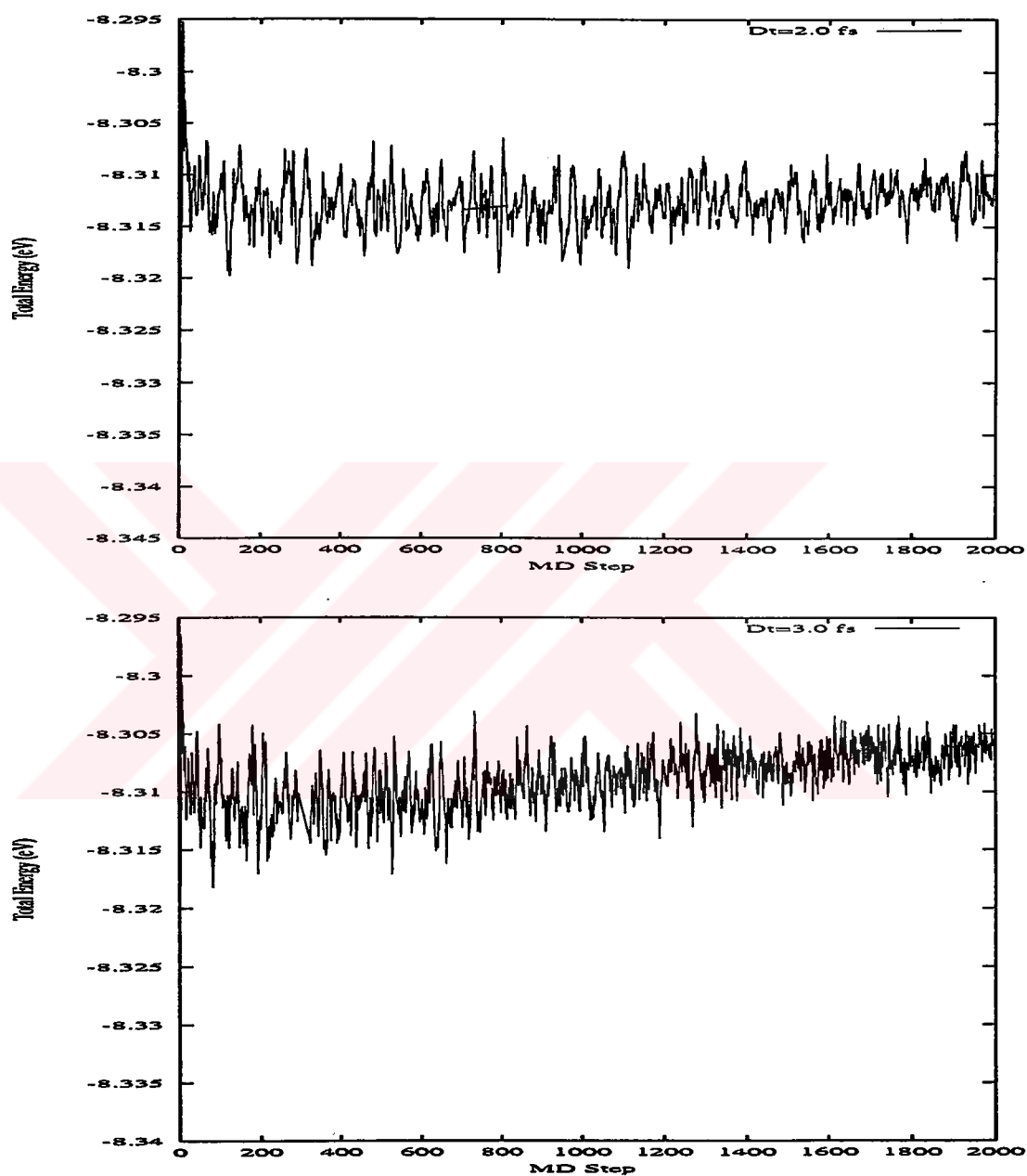


Figure III.3: The Total Energy versus MD Steps for the tube 10x10 (20 layers, $T=300$ K, electronic temperature is 0.005 eV) for the Δt values of 2 and 3 fs, respectively.

III.8 Parallelization

Simulation of molecular dynamics (MD) systems can be speed up considerably by parallelizing the existing codes for distributed memory machines. In classical MD the CPU time is typically function of the square of the number of atoms. The size of the molecular system which can be solved is therefore often limited by the CPU available. There are different approaches for reducing computation time. One consists in parallelizing sequential $O(N^2)$ algorithms. The other is replacing the calculation of non-bonding forces by a less complex algorithm which can then be parallelized [24, 25].

One of the standard ways of classifying computer systems is that proposed by Flynn (1972),

- SISD Single Instruction Single Data

Sequential

- SIMD Single Instruction Multiple Data

Parallel and synchronous, two cases; SM Shared Memory and ICN Interconnection Network

- MISD Multiple Instruction Single Data

Practically not useful

- MIMD Multiple Instruction Multiple Data

Parallel and non synchronous, again two cases; SM and ICN. Most powerful and most general.

Computational scientists have emphasized two phases of molecular dynamics simulation, namely, the computation of force interactions and the integrations of the Newton's equations of motion describing the time evolution of the atoms in the system. Since particles interact pairwise, computational time for the force interactions, assuming equal pairwise interactions, is proportional to $N(N - 1)/2$, where N is number of particles in the system. This becomes less computationally manageable for large N , numerical experiences have indicated that the force calculations constitute approximately ninety percent of the entire simulation time. Recently, systems with more than one hundred million particles have been simulated. These simulations are made possible by improvements in parallel decomposition algorithms and parallel computer hardware (SIMD and MIMD). Message-passing interface libraries such as PVM [26], Linda and MPI are making possible simulations on clusters of computers.

There are currently three types of parallel decomposition algorithms, namely: domain, atom, and force decompositions [27]. In the domain-decomposition approach particles are distributed to processors based on their positions in the computational domain. Atom-decomposition techniques assign particles to processors irrespective of their positions in the computational domain. Force-decomposition methods distribute components in the skew-symmetric, (sparse, when cutoff radius is assumed) force matrix processors.

Two theoretical indices have been used for meaning the performance of a parallel algorithms

$$\text{Speed up} : S_p = T_1/T_p \quad (\text{III.26})$$

where T_p is the time required for the calculation on a p-processor machine,
and

$$\text{Efficiency} : E_p = S_p/p \quad (\text{III.27})$$

The theoretical maximum value of S_p appears to be p (and of E_p to be 1)
attained when the algorithm is fully parallel and the calculation is distributed
equally among the p-processors.

III.9 Example about PVM

This is the program segment that shows how to send and receive data between
processors by using PVM and Fortran.

```
call pvmfpack(REAL8,rr2(ii+1:ii+ntask,1:n),n*ntask,1,info)
```

data is being packed,

```
call pvmfsend(tids(i),msgtype,info)
```

sent to processors,

.
. .
. . .

necessary calculation is being done by using this data,

```
call pvmfrecv(tids(i),msgtype,info)
```

it is received,

```
call pvmfunpack(REAL8,eri(fatom:latom),ntask,1,info)
```

calculated data is located in the respective dimension.

CHAPTER IV

RESULTS

IV.1 $O(N)$ Tight Binding MD Simulations

Traditional TB solves the Schrödinger equation in reciprocal space by direct matrix diagonalization, which results in cubic scaling with respect to the number of atoms. The $O(N)$ methods solve for the band energy in real space and make the approximation that only the local environment contributes to the bonding, and hence band energy, of each atom. All the $O(N)$ methods in which the properties of the whole system are computed (for instance, the charge distribution, the total energy or the forces on all atoms), provide necessarily approximations to the exact solution of the effective one-electron Hamiltonian. These approximations are based on physical assumptions, which are generally connected to the above mentioned locality or nearsightedness principle in one way or another. Most of the implementations of the $O(N)$ procedure have been developed for the orthogonal tight-binding Hamiltonian. The $O(N)$ techniques may be roughly grouped into two categories: variational methods and moment-based methods. There are two types of variational methods: the

density matrix methods and localized orbital methods. There is also a variety of moment methods. The $O(N)$ scaling, in these approaches, arises from the decay and/or truncation of these respective quantities [28]- [30]. It is worth noting that usually $O(N)$ schemes can be efficiently parallelized through the use of message passing libraries. In this study, we used the divide and conquer (DAC) approach (variational method; the density matrix method). The divide and conquer approach proposed by Yang [30]-[32] was the first linear-scaling method used to carry out quantum calculations. The basic strategy of this method is as follows: divide a large system into many subsystems, determine the electron density of each subsystem separately, and sum the corresponding contributions from all subsystems to obtain solely from the electron density [33]. Each subsystem is described by a set of local basis functions, instead of the entire set of atomic orbitals. The accuracy of the description is enhanced by the use of basis functions of neighboring atoms. These neighboring atoms are called *buffer*. The Schrödinger's equation of the buffer has the same form as in Eqn. III.3. The eigenvalues and vectors are found by diagonalizing Hamiltonian Matrices for the each subsystem.

\mathcal{N} : *number of atoms in the buffer region*

N : *number of atoms in the subsystem*

N_{Cell} : *The number of subsystem*

α : *subsystem*

P^i : *projection of i^{th} electron*

$O^i \equiv f((\mathcal{E}_i - \mu)/k_B T)$: *occupation of i^{th} electron*

n : number of atoms in the system

$\mathcal{N}\mathcal{N}$: number of atoms in the buffer region

that are in the interaction distance (cutoff)

So,

$$P^i = \sum_{j=1}^{4N} |H(j, i)|^2 \quad (\text{IV.1})$$

where $H(j, i)$ is the ji^{th} eigenvector after diagonalization scheme.

$$O^i = \frac{2}{1 + f((\mathcal{E}_i - \mu)/k_B T)} \quad (\text{IV.2})$$

$$\rho_\alpha^i \equiv P^i * O^i = \frac{2}{1 + f((\mathcal{E}_i - \mu)/k_B T)} * \sum_{j=1}^{4N} |H(j, i)|^2 \quad (\text{IV.3})$$

then subsystem density;

$$\rho_\alpha = \sum_{i=1}^{4N} \rho_\alpha^i \quad (\text{IV.4})$$

$$\text{trace} = \sum \rho_\alpha \quad (\text{IV.5})$$

Trace must be equal to number of electrons in the system; then for the error:

$$\text{error} = \text{trace} - 4 * n \quad (\text{IV.6})$$

where,

$f(x) = 1/(1 + \exp(x))$ is the Fermi function, μ is the chemical potential for the electrons, k_B is the Boltzmann constant, and T is the temperature of the electrons. If the error value is not desired accuracy within the desired electron temperature; the chemical potential is recalculated as the following:

$$\mu_{\text{new}} = \frac{-\text{error}}{d\rho} + \mu \quad (\text{IV.7})$$

where,

$$d\rho = \sum_{i=1}^{N_{Cell}} \sum_{i=1}^{4N} [(O^i * P^i) * (1 - O^i)/k_B T] \quad (IV.8)$$

This procedure is repeated until the desired level of accuracy is gained. The final value for the chemical potential is the Fermi Energy Level of the system.

The band structure energy of the system is calculated as:

$$E_{bs} = \sum_{\alpha=1}^{N_{Cell}} ebstot_{\alpha} \quad (IV.9)$$

where, $ebstot_{\alpha}$ is the contribution of the subsystem to the band structure energy of the system:

$$ebstot_{\alpha} = \sum_{j=1}^{4N} \left[\left(\sum_{j=i+1}^{4N} 2 * density_{\alpha}(i, j) * \mathcal{H}(i, j) \right) + density_{\alpha}(i, i) * \mathcal{H}(i, i) \right] \quad (IV.10)$$

where,

$$density_{\alpha}(k, j) = \sum_{j=1}^{4N} \left[\left(\sum_{k=j}^{4N} \sum_{i=1}^{4N} H(j, i) * H(k, i) * O^i \right) + \left(\sum_{k=4N+1}^{4N} \sum_{i=1}^{4N} 0.5 * H(j, i) * H(k, i) * O^i \right) \right] \quad (IV.11)$$

and $\mathcal{H}(i, j)$ is the ji^{th} element of the Hamiltonian matrix of the subsystem.

The next step is to find the forces that each atom experiences arising from the electronic structure, i.e. in the x-direction;

$$f_{xj=1...n}^{\alpha} = \sum_{\alpha=1}^{N_{Cell}} \sum_{i=1}^N f_{x_i}^{\alpha} \quad (IV.12)$$

where;

$$f_{x_i}^{\alpha} = \sum_{j=1}^{NN} \sum_{im=1}^4 \sum_{jm=1}^4 density_{\alpha}(4(i-1) + im, 4(j-1) + jm) * Force(im, jm) \quad (IV.13)$$

where $Force(im, jm)$ has the same form as in Eqn. III.13. Total energy of the system has the form,

$$E_{tot} = E_{bs} + E_{rep} \quad (IV.14)$$

where E_{rep} has the same form as in Eqn. III.14. The energetics and forces are now calculated and then molecular dynamics scheme is applied and this procedure is continued until structural stability is sustained.

IV.1.1 The Periodic Boundary Condition (PBC) and the Effect of the Buffer Size on O(N) TBMD, Carbon Nanotube Simulation

An important parameter in the simulation is the cuboidal box size. We took the cube size equal to the distance between the layers in the tube so that each cube has equal amount of atoms. This also provides the same number of interacting neighbor atoms (buffer) for each subsystem. The PBC is applied in the z -direction only. Hence, the system behaves as infinitely long tube. In the Fig. IV.1, it is seen that the difference with $O(N^3)$ total energy result for 18 layers and 24 layers are exactly same, since PBC works well. We have chosen 20 layers for both 10x10 and 17x0 tube structures for the rest of our study.

Buffer atoms are selected using a distance criterion, R_b . That is, if an atom is within a distance R_b of a subsystem, this atom will be included as buffer atom for that subsystem. The diagonalization for a subsystem is performed with atomic basis functions of the subsystem atoms and buffer atoms, and the computational effort scales as N_α^3 , where N_α is the number of basis func-

tions in the α subsystem and its buffer region. After diagonalization resulting eigenvalues and eigenvectors give us necessary information for local Density of States (IDOS) and for force expressions to evaluate the next MD iteration.

In Fig. IV.1, the effect of the buffer size on the total energy within the given constraints such as boxsize, electronic temperature is given. It is seen that the effect of the buffer size on the $O(N)$ TBMD is very important. For the 10×10 CNT difference with $O(N^3)$ TBMD result (error) decreases when the buffer size is increased; then reaches to desired accuracy and fluctuates around this value. Buffer size is important in evaluating the simulation time, energy and force values. Such as, if the buffer size is chosen a higher value than necessary, it will affect the simulation time in cubic manner since the Hamiltonian matrix is constructed with respect to the number of interacting atoms in the buffer region. On the other hand, if this parameter is chosen a low value then it will not be able to produce the correct energy and force values. In Figs. IV.3 and IV.4, the effect of the buffer size on the $O(N)$ TBMD for the 10×10 and 17×0 tube structures together with the effect of the electronic temperature are also given.

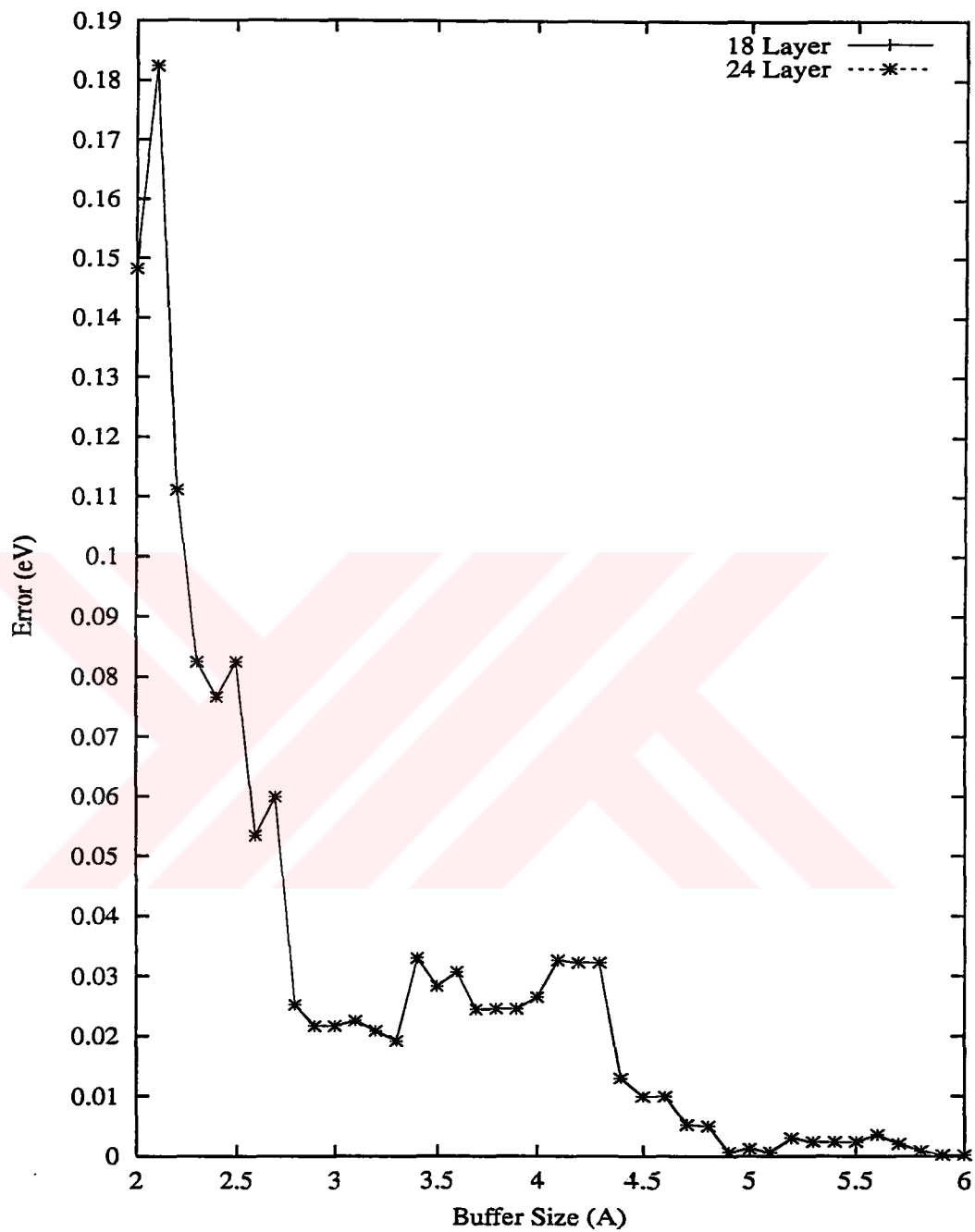


Figure IV.1: The difference of $O(N^3)$ total energy result (-8.350497775) with $O(N)$ total energy result for the variation of $O(N)$ parameter (Buffer Size) for the 24 Layers and 18 Layers 10x10 Tube with box size is equal to 1.229 Å , the electronic temperature is $k_B T = 0.005$ eV.

IV.1.2 The Effect of the Electronic Temperature ($k_B T$) on O(N) TBMD

The effect of the electronic temperature on the total energy is investigated. The energetics for the pristine 10x10 tube with different electronic temperature values $k_B T = 0.025 \text{ eV}$ ($\approx 300 \text{ K}$) and $k_B T = 0.05 \text{ eV}$ ($\approx 600 \text{ K}$) are studied. Results are given in the Figure IV.2. The upper graph is for the room temperature and the lower is the twice of the room temperature. Having an equal average energy value both graphs show similar behavior. They fluctuate around almost the same value. This is reasonable because they both simulate the same system with different electronic temperatures. The pattern at the above graph is more dense than the lower one. This is because of the hotter electrons in the system.

In the Figs. IV.3 and IV.4, the effect of the buffer size together with the varying electronic temperatures (from $k_B T = 0.000001 \text{ eV}$ ($\approx 0.012 \text{ K}$) to $k_B T = 0.1 \text{ eV}$ ($\approx 1200 \text{ K}$)) on the O(N) TBMD total energy value for the 10x10 and 17x0 tube structures are given. It is seen that when the buffer size value is small, electronic temperature has a slight effect on the energy value.

These values are the static results without performing simulation. The effect of the electronic temperature may be impressive during the simulation, when the forces between the atoms become dynamic. Therefore during simulations, it is safe to choose the electronic temperature as room temperature.

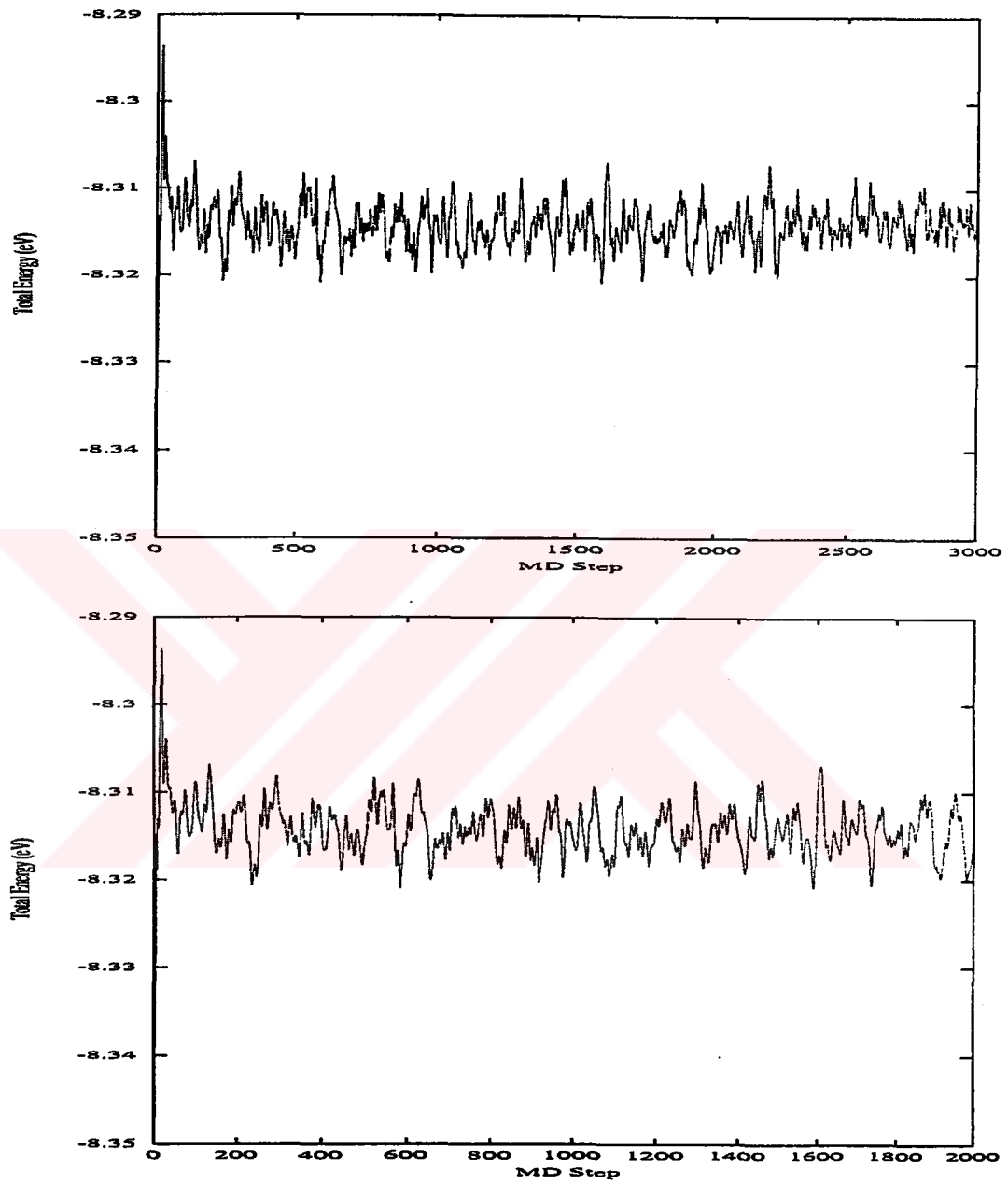


Figure IV.2: The effect of electronic temperature on the total energy (Tube 10x10 no strain $T = 300$ K) for the values $k_B T = 0.025$ eV and $k_B T = 0.05$ eV, respectively.

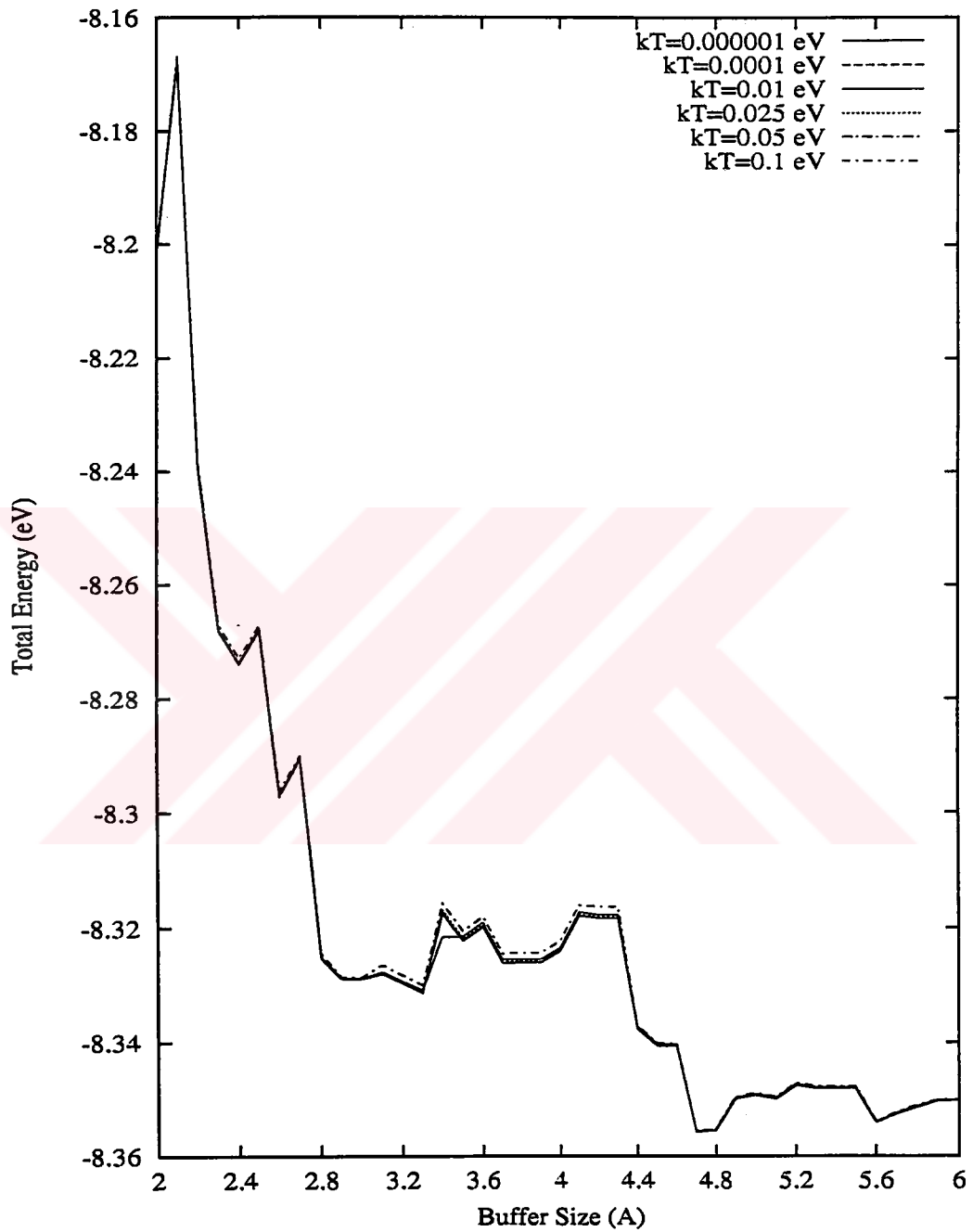


Figure IV.3: The effect of Buffer Size for the Total Energy value for the tube structure 10x10, with different electronic temperature values, respectively.

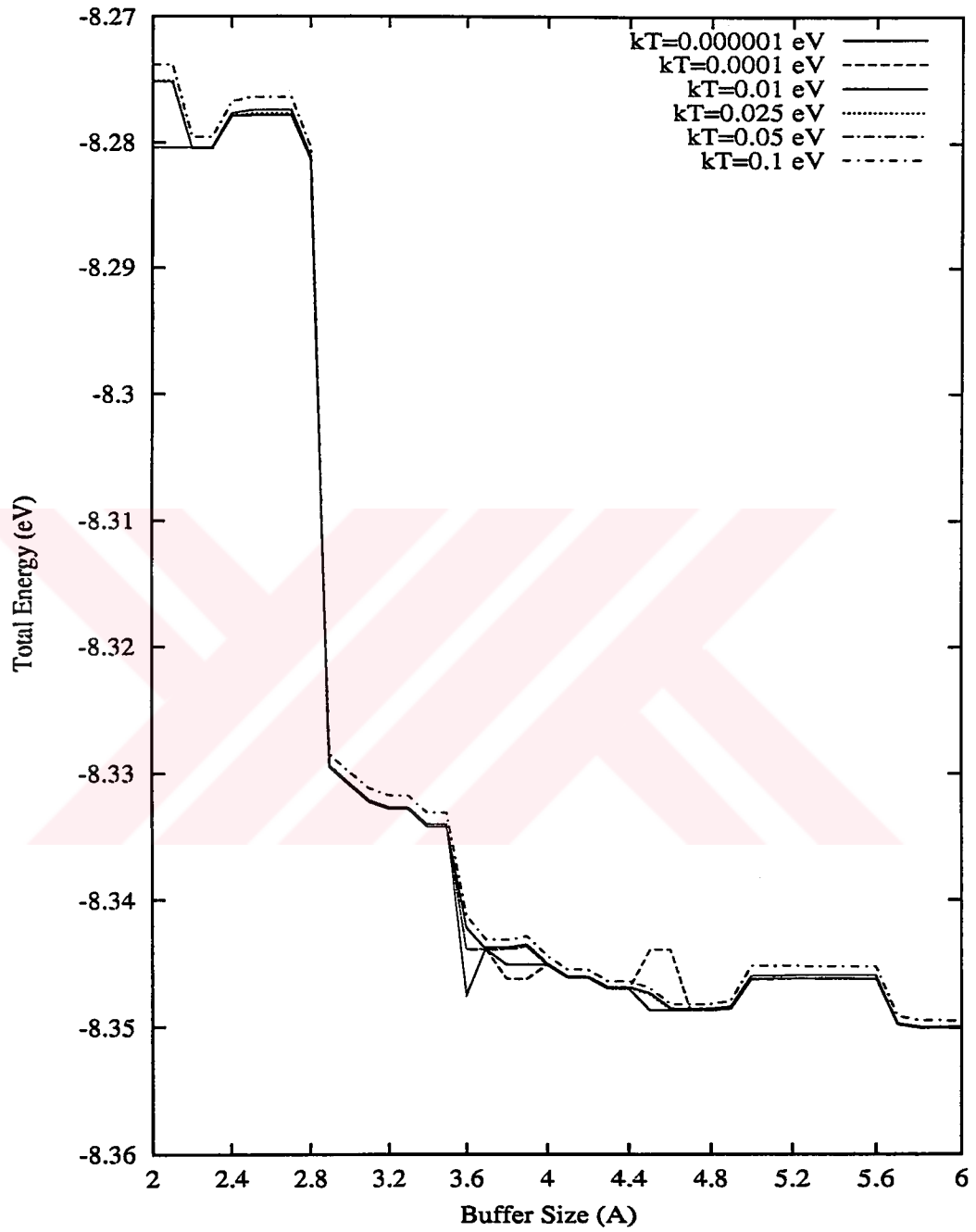


Figure IV.4: The effect of Buffer Size for the Total Energy value for the tube structure 17x0, with different electronic temperature values, respectively.

IV.1.3 The Effect of the Electronic Temperature ($k_B T$) on Fermi-Dirac Distribution and on Local Density of States

The effect of the electronic temperature on Fermi-Dirac Distribution and on Local Density of States (LDOS) is investigated. The Fermi-Dirac Distribution of the pristine 10x10 and 17x0 tubes with different electronic temperature values $k_B T = 0.01 \text{ eV}$ ($\approx 120 \text{ K}$) and $k_B T = 0.1 \text{ eV}$ ($\approx 1200 \text{ K}$) are studied. Results are given in the Figs. IV.5 and IV.6. The upper graphs in the figures are at 120 K while the lower ones are at 1200 K. It is observed that as the electronic temperature is increased the graphs are broadening. Since less electronic state is populated at the low electronic temperature condition there is no widening for the upper graphs as expected.

The density of states is obtained from the general formula,

$$g(\mathcal{E}) = \frac{dN(\mathcal{E})}{d\mathcal{E}} = \frac{N(\mathcal{E} + \epsilon) - N(\mathcal{E})}{\epsilon} \quad (\text{IV.15})$$

where N is the number of electrons in the system and equal to,

$$N(E) = \sum_{i=1}^{N_{\text{Cell}}} \sum_{j=1}^{4N} \frac{2}{1 + f((E - \mathcal{E}_i)/k_B T)} * \sum_{j=1}^{4N} |H(j, i)|^2 \quad (\text{IV.16})$$

In the Eq. IV.15, the statement is that; if there is a change in the slope this gives us the information about the existence of populated electronic state. The criteria is the change in the slope for the Figs. IV.7 – IV.10.

In the Figs. IV.7 – IV.10, the LDOS graphs for the pristine 10x10 and 17x0 tubes for different electronic temperature values $k_B T = 0.1 \text{ eV}$ ($\approx 1200 \text{ K}$), $k_B T = 0.05 \text{ eV}$ ($\approx 600 \text{ K}$) and $k_B T = 0.025 \text{ eV}$ ($\approx 300 \text{ K}$); respectively are given. In the Figs. IV.7 and IV.9, only a selected

range for IDOS are given to better understanding of the behavior of electronic states near the Fermi–Energy level for the tube structures 10x10 and 17x0, respectively. The other figures, namely IV.8 and IV.10, give the same information but in the full range. It is seen that when the electronic temperature is increased the graphs begin to be smoother since higher amount of electronic states are populated. But, the peaks at and around the Fermi–Energy level are at the same positions for different electronic temperatures as expected.

The Fermi–Energy level values are very similar (around 3.7 eV) for both tube structures. Although they have different chirality this is expected because two tubes have the same radii. The formula for the DOS gives the electronic state population for the different energy values. It is found that the 10x10 tube has metallic behavior since it has states around Fermi–Energy level and a wide band gap but on the other hand the 17x0 tube has semiconducting behavior since it has no states around Fermi–Energy level and small band gap as expected.

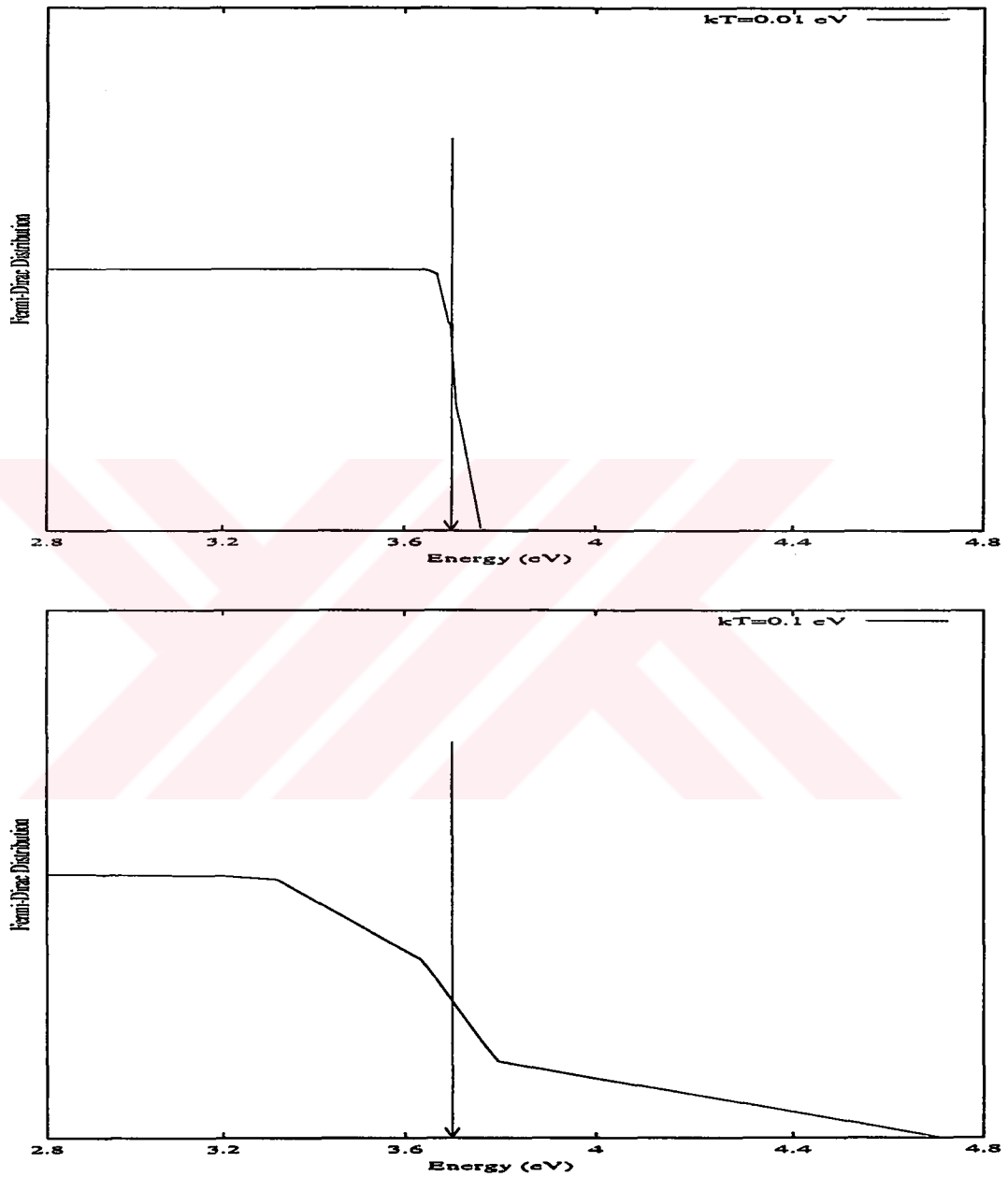


Figure IV.5: Fermi-Dirac Distribution Function vs Energy for various electronic temperatures for the Tube Structure 10x10.

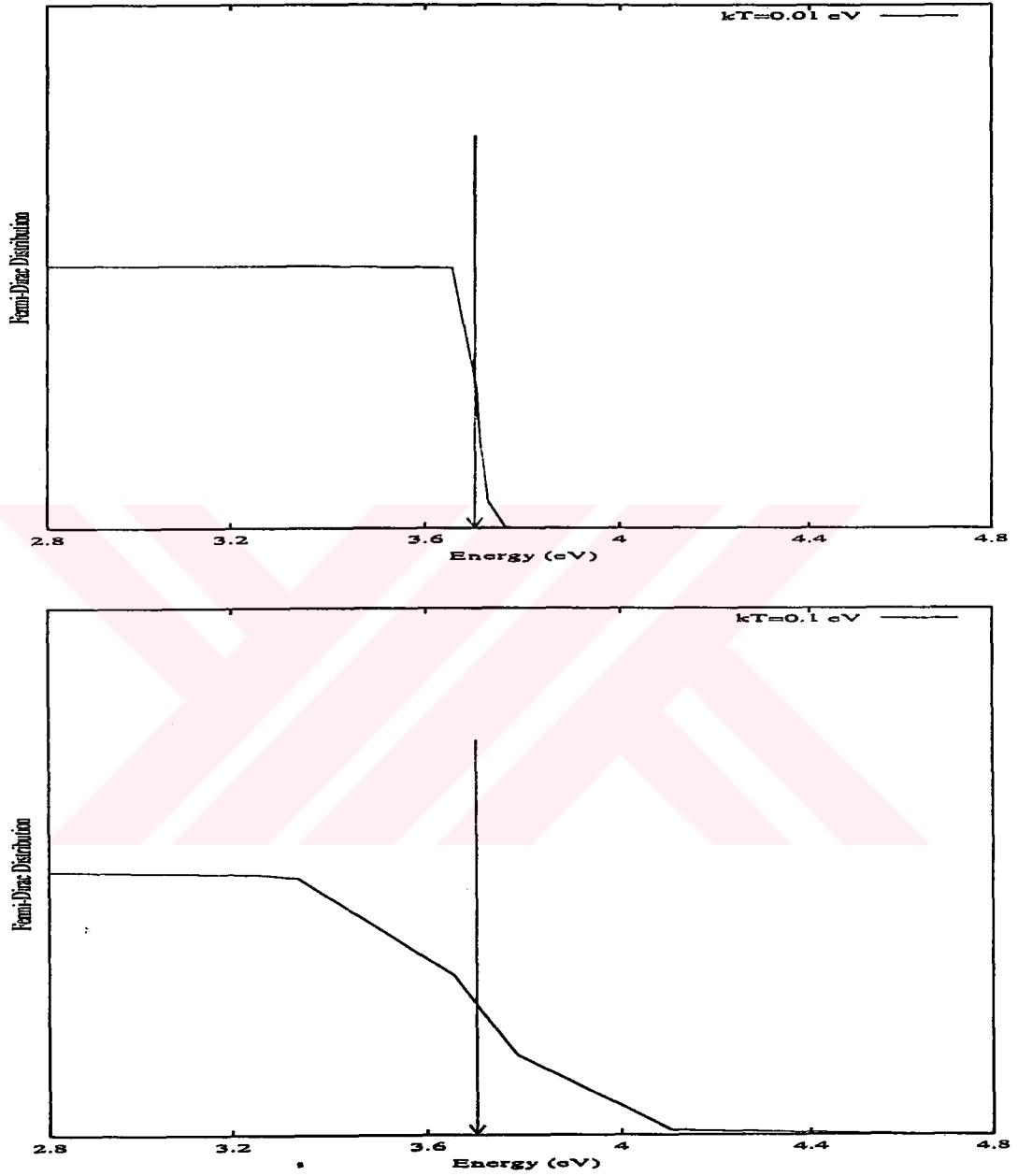


Figure IV.6: Fermi-Dirac Distribution Function vs Energy for various electronic temperatures for the Tube Structure 17x0.

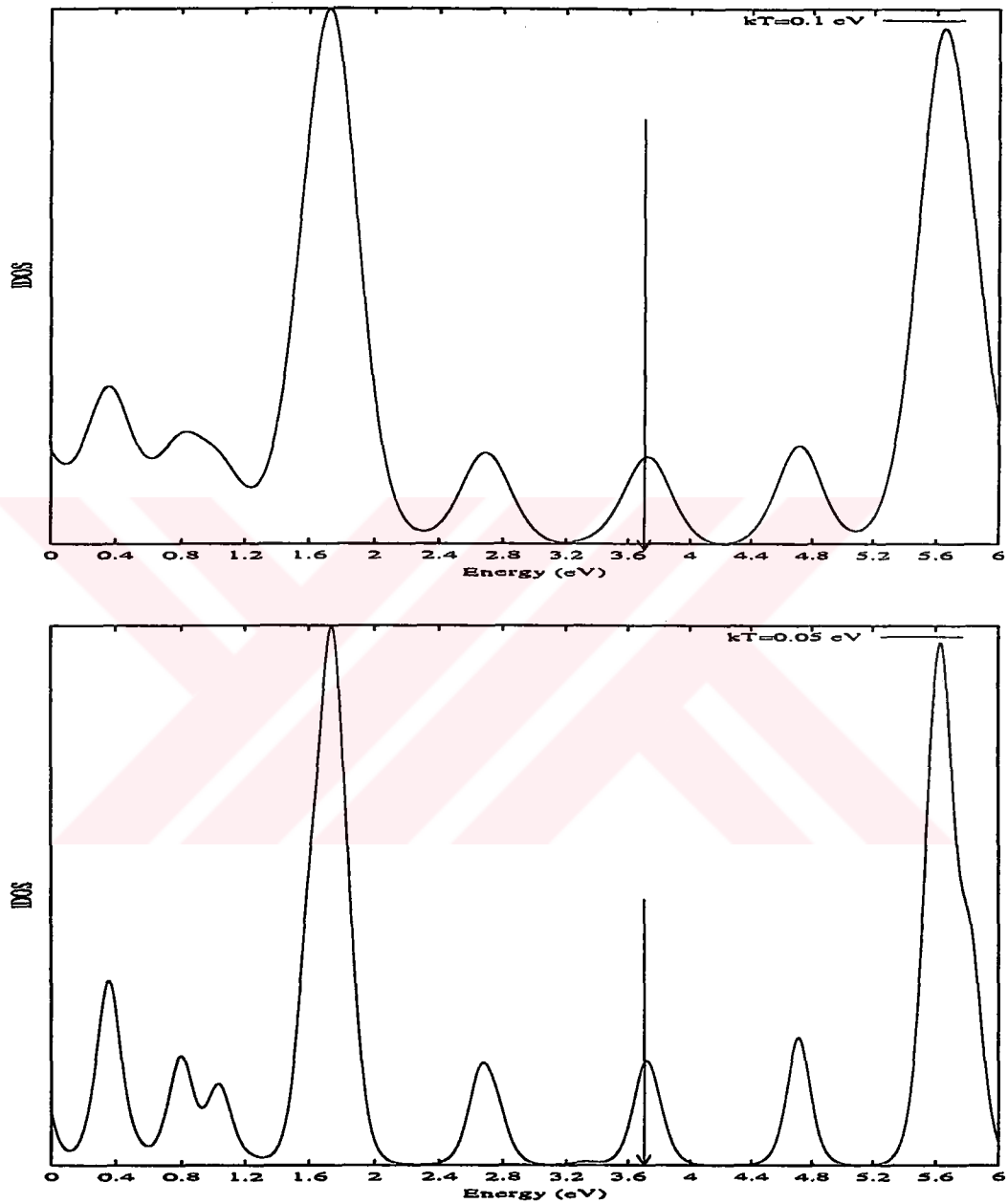


Figure IV.7: Local DOS vs Energy for different electronic temperatures for the Tube Structure 10x10..

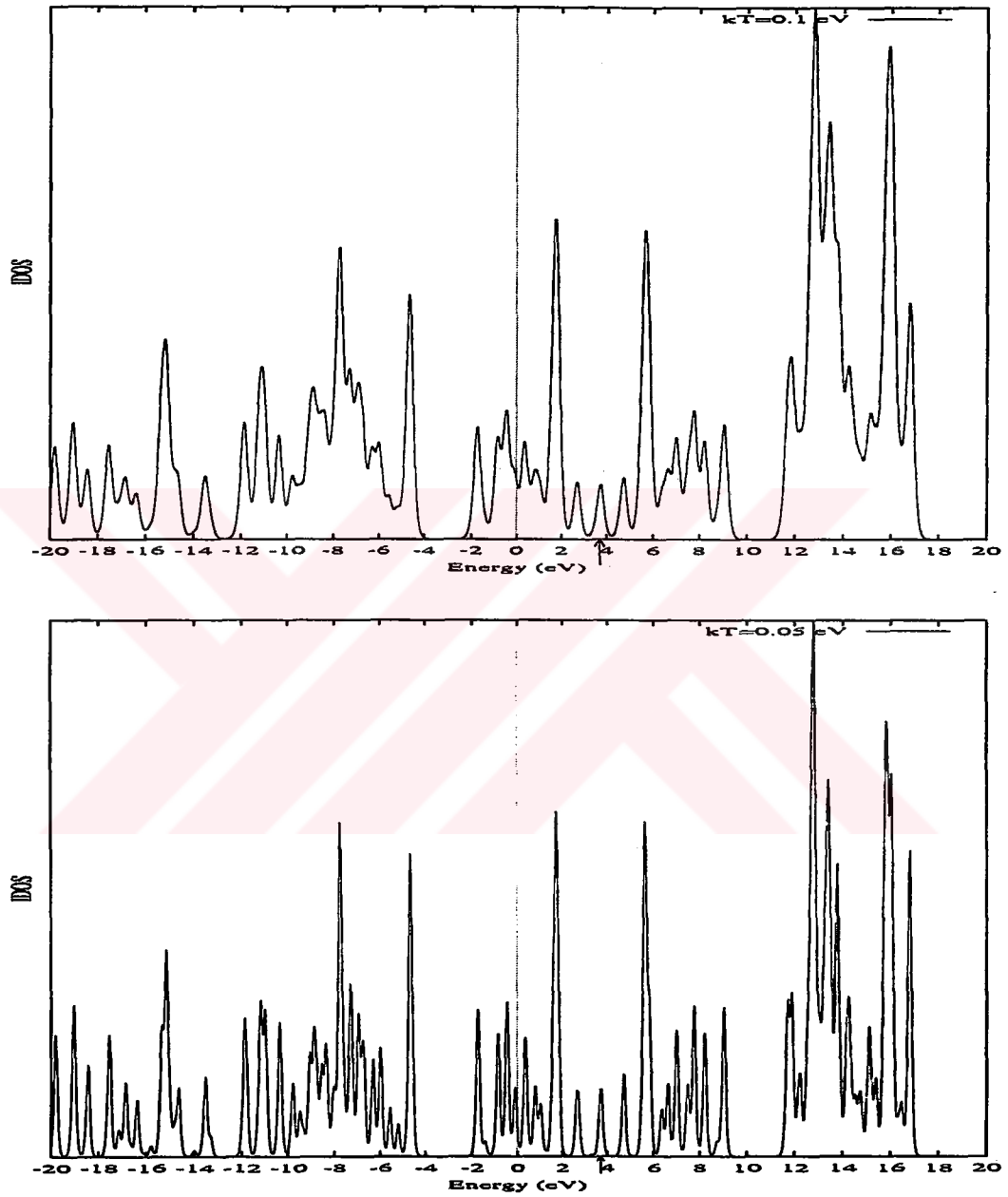


Figure IV.8: Local DOS vs Energy for different electronic temperatures for the Tube Structure 10x10

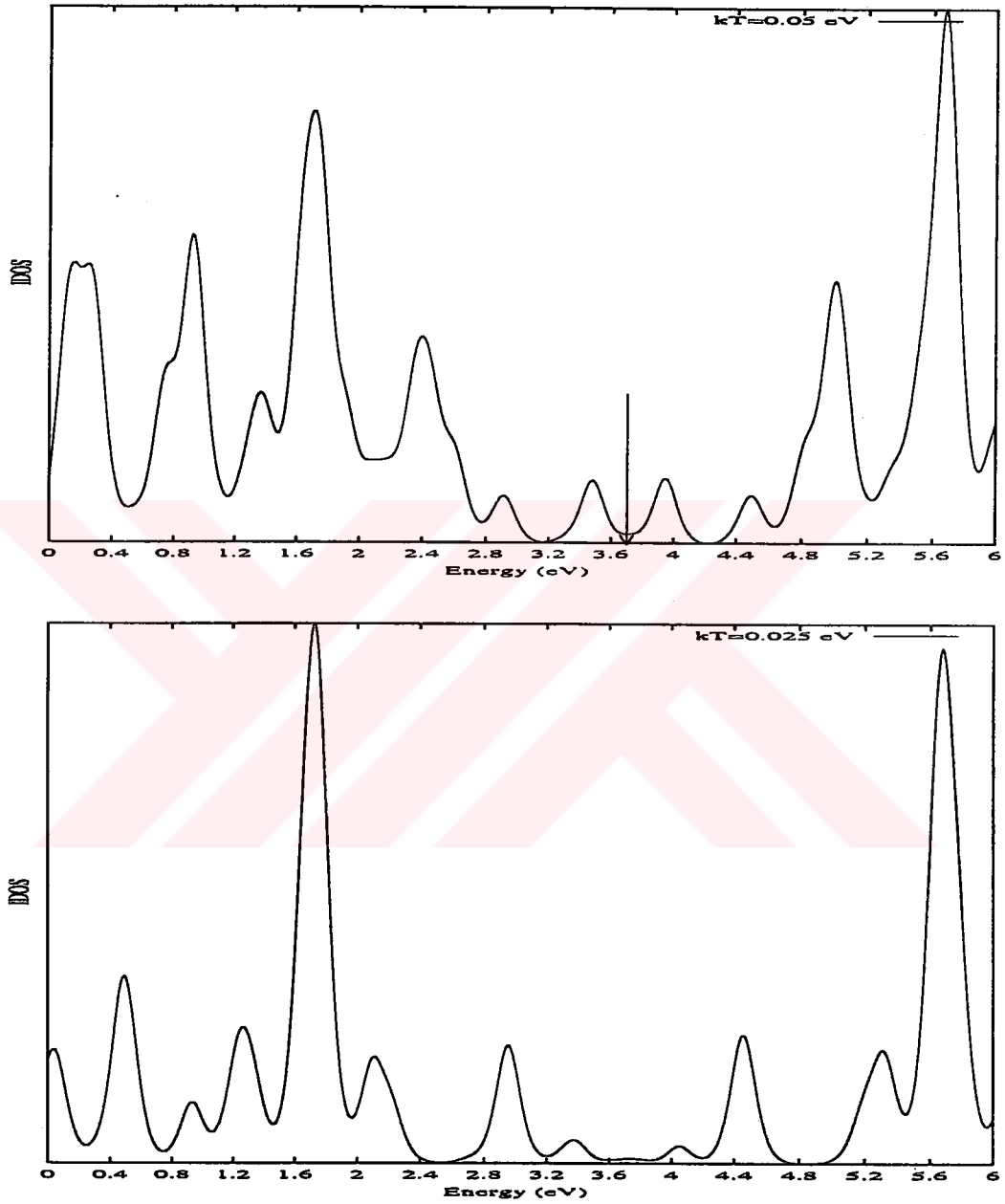


Figure IV.9: Local DOS vs Energy for different electronic temperatures for the Tube Structure 17x0.

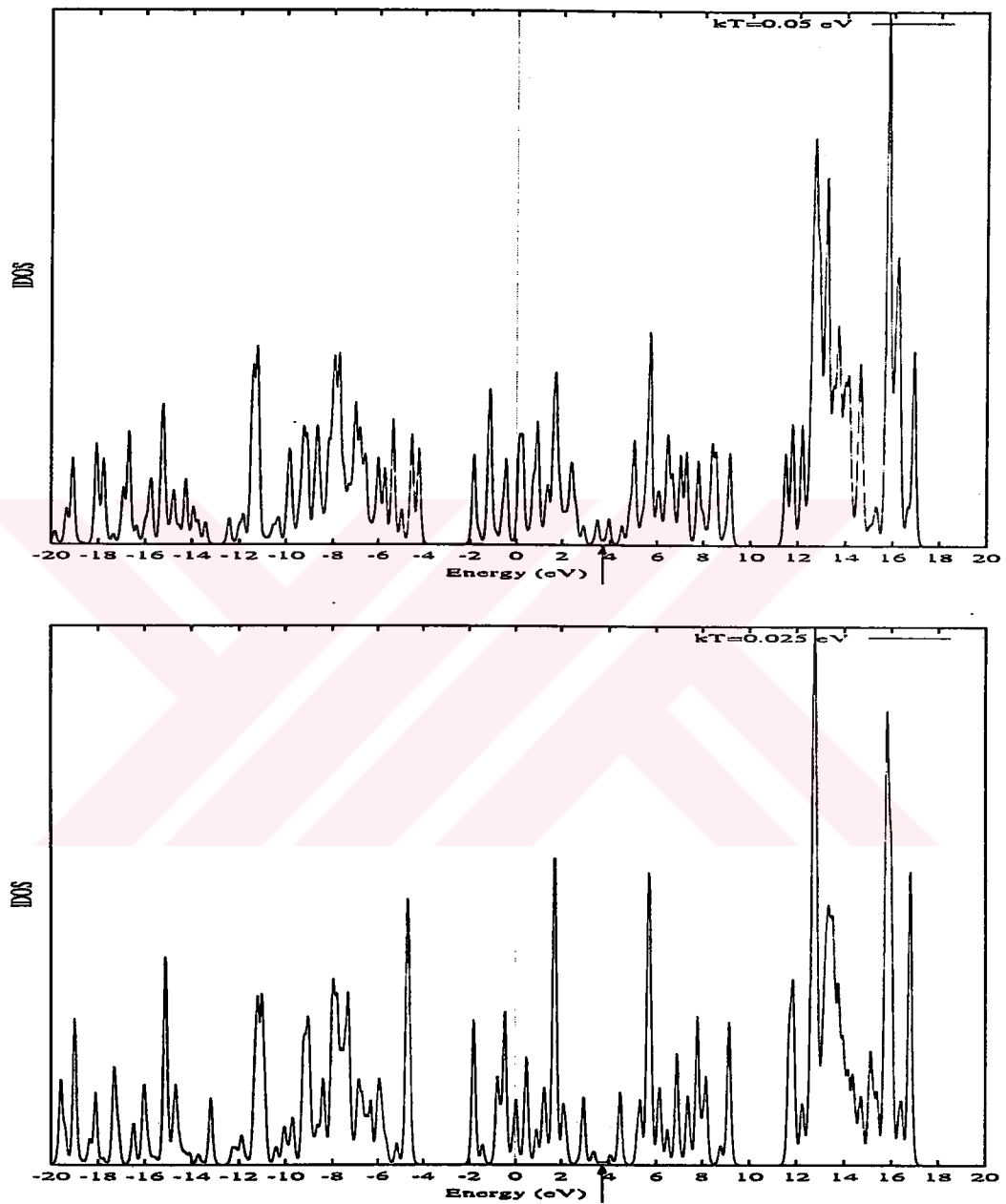


Figure IV.10: Local DOS vs Energy for different electronic temperatures for the Tube Structure 17x0.

IV.1.4 Discussion

In this study, the details of $O(N)$ TBMD algorithm is given. It is described that how a system is divided into many subsystems and how their contributions give overall system properties (such as charge density, band structure energy) by using nearsightedness principle. This principle uses the approximation that only the local environment contributes to the bonding of each atom. This gives us the opportunity for linear scaling. The main problem in the traditional TB is the increasing system size. When the system size increases (N), the time to diagonalize the constructed Hamiltonian matrix becomes in the order of N^3 . The $O(N)$ algorithms overcome this bottleneck and the behavior has a linear scaling. In the Fig. IV.13, it is seen that our $O(N)$ algorithm scales linearly for increasing system size.

The effect of some $O(N)$ parameters is studied. The first one is the buffer size. Each subsystem has its own buffer region so that its own small sized Hamiltonian matrix. After diagonalizing this Hamiltonian matrix, the eigenvalues and eigenvectors are obtained. The next step is to obtain all these informations for all subsystems and then calculate the overall system property; chemical potential. This parameter gives us the value for Fermi-Energy Level. Then, the forces that each atom experiences and the contribution of each subsystem to band structure energy of the system are calculated. All these procedures are repeated through each MD time step.

The results obtained with $O(N)$ algorithm must be consistent with $O(N^3)$ results for the same system. To ensure this, the value for the buffer size

parameter must be investigated. The results for this parameter are given in the Figs. IV.3 and IV.4. In Fig. IV.3, the buffer size for 10x10 tube is studied and it is feasible to choose it as 4.9 Å. Also, the value of the parameter for the 17x10 tube can be taken as 5.7 Å (see Fig. IV.4). It is important to keep the buffer size parameter as small as possible and at the same time, it must be able to produce the same values with the $O(N^3)$ TBMD results. The buffer size for 17x0 tube converges to desired accuracy much later than 10x10 tube. This results in much longer simulation time.

We have applied PBC in z-direction only and checked it in 10x10 tube structure with different sizes. The result can be seen in the Fig. IV.1. It is seen that PBC condition works well.

Another important parameter in the simulation is the electronic temperature. We have investigated the effect of the electronic temperature on the MD simulation and obtained the results given in Fig. IV.2. It is observed that higher electronic temperature does not affect the average value of the total energy but it may be effective for the extreme cases such as strain and vacancy. Therefore, we have chosen the electronic temperature as room temperature value for the rest of the study.

It is also studied that the effect of the electronic temperature on the buffer size value is not considerable after the desired accuracy on the buffer size is reached. We have also calculated the band gap values for 10x10 and 17x0 tubes as 2.01 eV and 0.53 eV; respectively. The proposed model values are calculated by the formulas $2\gamma_0 a_{c-c}/d$ and $6\gamma_0 a_{c-c}/d$ (where $\gamma_0 = 2.5 - 2.7$ eV, $a_{c-c} =$

0.142 nm , and d for diameter in (nm)) for semiconducting and metallic tubes, respectively [20],[34]-[37]. The band gap values for the 10x10 and 17x0 Carbon Nanotubes with this model are 1.62–1.75 eV and 0.54–0.58; respectively. Our $O(N)$ TBMD algorithm gives good energy band gap result for the 17x0 tube but not so good for 10x10 tube compared to the proposed models mentioned above. On the other hand, the behaviors of the local density of states graphs are (see Figs. IV.7–IV.10) as expected. For the 10x10 tube (metallic behavior), it is wide and there are states populated around Fermi-Energy level and for the 17x0 tube (semiconducting behavior), it is narrow and no states around Fermi-Energy level as expected.

As a result, we conclude that the methodology is able to produce the physical properties such as Fermi-Dirac Distribution, local Density of States and energetics for the Carbon Nanotubes. The next step is to investigate the structural stability under extreme conditions such as uniaxial strain.

IV.2 Parallel $O(N)$ TBMD

We have compared our $O(N)$ TBMD simulation results with $O(N^3)$ TBMD algorithm. Then parallelization technique is applied to $O(N)$ TBMD program. In this work we do not discuss $O(N)$ methods, rather we focus on the algorithm of the sequential $O(N)$ code and parallel version of it. We made use of the TB model by C. H. Xu et al. [22]. sp^3 basis set per C atom is used with cutoff distance for orbital overlap and U_{rep} at 2.1 Å to consider only first nearest neighbor interactions. When using a cutoff for non-bonding forces, it is necessary to construct a list of all pairs of atoms that are within the cutoff distance. This pair list is normally updated after a fixed number of MD steps, typically 10. In particular, the search for interacting pairs (by calculating the distance of separation and comparing these with cutoff radius) is quite expensive, being of the order N^2 , if no special algorithms are applied. To speed-up this process, either the linked-cells (LC) algorithm [16], or a Verlet list [17] (or both) can be used. To build-up the LC list for one type of non-bonded interaction, requires each region to be divided into cells. We have used LC list with equally-sized cells of cuboidal shape and Verlet list together. The linked lists of all the sites within each cell are built, and only interacting pairs within the neighboring cells need to be considered in computing pair interactions. Using this method, the number of extra pairs tested is reduced considerably. Since divide and conquer algorithm [31] for tight binding scheme is used, it is inherently possible to make use of LC technique and apply parallelization algorithm. Velocity Verlet algorithm is used for the time evolution of the system

with a time step equal to 1 fs.

The program was written by using Fortran 77. Functions and subroutines are grouped into modules. Dynamic memory allocation is used for all data structures, there are no compile-time limits for the number of atoms, etc. Benchmark tests has been performed on 8 PCs (Celeron 500 MHz, 128 Mb RAM, 128 Kb cache) running under Linux (Slackware 2.2.13). As a compiler option -O2 optimization level is used. Lapack (level 3) is used for the diagonalization of the Hamiltonian matrix. The flowchart is given in the appendix and the time analysis of the sequential code is given at the results section.

IV.2.1 Algorithm

The overwhelming part of all computation time in an $O(N)$ TBMD simulation is spent for calculation of band structure energy and forces. Our approach does not distribute all parts of TBMD simulation to avoid higher cost of the internode communication time. Instead of that only calculation of band structure energy and forces are distributed to processors, collecting the resulting forces, and doing the rest of the calculation (non-bonding potentials, time integration, velocity rescaling, etc.) on only one processor. This significantly reduces the communication requirements and enables much better scaling to large number of processors. It is the simplest to program as the parallel code loop structures remain essentially the same as the serial code with most of the subroutines remaining almost identical. Master-slave technology is used to parallelize the sequential code. It is a hybrid algorithm of replicated data and

domain decomposition algorithms [38]-[41]. PVM was used for communication between tasks of parallel program. The PVM standard has been widely accepted, is available for all important parallel machines, and makes it possible to write portable parallel programs that run efficiently on both shared memory and distributed memory machines.

In all cases the subroutine DSYEVD was adopted to fully diagonalize the Hamiltonian matrix. DSYEVD was selected for a two-fold reason: it is a diagonalization routine where eigenvectors are calculated by using a divide and conquer algorithm, and it allows for the calculation of the full eigen-spectrum and therefore simulates a real life application of TBMD where the calculation of physical observables depending on electron energies and/or wavefunctions are actually needed. The flowchart is given in the appendix and the time analysis of the parallel code is given at the results section.

IV.2.2 Discussion

In this study, the $O(N)$ technique is applied to sequential $O(N^3)$ TBMD simulation code and then parallelization is applied. Our system is a distributed memory system and contains 8 computer having Celeron processors with fast ethernet (100 Mbit/sec) using bus topology and PVM (Parallel Virtual Machine) library. The parallel code is benchmarked and tested on a physical system, which is 10x10 structured CNT. The number of atoms are related to the increasing layers of 10x10 structured CNT, 4200 atom corresponds to 210 layered CNT (\AA). All the simulations presented herein were carried out

in the canonical (N, V, T) ensemble. The Newton equations of motion were integrated using the Velocity Verlet algorithm with a time step equal to 1 fs. To avoid inaccurate integration of the Newton equations of motion, the velocities of the constituent atoms were occasionally rescaled to maintain the temperature of the system at the target value. Periodic boundary condition is applied in uniaxial direction. The results for sequential and parallel runs are compared and assured that they are the same both in numerical accuracy and in physical aspects. In Figs. IV.11 and IV.12, some physical properties and energetics values for the simulation results on (10×10) tube structure at 300 K are given. In Figure IV.11, simulation results of radial distribution function, particle-particle correlation function, bond angle and bond length distribution functions for (10×10) CNT are given. The radial distribution function defined as the average density of atoms at a given distance from any other reference atom gives the information about the structure of 10×10 tube. In the figure, we observe the first peak at the nearest neighbor distance of $a_{c-c} = 1.44 \text{ \AA}$. The second peak is at the second nearest neighbor distance of 2.49 \AA and the third peak at $2a_{c-c} = 2.88 \text{ \AA}$. These values are all in accord with the observed properties of 10×10 tube [42]. Particle-particle correlation function also gives the same information as Radial Distribution function. Bond-angle distribution function peaks around 120 degree as expected. Bond-length distribution function peaks around 1.4 \AA which is the a_{c-c} distance for the 10×10 tube. In Figure IV.12, we give the coordination number, repulsive energy, band structure energy and total energy for our CNT. The coordination number peaks

around 3 as expected. Total energy reaches equilibrium around -8.30 eV in 250 fs. It fluctuates around this value for another 250 fs. This gives us enough information about the average value of the total energy for 10x10 CNT. The only reported total energy value we could have found in literature is -8.01 eV [43] and in obtaining this value periodic boundary condition is not taken into consideration.

Sequential $O(N^3)$ TBMD scales as cubic power to number of atoms and limited to system size around 600 atoms, however sequential $O(N)$ TBMD enables us to study system sizes around 900 atoms and also linearly scales as can be seen in Figure IV.13. Our test case 10x10 tube structure consists of 400 atoms. Using $O(N^3)$ matrix diagonalization run time per MD Step for this simulation is 573 sec. $O(N)$ algorithm reduces the run time per MD Step to 40 sec. More on the system size studies can be seen in Figs. IV.14 to IV.18.

Run time for parallel $O(N)$ TBMD code also scales as linearly with the increasing number of atoms up to available system sources. It scales linearly with increasing number of atoms and fixed number of processors, and then the slope changes. After that point is reached, it is necessary to add new host to decrease the run time, to have a feasible and efficient system. Another aspect is increasing the number of hosts in the cluster will not always decrease the run time for the same number of atoms. Because the communication between the nodes overheads and increase the run time. These two behavior are seen in Figures. IV.14 and IV.15. The same trend is also observed in the communication time with increasing number of atoms, as can be seen in Figure

IV.16.

Increasing number of processors in the cluster decreases the run time. Exception to this is observed in Figure IV.15 for 200 atoms case. Here the communication time overrides the small calculation time. In Figure IV.17, communication time per MD Step (in units of sec) is analyzed with respect to number of processors. The communication time for fixed number of atom and increasing number of processors shows $O(N_{proc}^3)$ behavior. In Figure IV.18, the percentage contribution of communication time to Run Time is analyzed for varying sizes of processors Since Run Time per MD Step composes of communication and calculation parts. We see that the contribution of communication time to run time increases with the addition of new hosts to cluster as expected. Communication time becomes dominant thus decreasing the calculation time considerably.

Our result for Speed Up and Efficiency are given in Tables IV.2.2 and IV.2.2. The highest Speed up and Efficiency values are 3.71 and 0.98, respectively. Speed Up is defined as $S_p = T_1/T_p$ where T_1 is the time for sequential runs and T_p is the time for runs using p number of processors. Efficiency is obtained using $E_p = S_p/p$. The highest value for speed up is 3.71. This is obtained in the simulation of 20 layer (400 atoms) CNT using 5 processors. Highest value for efficiency is 0.98. It is obtained in the simulation of 20 layer and 26 layer (520 atoms) using 2 processors CNT. In Table IV.2.2, the comparison for the Lapack routines; (to diagonalize Hamiltonian Matrix), dsyev (DSYEV computes all eigenvalues and, optionally, eigenvectors of a real

Table IV.1: Speed Up values are listed for varying system size and processor number (np) for (10x10) CNT structure.

Number of Atom 10x10 Tube	$O(N)$ np=2	$O(N)$ np=3	$O(N)$ np=4	$O(N)$ np=5	$O(N)$ np=6	$O(N)$ np=7	$O(N)$ np=8
200	1.85	2.58	3.46	3.53	2.41	2.22	0.78
360	1.92	2.70	3.29	2.88	1.56	1.19	1.28
400	1.96	2.78	3.58	3.71	2.18	1.24	1.05
520	1.95	2.76	3.53	3.27	2.12	1.47	1.21
600	1.89	2.74	3.55	3.28	2.07	1.60	1.50
720	1.86	2.76	3.56	3.54	1.94	1.73	1.56
800	1.83	2.63	3.57	3.02	2.65	1.73	1.48

symmetric matrix) and dsyevd (DSYEVD computes all eigenvalues and, optionally, eigenvectors of a real symmetric matrix. If eigenvectors are desired, it uses a divide and conquer algorithm). It is seen that for the standard matrix diagonalization ($O(N^3)$ TBMD) dsyevd routine decreases the run time but uses higher amount of RAM source. On the other hand for $O(N)$ TBMD simulation, Dsyevd and Dsyev run time values are similar to each other. This is true even when the system size increases. Since the interactions are local this is an expected behavior.

Our results show that parallelization technique is beneficial because of the nature of the $O(N)$ algorithm. In present situation, parallelization together with $O(N)$ algorithm proves to be very effective and favorable.

Table IV.2: Efficiency with respect to for varying system size and processor number (np)

Number of Atom 10x10 Tube	$O(N)$ np=2	$O(N)$ np=3	$O(N)$ np=4	$O(N)$ np=5	$O(N)$ np=6	$O(N)$ np=7	$O(N)$ np=8
200	0.92	0.86	0.86	0.71	0.40	0.32	0.10
360	0.96	0.90	0.82	0.58	0.26	0.17	0.16
400	0.98	0.93	0.89	0.74	0.36	0.18	0.13
520	0.98	0.92	0.88	0.65	0.35	0.21	0.15
600	0.94	0.91	0.89	0.66	0.34	0.23	0.19
720	0.93	0.92	0.89	0.71	0.32	0.25	0.19
800	0.91	0.88	0.89	0.60	0.44	0.25	0.18

Table IV.3: Comparison of Dsyevd and Dsyev Lapack routines on the cases; total run time for $O(N^3)$ TBMD and diagonalization time $O(N)$ TBMD per MD Step (in sec).

Number of Atom 10x10 Tube	$O(N^3)$ Dsyevd Sequential Run Time	$O(N^3)$ Dsyev Sequential Run Time	$O(N)$ Dsyevd Sequential Diagonalizing	$O(N)$ Dsyev Sequential Diagonalizing
200	73.4	84.9	10.8	9.46
360	461.9	511.6	20.78	17.90
400	573.2	672.7	22.32	22.12
520	1214.7	1516.7	30.88	28.18
600	2303.5	4432.8	35.54	32.70
720	-	-	37.88	34.30
800	-	-	42.68	39.18
920	-	-	54.94	51.12

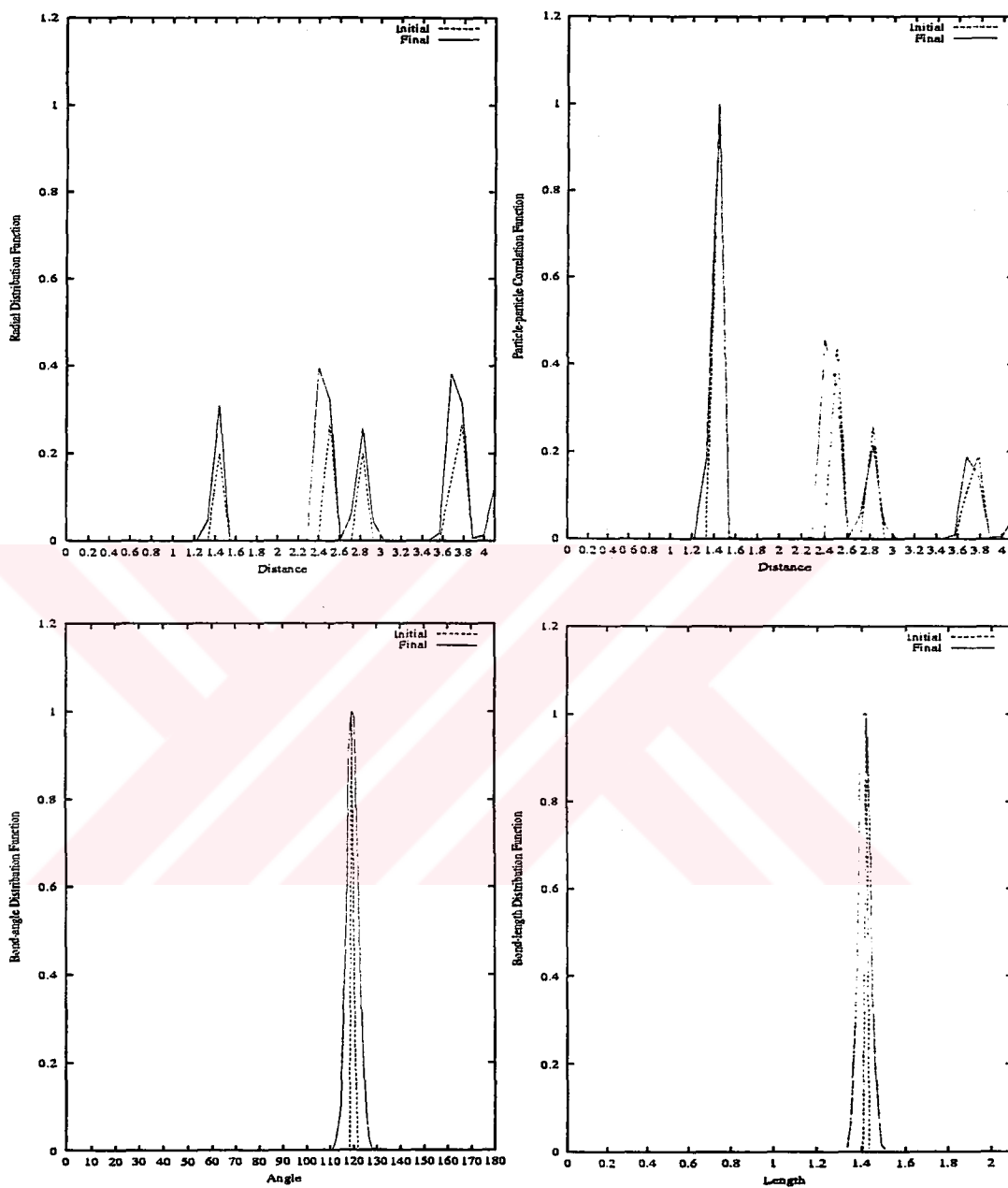


Figure IV.11: Physical Properties; Radial Distribution Function, Pair Correlation Function, Bond-Angle Distribution Function, Bond-Length Distribution Function for the Tube Structure 10x10 and $T= 300$ K with the electronic temperature 0.005 eV (MD Time Step $\equiv 1$ fs); respectively.

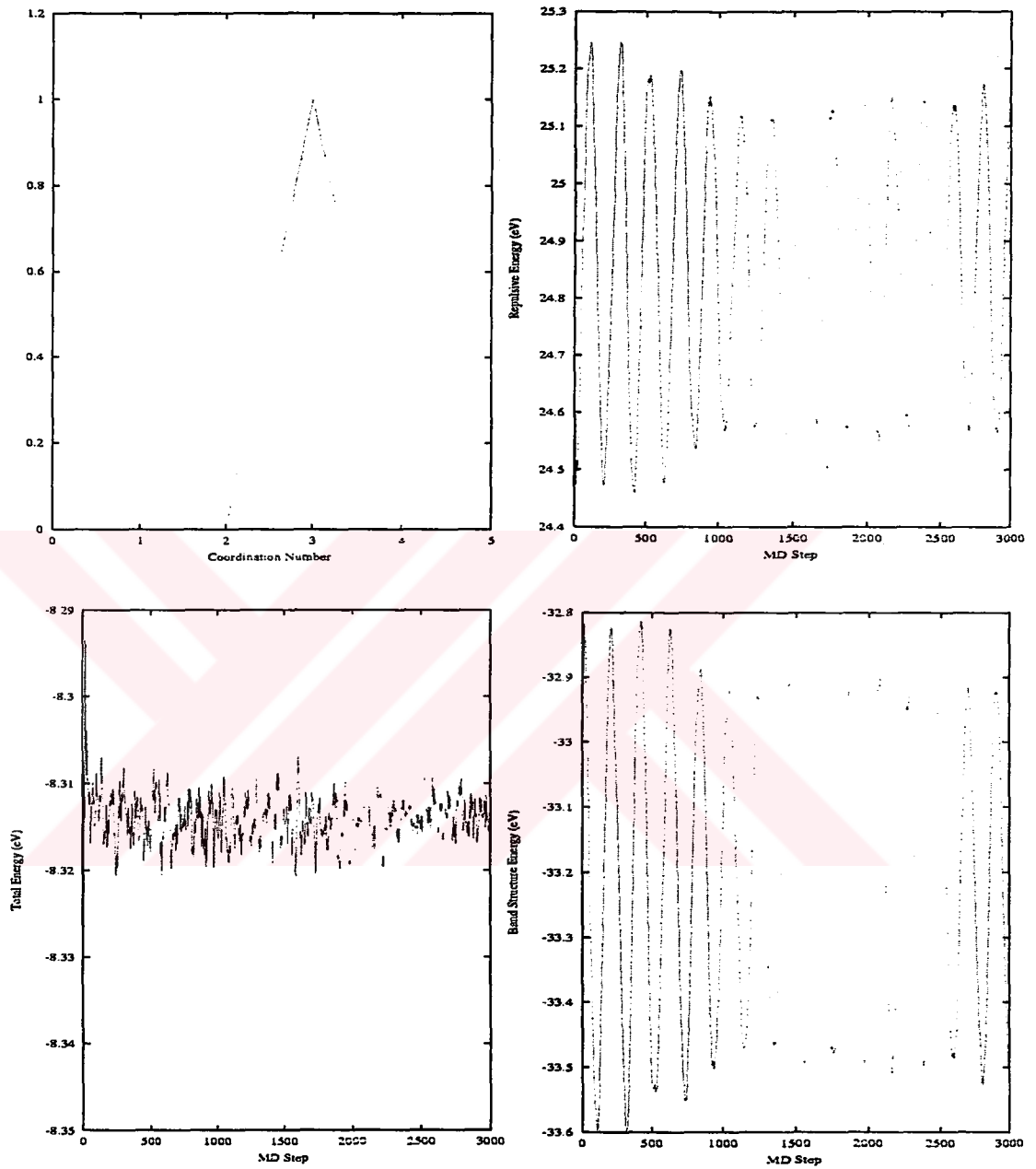


Figure IV.12: Physical Properties; Atomic Coordination Number, Repulsive Energy, Band Structure Energy, and Total Energy for the Tube Structure 10x10 and $T=300$ K with the electronic temperature 0.005 eV (MD Time Step \equiv 1 fs); respectively.

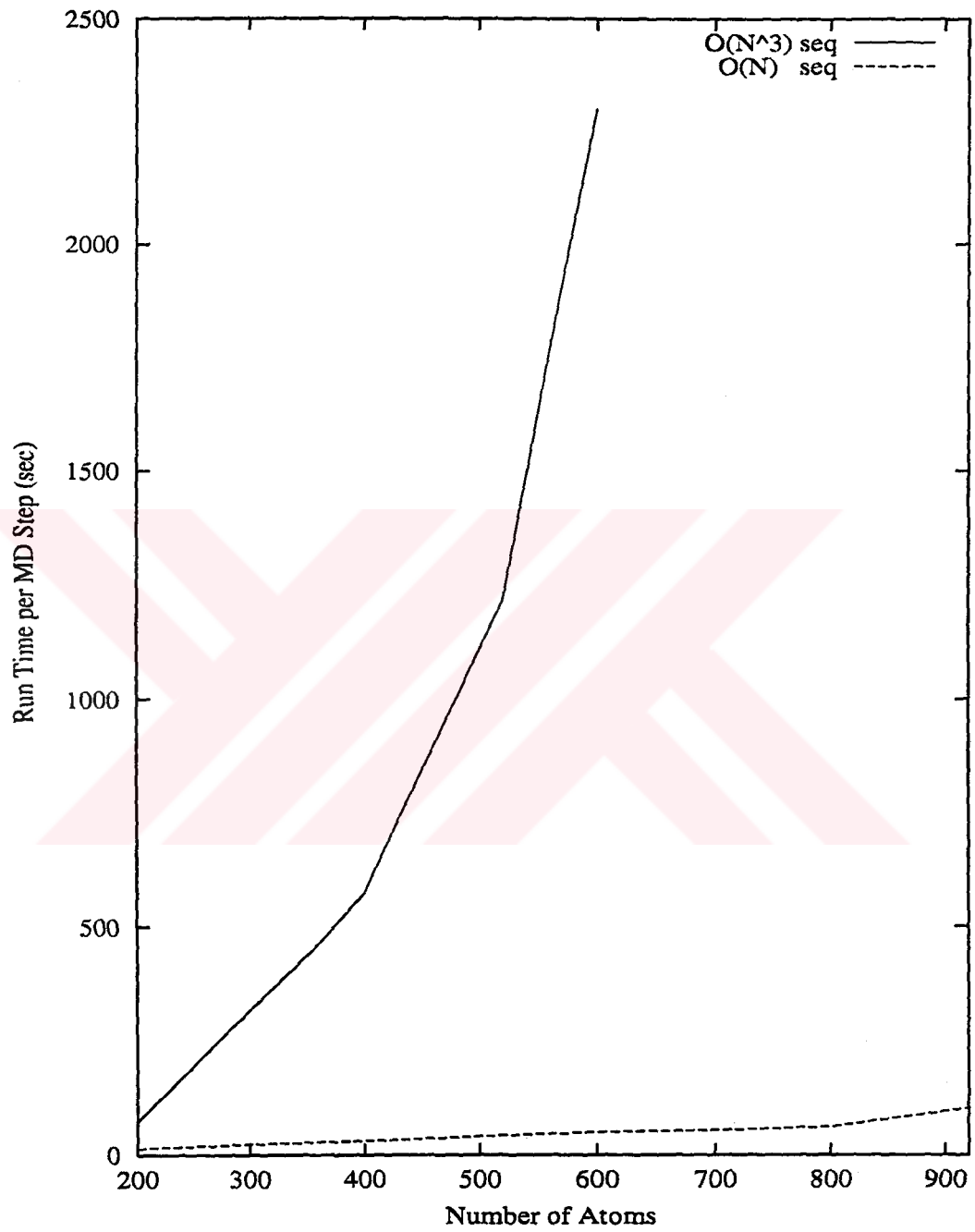


Figure IV.13: Run Time per MD Step (sec) vs Number of Atoms for $O(N^3)$ TBMD and $O(N)$ TBMD

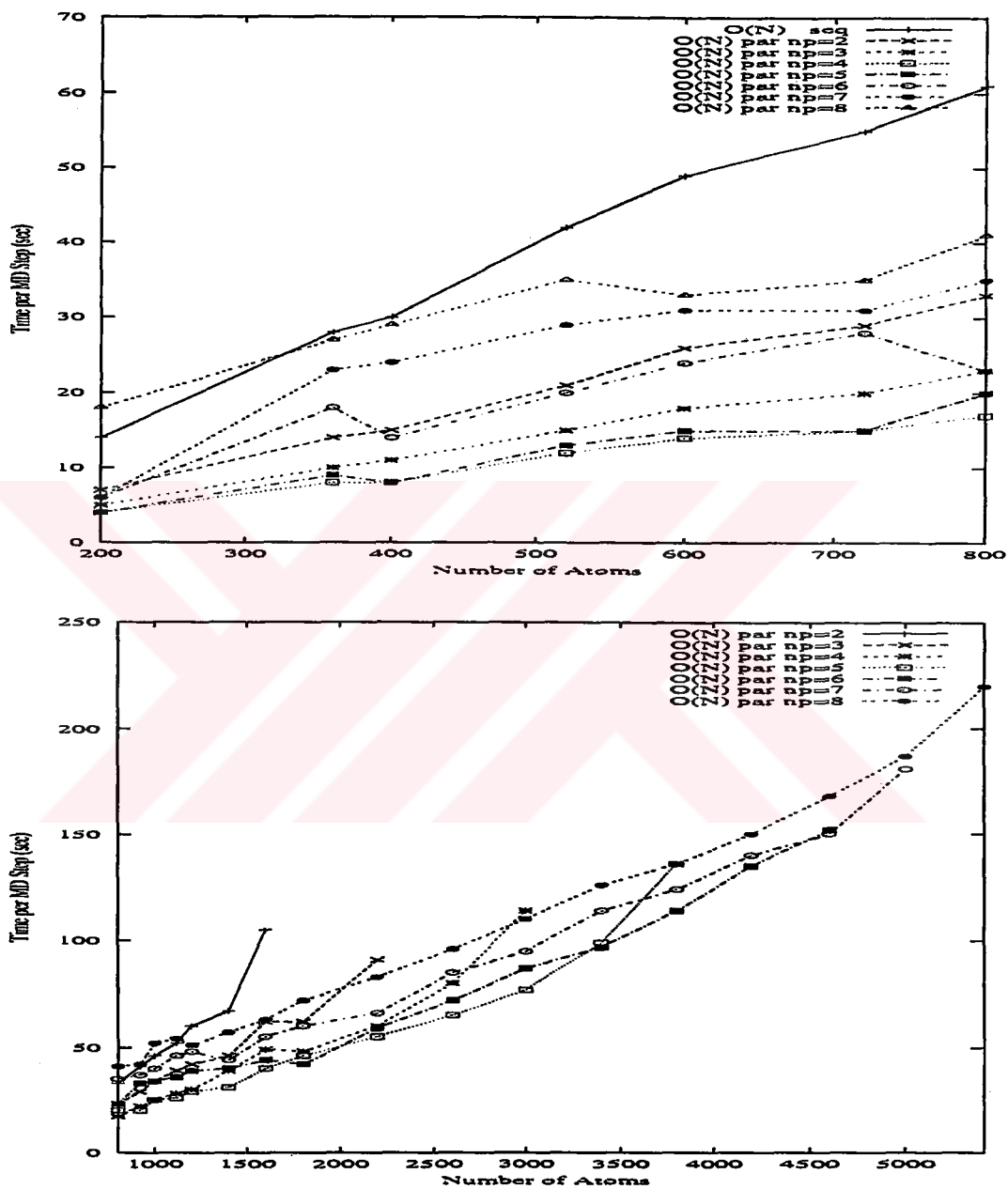


Figure IV.14: Run Time per MD Step (sec) vs Number of Atoms for different number of processors (np)

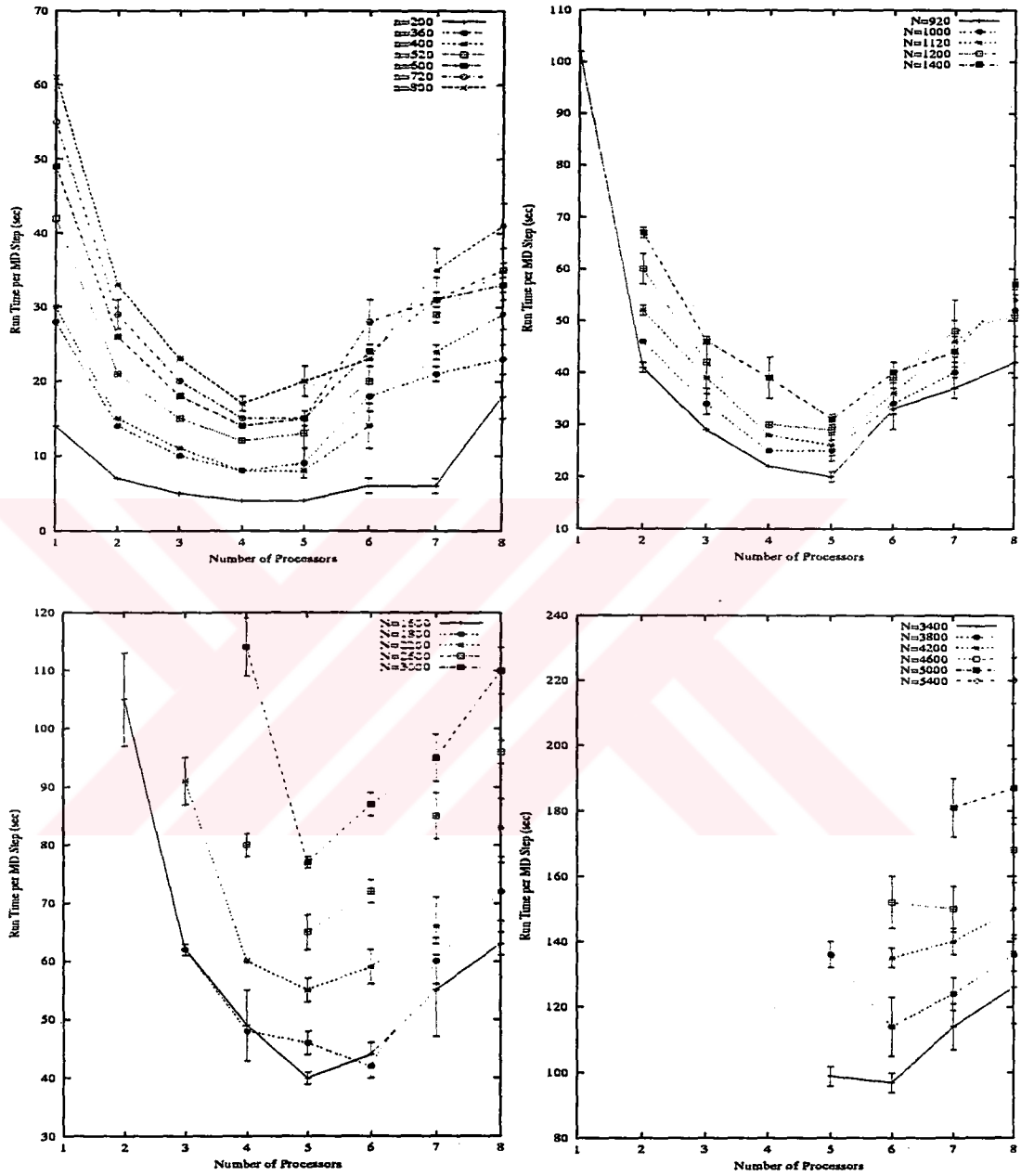


Figure IV.15: Run Time per MD Step (sec) vs Number of Processors for varying size of atoms (N)

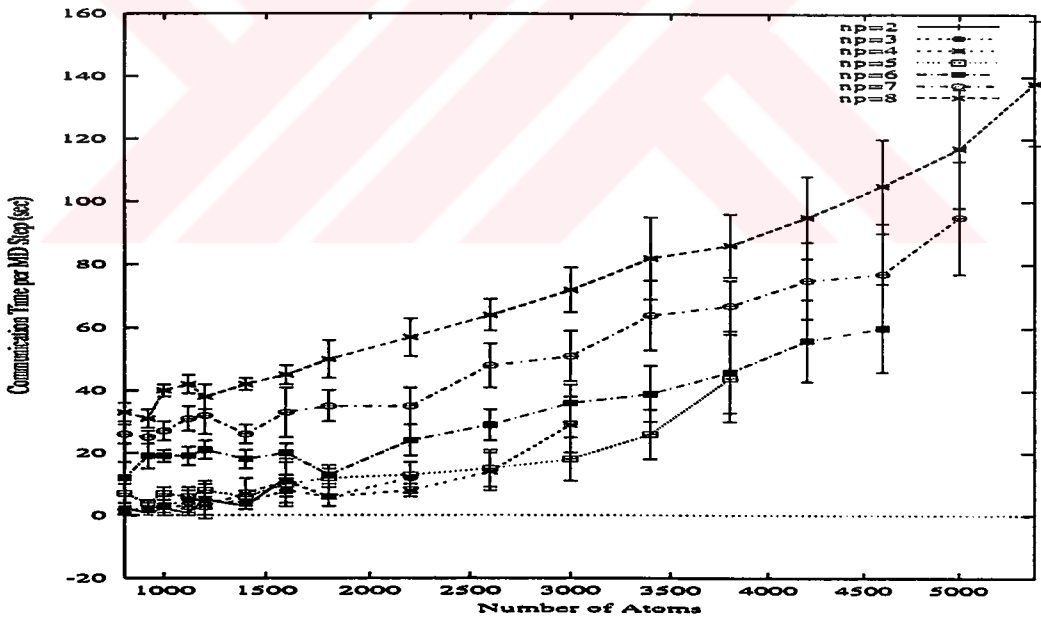
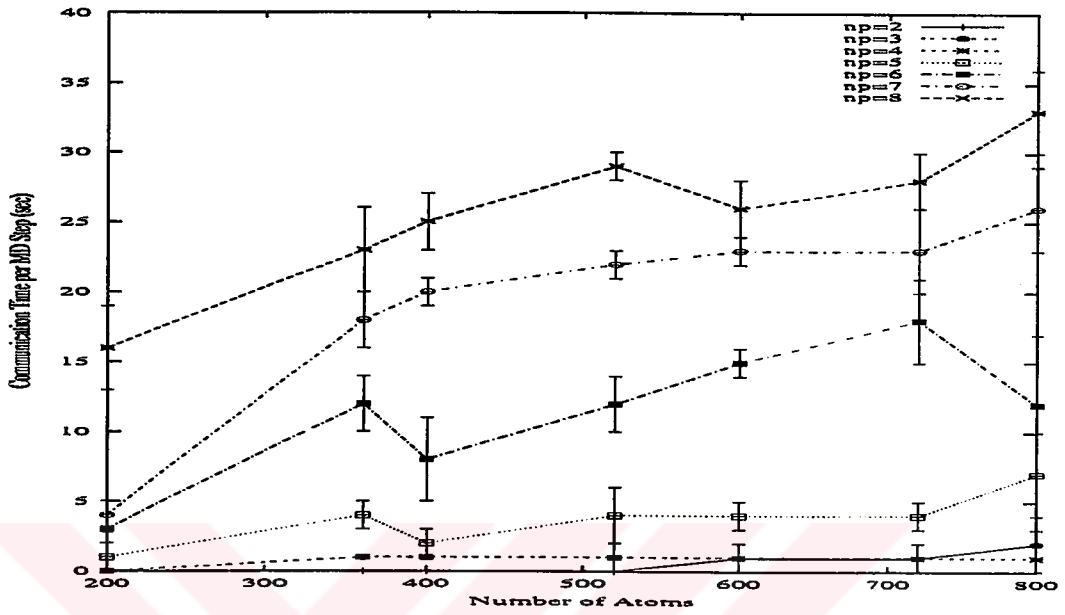


Figure IV.16: Communication Time per MD Step (sec) vs Number of Atoms for different number of processors (np)

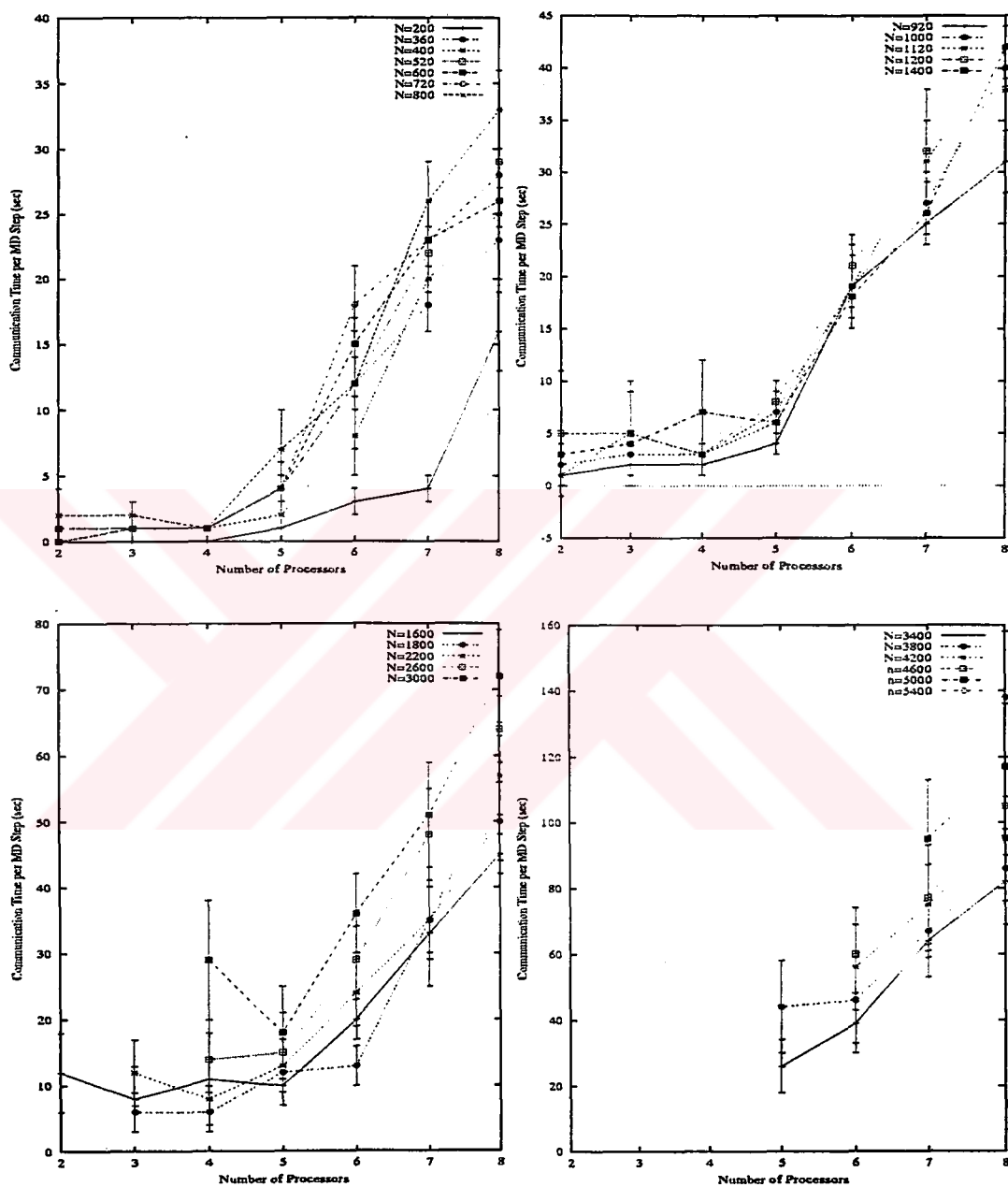


Figure IV.17: Communication Time per MD Step (sec) vs Number of Processors for different number of atoms (N)

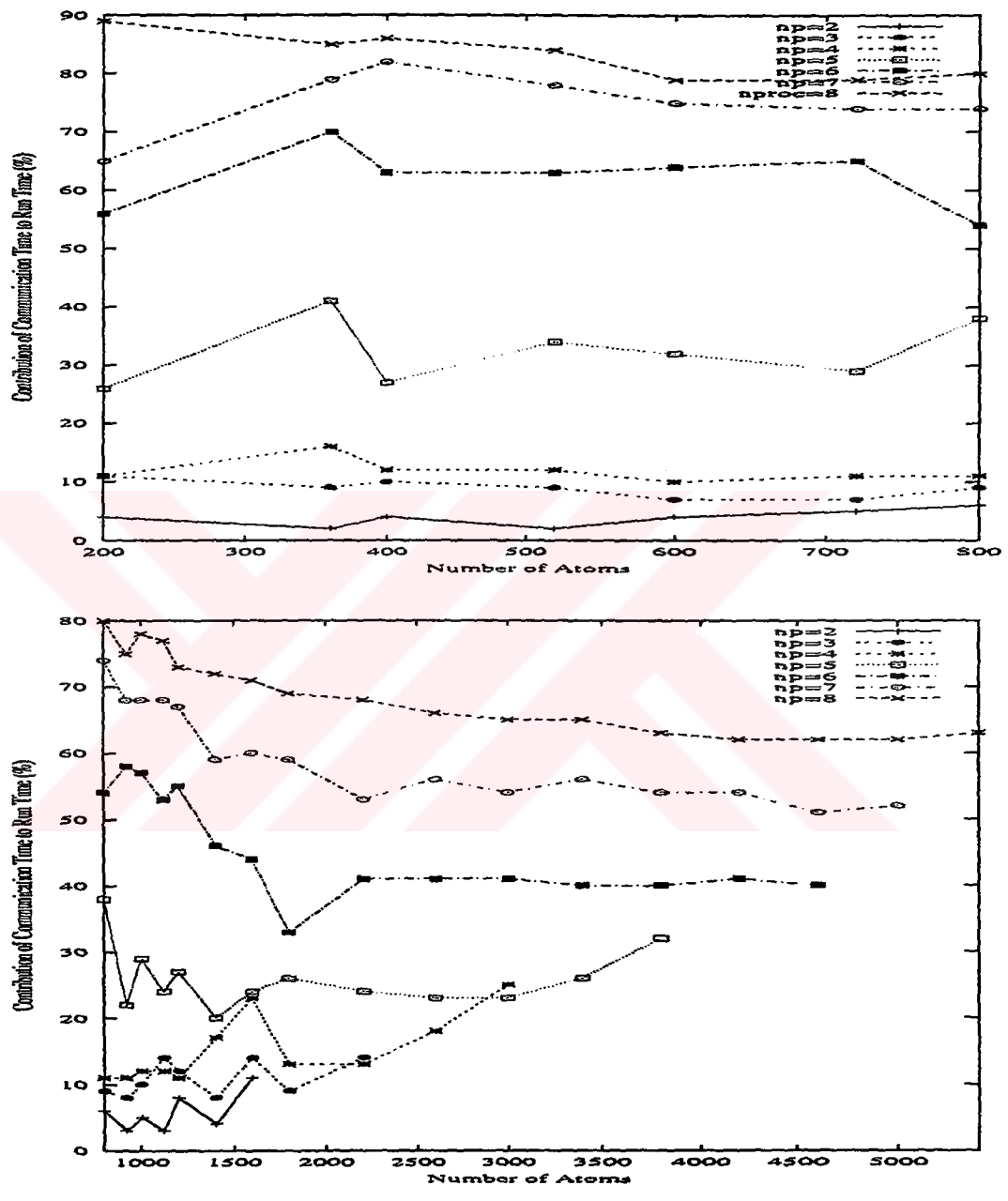


Figure IV.18: Contribution of Communication Time to Run Time (%) per MD Step vs Number of Atoms for different number of processors

IV.3 Structural Stability and Energetics Under Uniaxial Strain

The structural stability, energetics and tensile mechanical properties of 10x10 carbon nanotube are investigated. The uniaxial strain is applied and studied using $O(N)$ TBMD method. Similar to that of graphite, carbon nanotube has high flexibility, strength and stiffness. Although a direct measurement of its mechanical properties is difficult because of its nanosize, along with the developments in instrumentation, production, processing and manipulation techniques, the measurements for the elastic moduli of carbon nanotube became possible. On the other hand, this extreme small size is very suitable for performing atomistic simulations. Both the experimental [44]–[60] and theoretical [61]–[85] studies have shown that SWCNTs, and SWCNT ropes are promising low-weight high-strength fibers for use as reinforcing element in composite materials. It is predicted that Young's Modulus of SWNTs can be up to order of 1 TPa. This is comparable to that of diamond. It is also predicted that SWCNTs can sustain large strain in axial direction [81].

IV.3.1 Method

In this study, 10x10 carbon nanotube (consisting of 400 atoms with 20 layers) is simulated under tensile loading using our developed $O(N)$ parallel TBMD program. Two steps are followed; firstly, the tube is annealed at simulation temperature for 3000 MD Steps (time step used in the simulation is 1 fs). The variation of total energy, and some physical properties such as radial

distribution function, atomic coordination number, bond-angle distribution function, and bond-length distribution function are given in the Figs IV.11 and IV.12. The geometrical structure of pristine carbon nanotube at the end of the simulation is given in the Fig.IV.19. The next step is to apply strain on the tube. Several groups have proposed different procedures; such as shifting the end atoms along the axis (i.e. z-direction) by small steps [72], reducing radial dimension while the nanotube is axially elongated [73], pulling in axial direction with a strain rate and following each step of pulling some additional MD steps were used to relax the distorted structure [75] and using hydrostatic pressure exerted on the walls of SWCNT by the means of encapsulating H_2 molecules inside the tube and the the wall of the tube [74]. In our study, the tensile strain is applied by the reduction or enlargement of the radial dimension while the nanotube is axially elongated or contracted. Throughout this procedure volume of the tube is kept constant. Zhou et al. [73], has investigated the mechanical properties of SWCNT with the same procedure using a first-principle cluster method within the framework of local density approximation. We further simulated the deformed tube structure (under uniaxial strain) for another 2000 MD steps (time step is chosen again as 1 fs) to understand the strain mechanism. Strain is obtained from $(\epsilon = \left(\frac{L-L_0}{L_0}\right))$, where L_0 and L are the tube lengths before and after the strain, respectively). Several strain rates are applied to pristine tube to study the strain rate. Simulations are performed at room temperature and periodic boundary condition is applied along the axial direction.

IV.3.2 Results

Total energy of curve of the carbon nanotube as a function of strain along the tubular axis is given in Figure IV.20. We observe an asymmetric pattern for the elongation and compression cases. The tube has not a high strength for the compression as much as elongation. This might be due to the dominant behavior of repulsive forces in the system under uniaxial strain. This figure indicates that the remarkable elastic properties under large strain are caused by nonparabolic strain energy. It is seen that the carbon nanotube is able to carry the strain up 122% of pristine tube length in elongation and up to 93% of pristine tube length for the compression.

The variation of total energy of the deformed system during MD simulation for the strains 0.22 elongation and 0.07 compression are given in the Figure IV.21. In the graphs, first 3000 MD steps is for the equilibration of the carbon nanotube and the next 2000 MD steps shows the variation of the total energy of the tube during the simulation under the applied uniaxial strain. It is seen that the tube under these strain rates is able to sustain its structural stability. The geometrical structures for these strain rates at the end of the simulations are given in the Figs. IV.22 and IV.23 for the elongation and contraction, respectively. Bond angles and bond lengths are the two important factors that control the deformation. The effect of the strain on the bonds is such that it alters the angles between two neighbor carbon bonds and changes the lengths of the C-C bonds. For high strain rates the changes in the the radial distribution function, bond-length distribution and bond-angle distribution

are given in Figs. IV.24–IV.26. It is seen in the graphs that the two–third of the bond lengths and one–third of the bond angles increases (decreases) when tube is elongated (contracted) as expected.

Increasing the strain beyond these points results in the disintegrations in the carbon nanotube. The geometrical structures, and the behavior of the total energy for the strains 0.23 (elongation) and 0.08 (compression) are given at the Figs. IV.27 and IV.28. Figures show that the elongated tube dissociates by starting from the middle like a zipper while the compressed tube starts to dissociate from the ends of the tube. Each peaks in the Figs. IV.29a and IV.29b represent disintegrations of the atoms from the tube.

The elastic constants are calculated from the second derivative of the energy density with respect to various strain. To obtain the stress–strain curve, the cross–section upon which the resulting forces act is needed to be estimated. The cross–sectional area of a nanotube is ambiguous in definition [42]. A circular cylindrical shell is considered around the surface of the nanotube. Then the surface area of the cross–section, s , is defined as

$$s = 2\pi R\delta R \quad (\text{IV.17})$$

where R stands for the radius of the SWNT, δR for the wall–thickness. It should be noted that different wall–thickness values were used by several groups [67], [65], [68], [66]. In Ref. [67], $\delta R=3.4 \text{ \AA}$ (measured interwall distance in the Multi Wall Nano Tube) was used, while in Ref. [68] $\delta R=1.7 \text{ \AA}$ (taken as the van der Waals radius for Carbon) was accepted, it is also accepted as 0.66 \AA (in the π orbital extension) in Ref. [65] and as the whole cross-sectional

area of the tube in the Ref. [66]. We defined the thickness of SWNT shell as follow in our research; $\delta R = 3.4 \text{ \AA}$. The stress–strain curve obtained from this study is given in the Figure IV.30a. It is seen in the figure that the elastic limit is at the strain value of 0.09. Beyond the elastic limit, the stress–strain curve departs from a straight line. Hence, its shape is permanently changed. The breaking point is observed at the strain rate of 0.23. The Young’s modulus is determined as the slope of the stress-strain curve. Our calculated value of the Young’s modulus of the 10x10 Carbon nanotube is 0.311 TPa.

Theoretical tensile strength is defined as the maximum stress, which may be applied to the material without perturbing its stability. It can be given as

$$\sigma_{th} = \frac{1}{s} \left(\frac{\partial E_{tot}}{\partial \varepsilon} \right)_{\varepsilon=\varepsilon_i} \quad (\text{IV.18})$$

where ε is the stress, ε_i is the maximum stress in the system, and s is the surface area of cross–section. Our calculated value is 4.92 GPa, which is larger than that of Carbon fibers (2.6 GPa) [86], but less than the in–plane tensile strength of graphite (20 GPa) [87].

Another mechanical property of interest is the Poisson ratio, ν , which is defined by

$$\nu = - \left(\frac{1}{\varepsilon} \frac{R - R_{eq}}{R_{eq}} \right) \quad (\text{IV.19})$$

where R is the radius of the tube at the strain ε , and R_{eq} is the equilibrium (zero strain) tube radius. The Poisson ratio measures how much the tube contracts (expands) radially when subject to a positive (negative) axis strain ε . The corresponding value found in this study is 0.287.

Another interesting phenomenon we observed in simulation is the vibration of SWNT in radial direction. In Figure IV.30b, the average radius of the pristine 10x10 SWNT as a function of MD steps is given. The frequency of vibration can be evaluated from the figure and has the value of 4.71×10^3 GHz. The variation of radius for the strains 0.22 and -0.07 is also given in the Figs. IV.31a and IV.31b. It is found that the strain is effective on the vibration frequency. Increasing strain on the tube structure results in the decrease for the frequency of vibration. It is ranged from 2.94×10^3 GHz to 4.41×10^3 GHz with decrease by the increasing strain rate and has a mean value of 3.70×10^3 GHz.

IV.3.3 Discussion

The elastic properties of 10x10 carbon nanotube under tensile loading is investigated by using O(N) Tight-Binding Molecular Dynamics method. The Young's modulus, tensile strength, Poisson ratio and frequency of vibration are calculated and the values are 0.311 TPa, 4.92 GPa, 0.287 and 4.71×10^3 GHz, respectively. Several groups are reported a wide range of values for the corresponding properties by using several theoretical and experimental techniques.

The Young's modulus values given by different researchers range from 0.200 TPa to 5.5 TPa [74]. The reasons may be attributed for the variation are at the followings:

- The different values are used for the wall-thickness [65]-[68].

- Different procedures are applied to represent the strain [72]-[75].
- The curvature effect of nanotubes was neglected [67], or not [69]. In Ref. [67], it is concluded that the elastic moduli of nanotubes, (SWNT and MWNT) were insensitive to geometrical structure while it is suggested in Ref. [69] that Young's modulus slightly depend on the tube diameter. On the other hand, the variation of Young's modulus as a function of tube radius is also reported [62, 66].
- Accuracy of methods; first-principle methods are more reliable [68]-[74] with comparison to the empirical potentials [61]- [67].
- The strain rates that Young's modulus was calculated are either different [74] or not pointed out [67, 72].
- Difference in the tube lengths; although the Periodic Boundary Condition is applied for the most cases, finite size effects might be still important.

Our result is in the range mentioned above. It emphasizes the high Young's modulus and high strengths of Carbon nanotube. The strain at tensile failure for SWNTs was predicted to be as high as 0.40 [65]. This is a tensile strength of 400 GPa would be expected for SWNTs if one used the in-plane Young's modulus of graphite, ~ 1 TPa [5]. However, such a high tensile strength has not been justified by experiments. In this study, it is found that the elastic limit is at the strain rate 0.09 beyond this point tube becomes permanently changed. In Ref. [74], it is reported that when the strain larger than 0.10, the tube becomes softened. They also estimated the strain at failure for the

SWNT as 0.17 whereas it is found as 0.23 in this study. The procedure for describing the strain in their work is to apply hydrostatic stress to the tube wall. On the other hand, Tight-Binding electronic calculations reported by Ozaki *et al.* [72] revealed large strain as 0.30.

The calculated and measured tensile strength also varies in value. In Ref. [73], it is reported as 6.249 GPa by a result of a first-principle study while it has the value of 62.9 GPa for the perfect 5x5 SWNT under hydrostatic pressure [74]. Another MD simulation by using the multi-body potential function of embedded atom method reports the tensile strength as 9.6 GPa [61]. On the other hand, it is reported as 3.6 GPa [44] and as ranged from 13 to 52 GPa [49] in the experimental studies. The value found in this study is 4.92 GPa and seems to comparable with the experimental and theoretical results.

The calculated Poisson ratio is 0.287 and in good agreement with the available reported values which are 0.278 [67], and 0.32 [73]. The evaluated frequency of vibration for the pristine (10x10) Carbon nanotube is 4.71×10^3 GHz which is very close to the value obtained from the experiment 4.94×10^3 GHz [88] and almost same with the value reported in the MD simulation by using a bond-order potential [75]. In Ref. [75], it is reported that the frequency of vibration is insensitive to the strain rate and the frequency of vibration is identified as self-vibration. We have found that it is not constant and increasing strain rate decreases the vibration frequency.

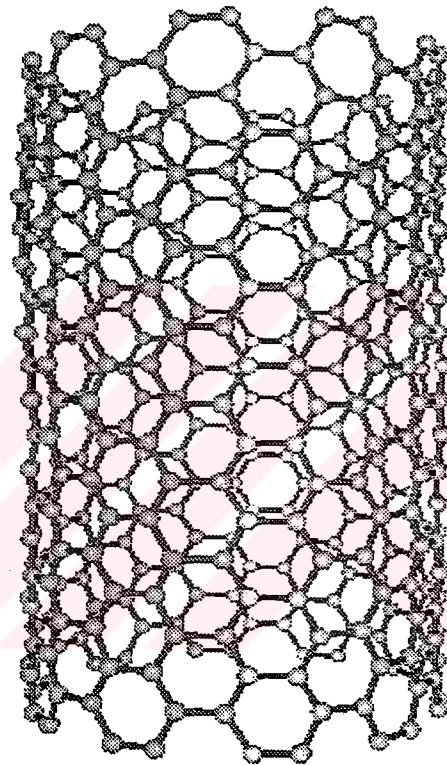


Figure IV.19: The geometrical structure of 10x10 pristine Carbon nanotube after simulation.

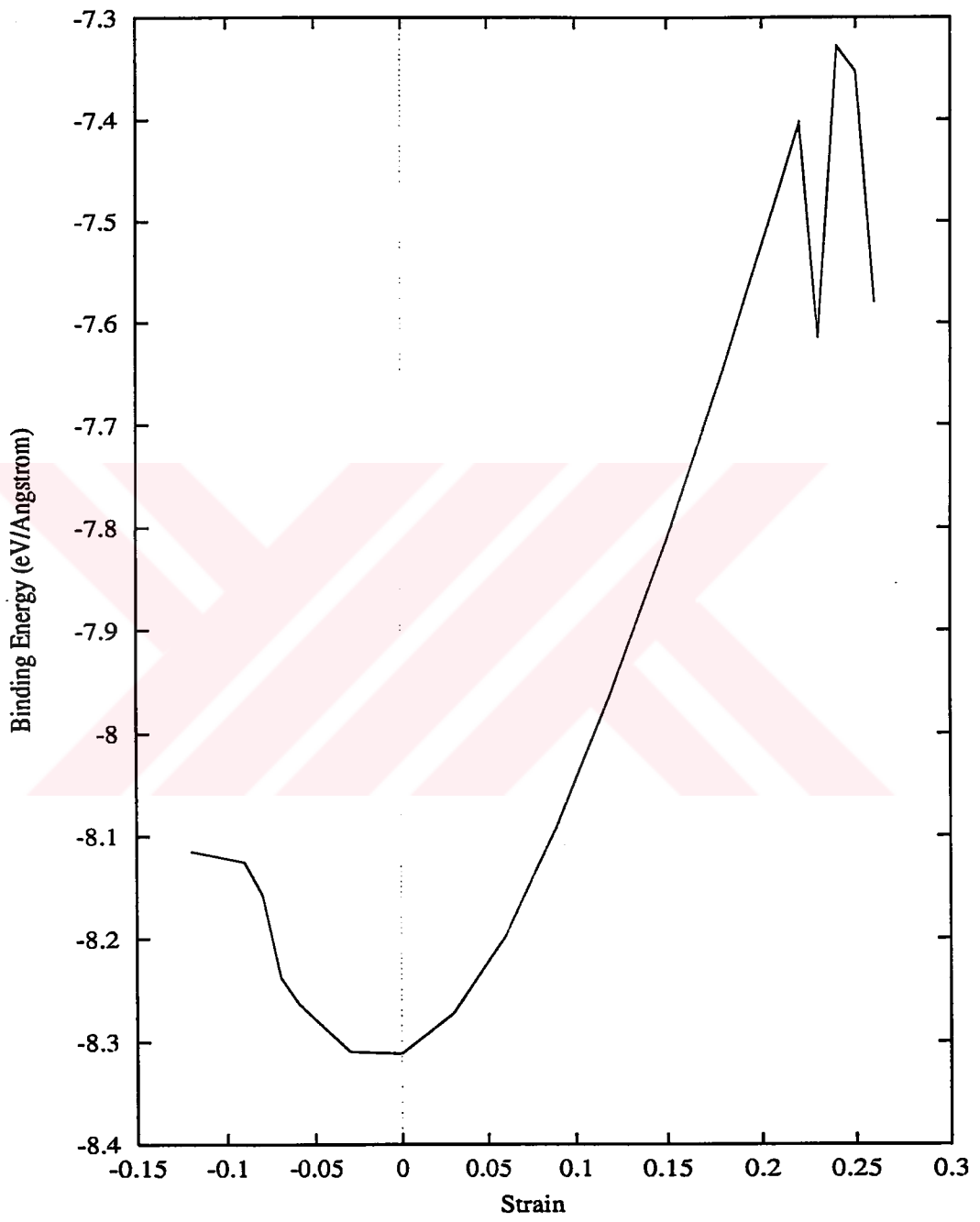


Figure IV.20: Total energy curve as a function of strain ϵ

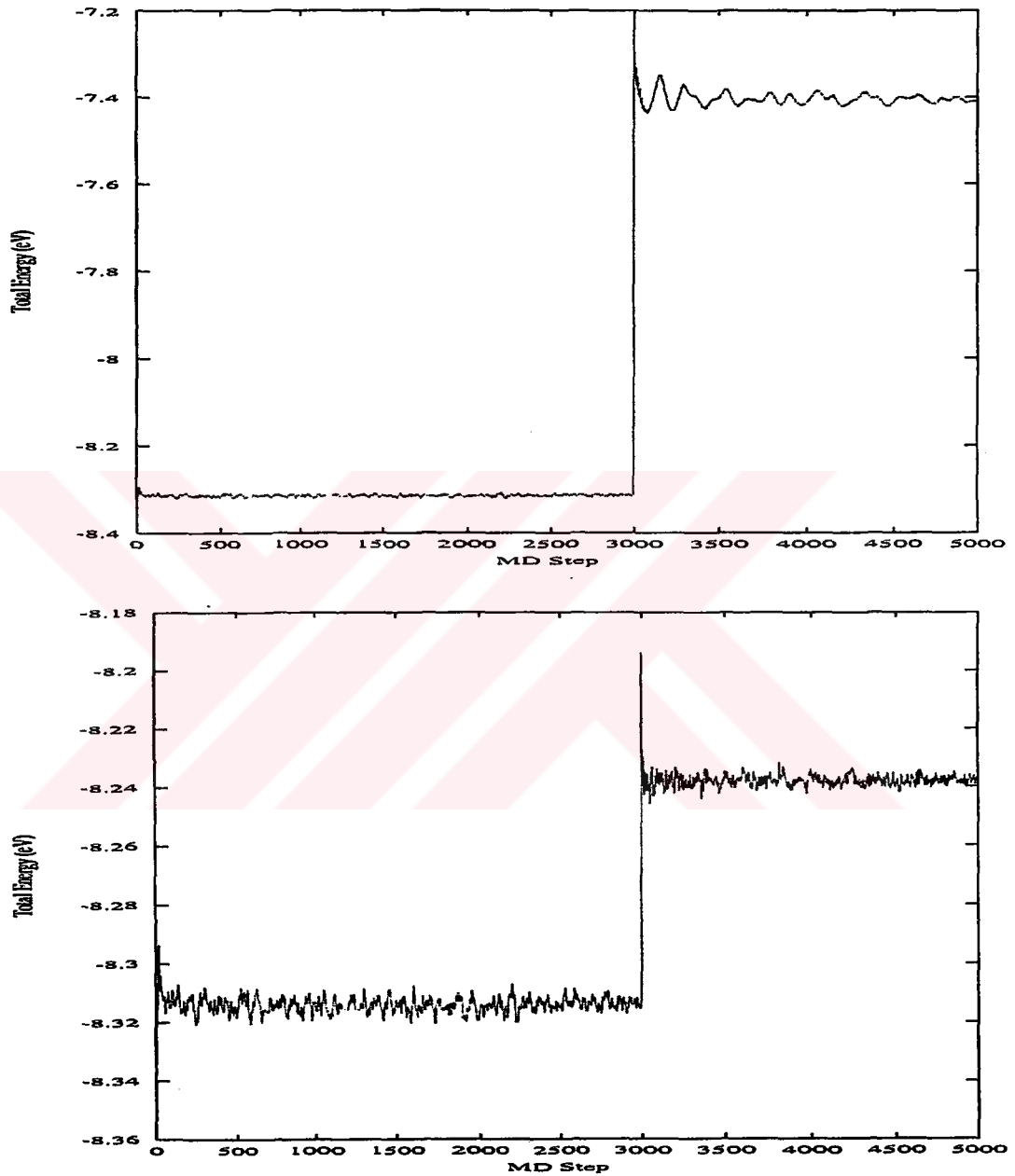


Figure IV.21: The variation of total energy of deformed 10x10 Carbon nanotube during MD simulation for the strains 0.22 and -0.07 (negative sign corresponds for the compression), respectively.

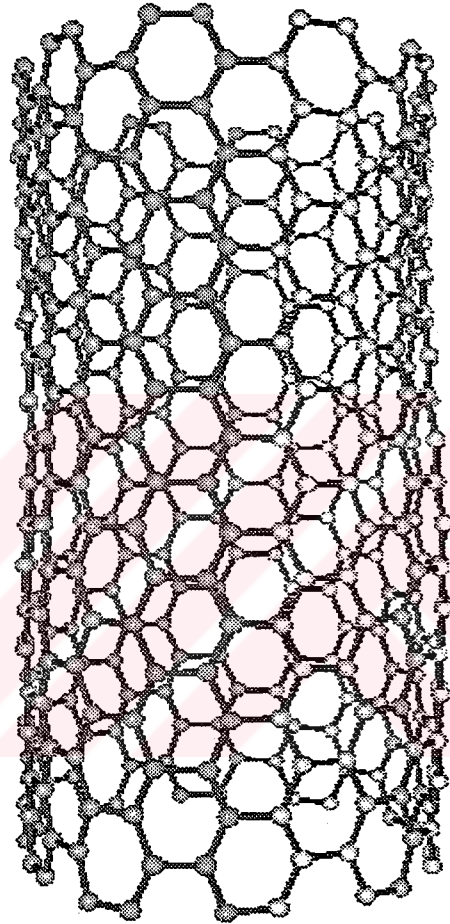


Figure IV.22: The geometrical structure of 10x10 Carbon Nanotube with 0.22 strain (elongation)after simulation.

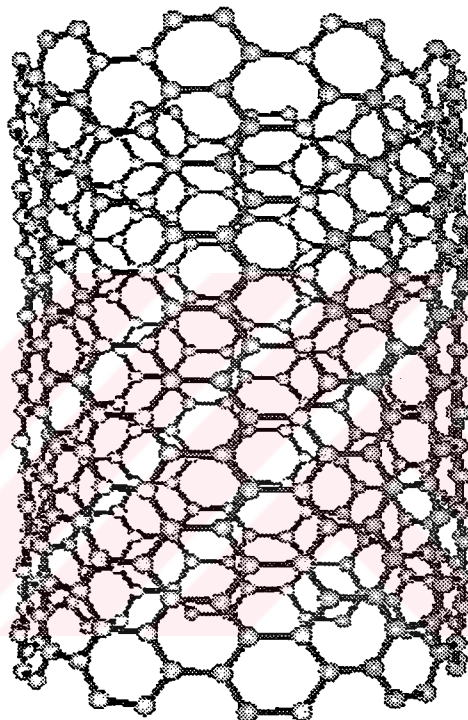


Figure IV.23: The geometrical structure of 10x10 Carbon Nanotube with 0.07 strain (contraction)after simulation.

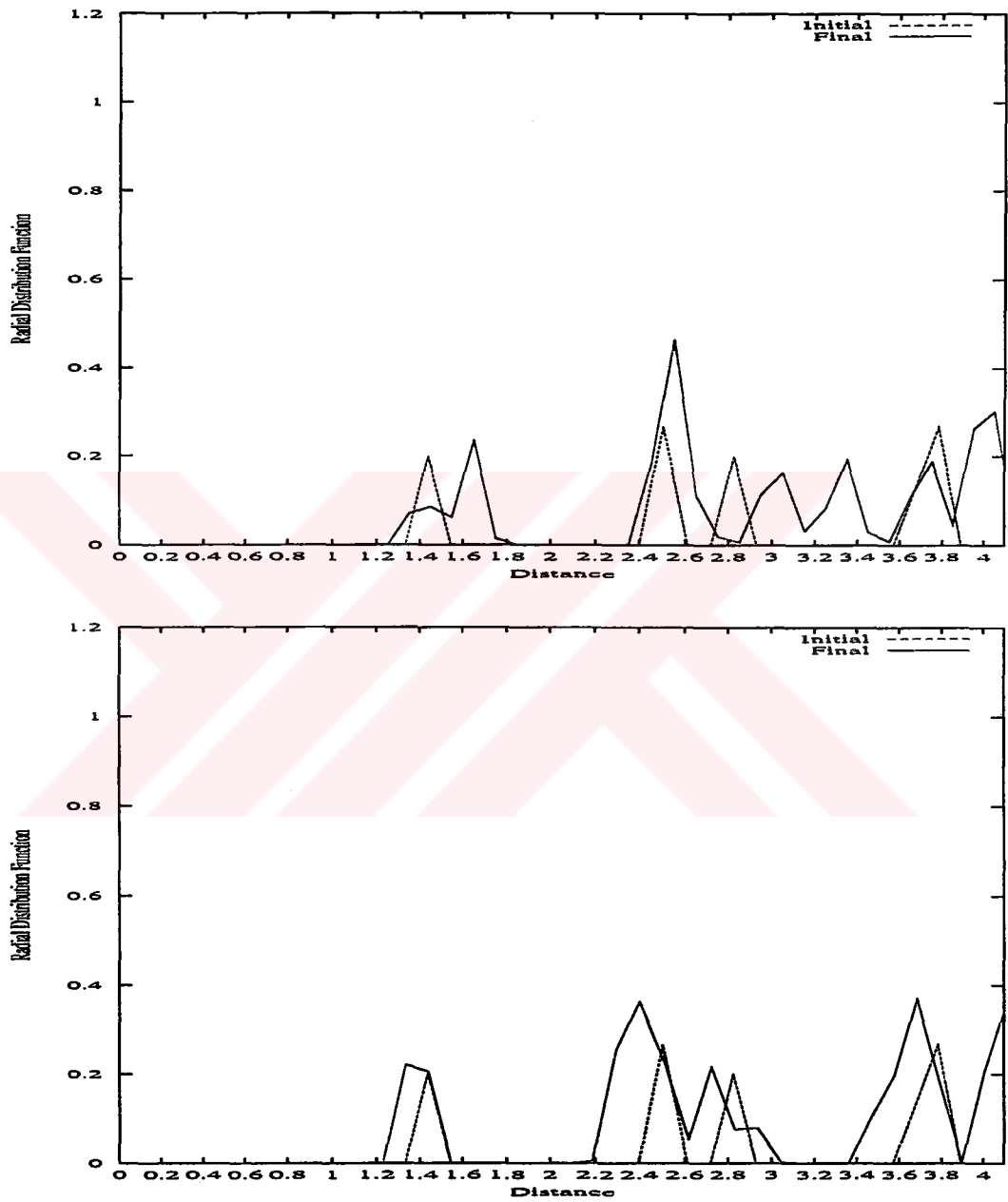


Figure IV.24: Radial Distribution Functions for the Tube Structure 10x10 under strains 0.22 and -0.07, respectively.

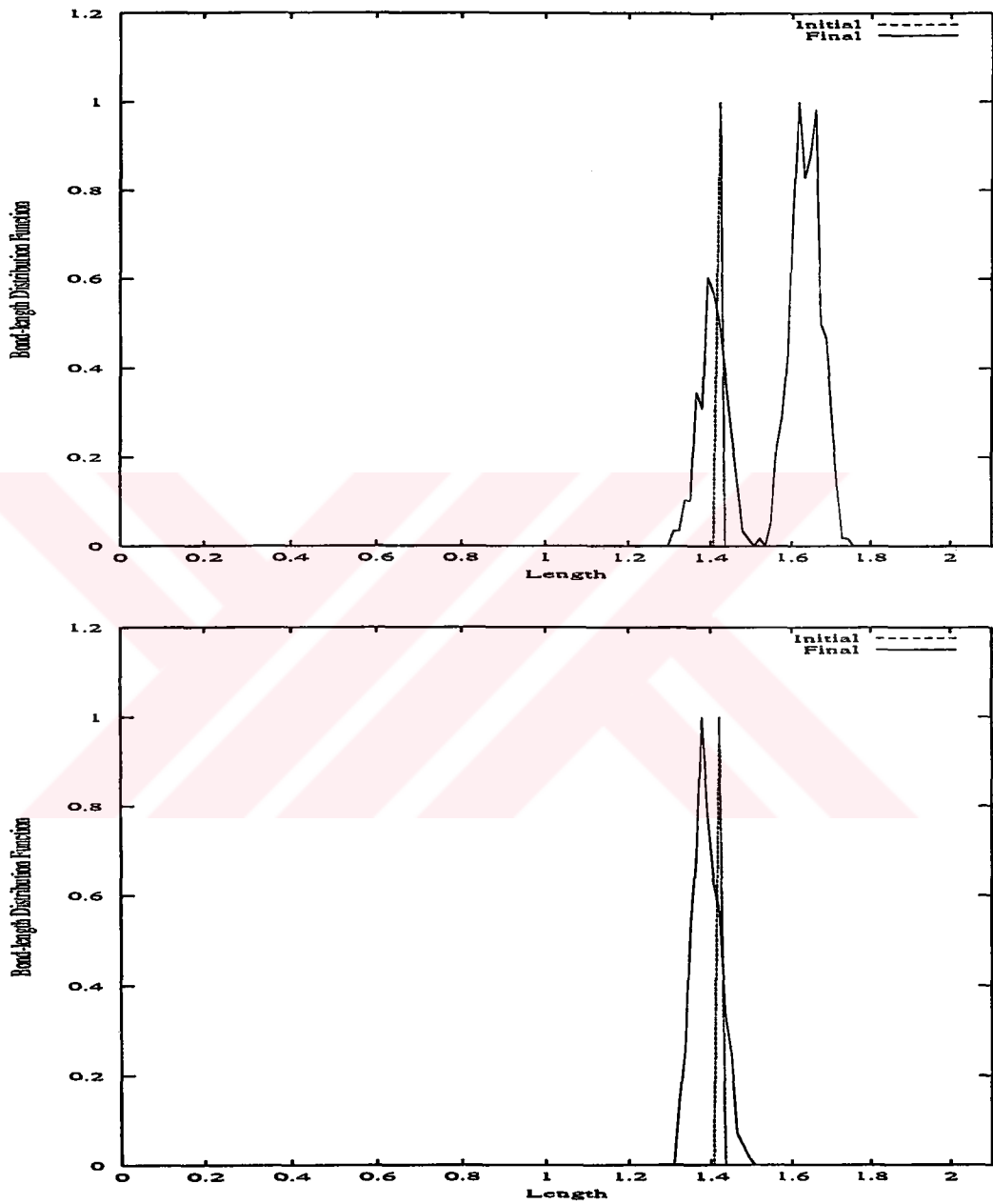


Figure IV.25: Bond-length Distribution Functions for the Tube Structure 10x10 under strains 0.22 and -0.07, respectively.

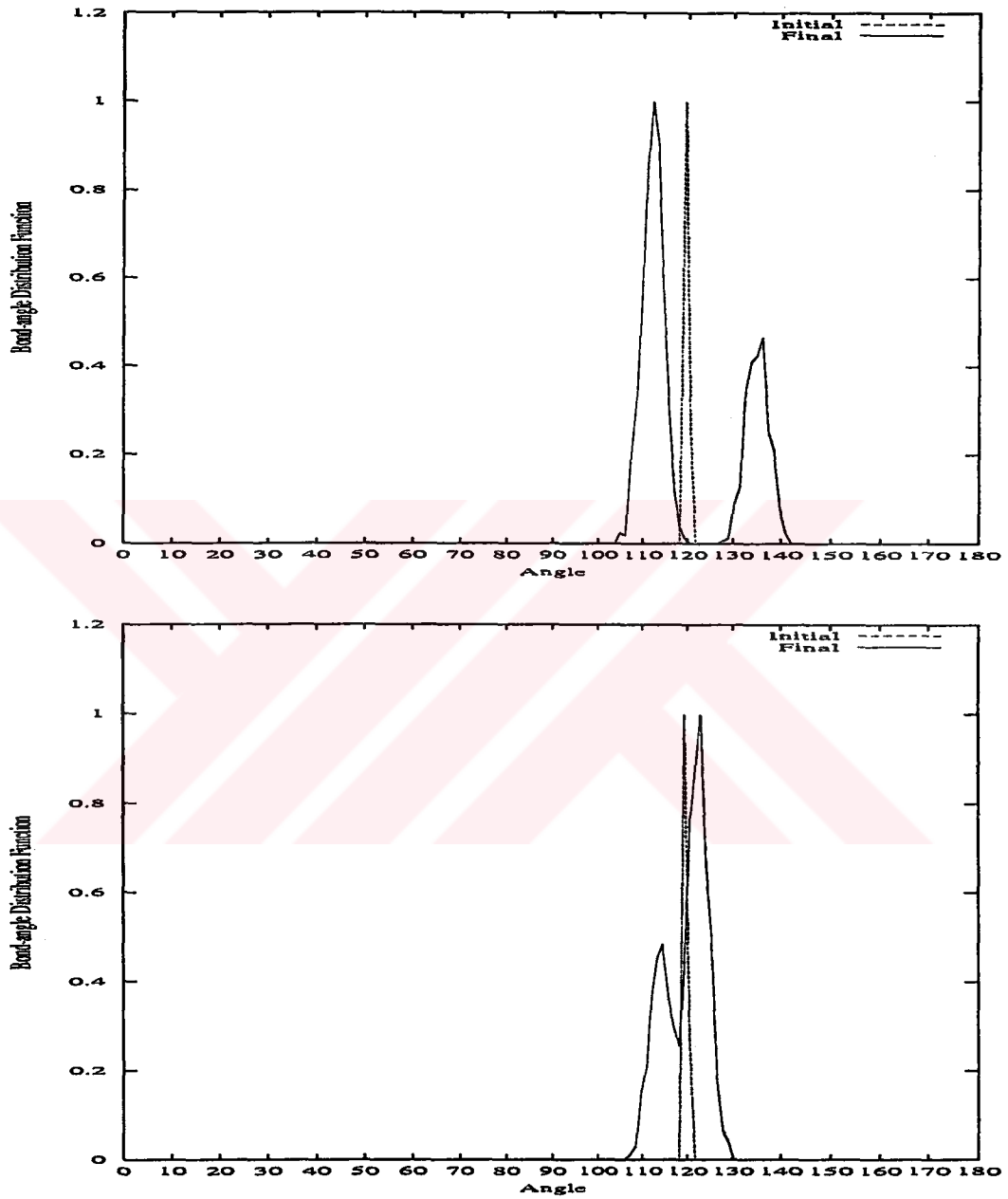


Figure IV.26: Bond-angle Distribution Functions for the Tube Structure 10x10 under strains 0.22 and -0.07, respectively.

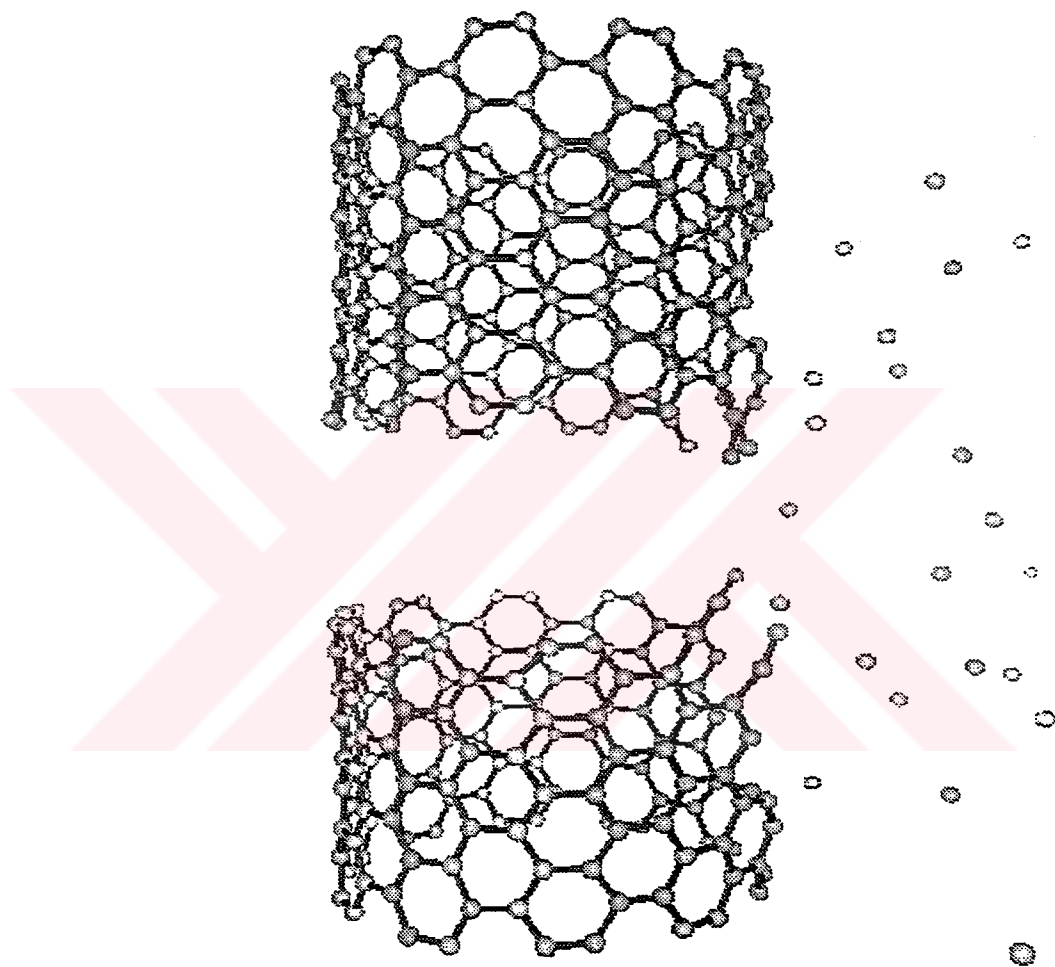


Figure IV.27: The geometrical structure of 10x10 Carbon Nanotube with 0.23 strain (elongation)after simulation.

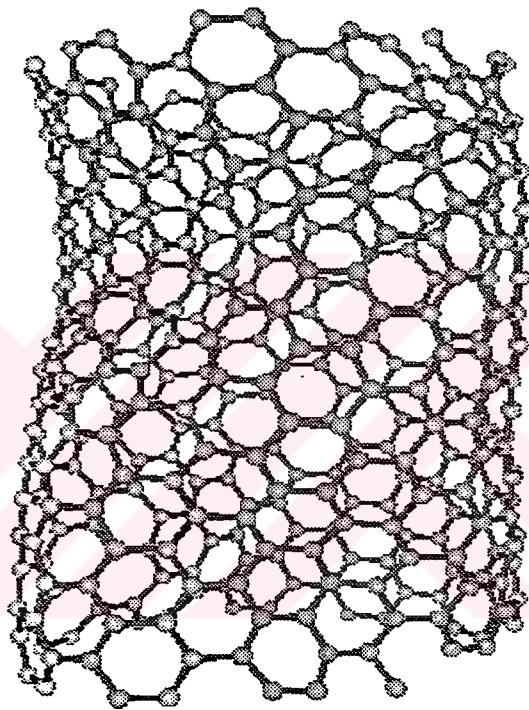


Figure IV.28: The geometrical structure of 10x10 Carbon Nanotube with 0.08 strain (contraction)after simulation.

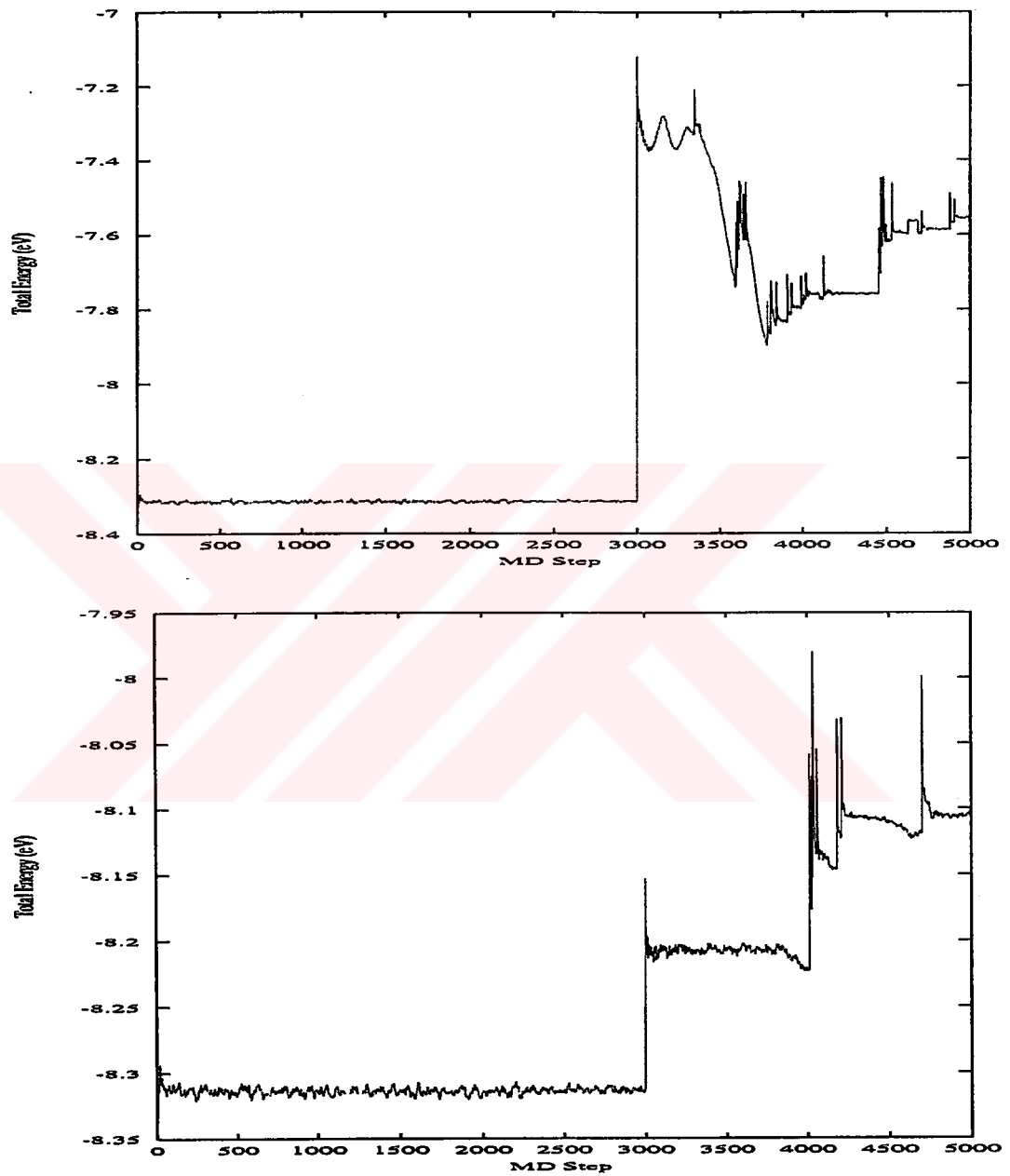


Figure IV.29: The variation of total energy of deformed 10x10 Carbon nanotube during MD simulation for the strains 0.23 and -0.08, respectively.

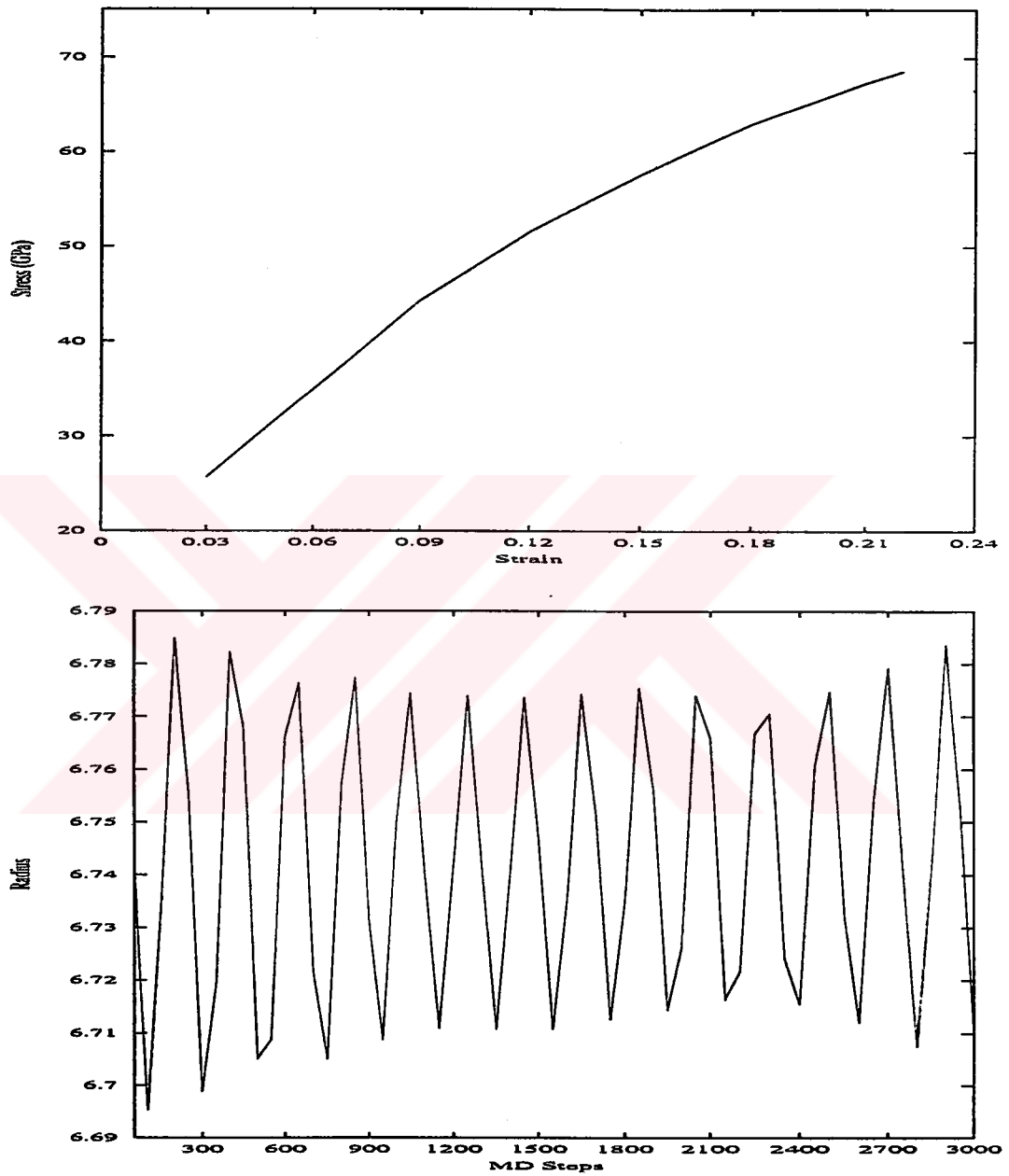


Figure IV.30: The uniaxial stress applied to the tube versus the strain ϵ (elongation) and the variation of radius of pristine (10x10) Carbon nanotube as a function of MD steps; respectively.

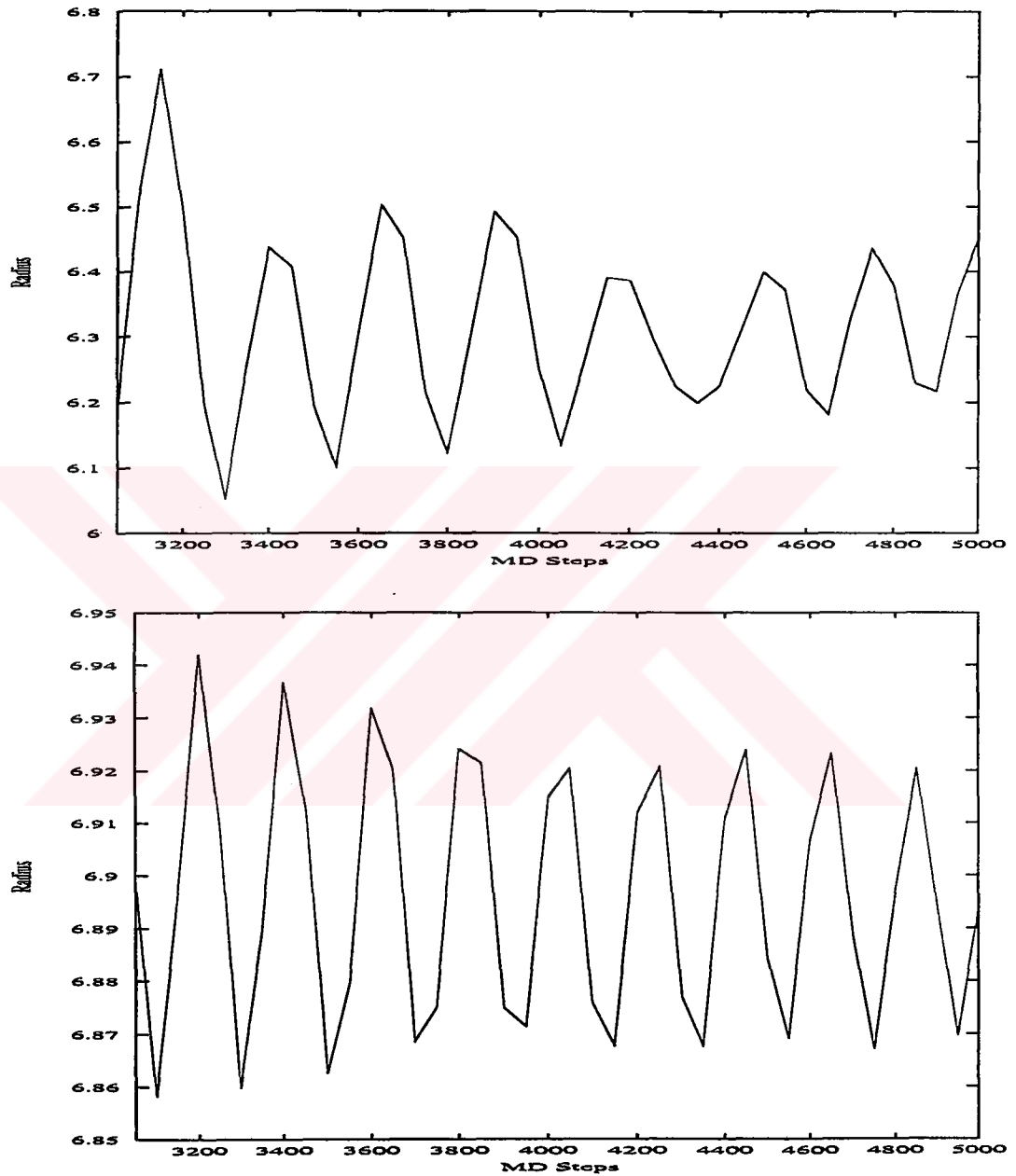


Figure IV.31: The variation of radius of (10x10) Carbon nanotube as a function of MD steps with strain rates 22% and -7%; respectively.

CHAPTER V

CONCLUSION

Carbon is unique among the elements in its ability to create a wide-variety of network-like structures termed fullerene. From the present research status CNT materials have been expected to carry out the wide-spreading industrial applications in the near future. With the development of new applications, two main characteristics of the nanotubes are used. First, there are the electronic properties. Being metallic or semi-conducting, depending on their structure, nanotubes can be used in the development of quantum wires with interesting electronic transport properties, giving rise to a whole new concept of nanodevices. Also mechanical devices are developed, using mostly chemically modified nanotubes. The mechanical and elastic properties are being used in the development of novel materials.

The chirality of SWCNT is denoted by two numbers (n, m) which describe how graphite sheets roll up to form CNTs. The SWCNT with $n \neq 0$ but $m = 0$ is named zigzag CNT, $n = m$ named armchair CNT, and the others are named chiral CNT. The electronic properties of SWCNT are strongly dependent on its chirality. The researches show that if $n - m$ is a multiple of three, then CNTs

present metallic conductivity, otherwise present semiconductor conductivity.

In the thesis, the mechanical properties of SWCNT are investigated using our developed $O(N)$ parallel Tight-Binding (TB) Molecular Dynamics (TBMD) method [89]. The TB theory has been established as a good compromise between ab initio simulations and model-potential ones, bridging the gap between them, either as far as the overall numerical efficiency or as far as accuracy are concerned. TBMD is a computational tool designed to run finite-temperature MD simulations within the semi-empirical tight-binding scheme. The electronic structure of the simulated system is calculated by a TB Hamiltonian so that the quantum mechanical many-body nature of interatomic forces is naturally taken into account.

The main problem in the traditional TB is the increasing system size. When the system size increases (N), the time to diagonalize the constructed Hamiltonian matrix becomes the order of N^3 . The $O(N)$ algorithms overcome this and the behavior has a linear scaling. The $O(N)$ algorithm (by using Divide and Conquer scheme) is applied for the Carbon Nanotube simulation and details of $O(N)$ TBMD algorithm is given. It is described that how a system is divided into many subsystems and how their contributions give overall system properties (such as charge density, band structure energy) by using nearsightness principle. In the Fig. IV.13, it is seen that our $O(N)$ algorithm scales linearly for increasing system size. The results obtained with $O(N)$ algorithm must be consistent with $O(N^3)$ results for the same system. To ensure, the value for the buffer size parameter must be investigated. The results for this

parameter are given in the Figs. IV.3 and IV.4. It is important to keep the buffer size parameter as small as possible and at the same time, it must be able to produce the same values with the $O(N^3)$ TBMD results. The another parameter in the simulation is the electronic temperature. We have investigated the effect of the electronic temperature on the MD simulation and obtained results are given in Fig. IV.2. Our $O(N)$ TBMD algorithm gives good energy band gap results for the 17x0 tube, but not so good for 10x10 tube with respect to proposed models mentioned above. On the other hand, the behavior of the local density of states graphs are (see Figs. IV.7–IV.10) as expected. We have concluded that the methodology is able to produce the physical properties such as Fermi-Dirac Distribution, local Density of States and energetics for the Carbon Nanotubes.

We have compared our $O(N)$ TBMD simulation results with $O(N^3)$ TBMD algorithm. Then parallelization technique is applied to $O(N)$ TBMD program. The parallel code is benchmarked and tested on a physical system, which is 10x10 structured CNT. The number of atoms are related to the increasing layers of 10x10 structured CNT, 4200 atom corresponds to 210 layered CNT (Å). Results for sequential and parallel runs are compared and assured that they are the same both in numerical accuracy and in physical aspects. Sequential $O(N^3)$ TBMD scales as cubic power to number of atoms and limited to system size around 600 atoms, however sequential $O(N)$ TBMD enables us to study system sizes around 900 atoms and also linearly scales as can be seen in Figure IV.13. Run time for parallel $O(N)$ TBMD code also scales as linearly

with the increasing number of atoms up to available system sources. Our result for Speed Up and Efficiency are given in Tables IV.2.2 and IV.2.2. The highest Speed up and Efficiency values are 3.71 and 0.98, respectively. Our results show that parallelization technique is beneficial because of the nature of the $O(N)$ algorithm. In present situation, parallelization together with $O(N)$ algorithm proves to be very effective and favorable.

The elastic properties of 10x10 carbon nanotube under tensile loading is investigated by using $O(N)$ Tight-Binding Molecular Dynamics method. The Young's modulus, tensile strength, Poisson ratio and frequency of vibrations are calculated and the values are 0.311 TPa, 4.92 GPa, 0.287 and 4.71×10^3 GHz, respectively. Our result is in the range reported in the literature. Although it is not at the high order of 1 TPa it still emphasizes a high Young's modulus and high strengths of Carbon nanotube. It is found that the elastic limit is at the strain rate 0.09 beyond this point tube becomes permanently changed. In Ref. [74], it is reported that when the strain larger than 0.10, the tube becomes softened. They also estimated the strain at failure for the SWNT as 0.17 whereas it is found as 0.23 in this study. The value for tensile strength found in this study is 4.92 GPa and seems to comparable with the experimental and theoretical results.

The calculated Poisson ratio is 0.287 and in good agreement with the available reported values which are 0.278, and 0.32. The evaluated frequency of vibration for the pristine (10x10) Carbon nanotube is 4.71×10^3 GHz which is very close to the value obtained from the experiment 4.94×10^3 GHz and

almost same with the value reported in the MD simulation by using a bond-order potential. It is reported that the frequency of vibration is insensitive to the strain rate and the frequency of vibration is identified as self-vibration. We have found that it is not constant and increasing strain rate decreases the vibration frequency.

An $O(N)$ Tight-Binding Molecular Dynamics (TBMD) algorithm in simulations of Single Wall Carbon Nanotubes (SWCNT) is developed. The algorithm is able to produce $O(N^3)$ TBMD results in good accuracy level. The problem of cubic scaling in $O(N^3)$ TBMD is overcome. Parallelization of the algorithm further speeds up the simulations. This also provides the increase in the system size. The usage of these two techniques together in the program enabled us to study very high system sizes with the available hardware. The results are remarkable such that the investigation of the stability, energetics and elastic properties of Carbon Nano Tubes became possible in PC structure in reasonable wall time and sizes. The evaluated total energy, radial distribution function, bond-length and bond-angle distribution functions, Fermi energy, band gaps, the Young's modulus, tensile strength, Poisson ratio and frequency of vibrations values are all in good agreement with those obtained from theory and experiment.

REFERENCES

- [1] V. Jamieson, *Physics World June*, 29 (2000).
- [2] S. Iijima, *Nature* **354**, 56 (1991).
- [3] S. Iijima and T. Ichlhashi, *Nature* **363**, 603 (1993).
- [4] D. S. Bethune, C. H. Kiang, M. S. de Vries, G. Gorman, R. Savoy, J. Vazquez, and R. Beyers, *Nature* **363**, 605 (1993). (1998).
- [5] P. M. Ajayan and T. W. Ebbesen, *Rep. Prog. Phys.* **60**, 1025 (1997).
- [6] N. Hamada, S. Sawada and A. Oshiyama, *Phys. Rev. Lett.* **68**, 1579 (1992).
- [7] X. Blase, L. X. Benedict, E. L. Shirley and S. G. Louie, *Phys. Rev. Lett.* **72**, 1878 (1994).
- [8] J. Tersoff and R. S. Ruoff, *Phys. Rev. Lett.* **73**, 676 (1994).
- [9] N. G. Chopra, L. X. Benedict, V. H. Crespi, M. L. Cohen, S. G. Louie, and A. Zettl, *Nature* **377**, 135 (1996).
- [10] R. E. Tuzun, D. W. Noid, B. G. Sumpter, and R. C. Merkle, *Nanotechnology* **7**, 241 (1996).
- [11] Y. A. Krotov, D. H. Lee, and S. G. Louie, *Phys. Rev. Lett.* **78**, 4245 (1997).
- [12] J. C. Slater and G. F. Koster, *Phys. Rev.* **94**, 1498 (1954).
- [13] W. A. Harrison, *Electronic Structure and the Properties of Solids*, (Dover, New York, 1980).
- [14] D. J. Chadi, *Phys. Rev. Lett.* **43**, 43 (1979).
- [15] W. M. C. Foulkes and R. Haydock, *Phys. Rev. B* **39**, 12520 (1989).
- [16] M. P. Allen, D. J. Tildesley, *Computer Simulation in Chemical Physics*, (Kluwer Academic Publishers, Amsterdam, 1993).
- [17] Heermann, D.W., *Computer Simulation Methods in Theoretical Physics*,(Springer-Verlag, Berlin 1990).

- [18] L. Colombo, *Comput. Mater. Sci.* **12**, 278 (1998).
- [19] S. J. Tans, M. H. Devoret, H. Dai, A. Thess, R. E. Smalley, L. J. Geerligs and C. Dekker, *Nature* **386**, 474 (1997).
- [20] J. W. G. Wildöer, L. C. Venema, A. G. Rinzler, R. E. Smalley and C. Dekker, *Nature* **391**, 59 (1998).
- [21] P. Löwdin, *J. Chem. Phys.* **18**, 365 (1950).
- [22] C. H. Xu, C. Z. Wang, C. T. Chan, K. M. Ho, *J. Phys.: Condens. Matter.* **4**, 6047 (1992).
- [23] <http://www.netlib.org>.
- [24] H. Schwichtenberg, G. Winter and H. Wallmeier, *Parallel Computing* **25**, 535 (1999).
- [25] A. Grama, V. Kumar and A. Sameh, *Parallel Computing* **24**, 797 (1998).
- [26] <http://www.epm.ornl.gov/pvm/>.
- [27] R. Murty and D. Okunbor, *Parallel Computing* **25**, 217 (1999).
- [28] P. Ordejon, *Comput. Mater. Sci.* **12**, 157 (1998).
- [29] C. S. Jayanthi, S. Y. Wu, J. Cocks, N. S. Luo, Z. L. Xie, M. Menon and G. Yang, *Phys. Rev. B* **57**, 3799 (1998).
- [30] D. R. Bowler, M. Aoki, C. M. Goringe, A. P. Horsfield and D. G. Pettifor, *Modelling Simul. Mater. Sci. Eng.*, **5**, 199 (1997).
- [31] W. Yang, *Phys. Rev. Lett.* **66**, 1438 (1991).
- [32] T. Zhu, W. Pan and W. Yang, *Phys. Rev. B* **53**, 12713 (1996).
- [33] T. Lee, J. P. Lewis and W. Yang, *Comput. Mater. Sci.* **12**, 259 (1998).
- [34] T. Hertel and G. Moos, *Phys. Rev. Lett.* **84**, 5002 (2000).
- [35] L. C. Venema, V. Meunier, Ph. Lambin, and C. Dekker, *Phys. Rev. B* **61**, 2991 (1998).
- [36] J.-C. Charlier, and Ph. Lambin, *Phys. Rev. B* **57**, R15037 (1998).
- [37] M. Ouyang, J. Huang, C. L. Cheung and C. M. Lieber, *Science* **292**, 702 (2001).
- [38] D. Brown, J. H. R. Clarke, M. Okuda, and T. Yamazaki, *Comput. Phys. Comm.* **86**, 312 (1995).
- [39] D. Brown, H. Minoux, and B. Maigret, *Comput. Phys. Comm.* **103**, 170 (1997).

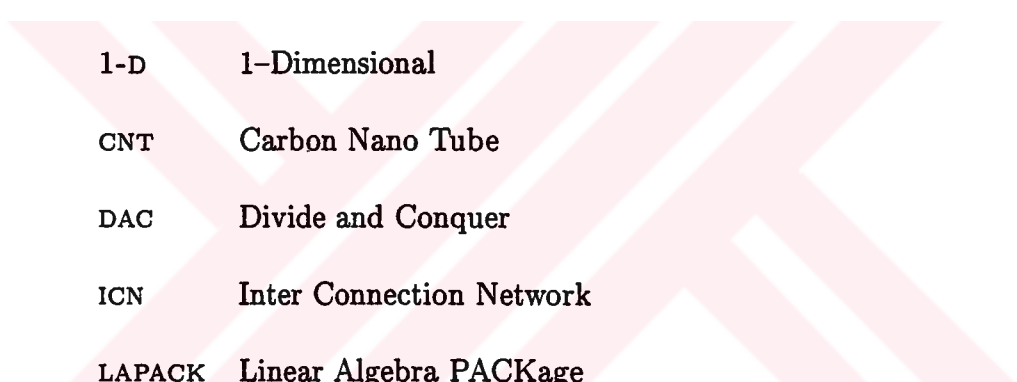
- [40] C. F. Cornwell, and L. T. Wille, *Comput. Phys. Comm.* **128**, 477 (2000).
- [41] J. Ilnytskyi, and M. R. Wilson, *Comput. Phys. Comm.* **134**, 23 (2001).
- [42] R. Saito, G. Dresselhaus, and M. S. Dresselhaus, *Physical Properties of Carbon Nanotubes*, (Imperial College Press, London, 1998).
- [43] D. Oh, J. M. Pank and K. S. Kim, *Phys. Rev. B* **62**, 1600 (2000).
- [44] S. Xie, W. Li, Z. Pan, B. Chang, L. Sun, *J. Phys. Chem. Solids* **61**, 1153 (2000).
- [45] M-F. Yu, O. Lourie, M. J. Dyer, K. Moloni, T. F. Kelly, and R. S. Ruoff, *Science* **287**, 637 (2000).
- [46] J.-P. Salvetat, J.-M. Bonard, N. H. Thomson, A. J. Kulik, L. Forró, W. Benoit, L. Zuppiroli, *Appl. Phys. A* **69**, 255 (1999).
- [47] Z. L. Wang, P. Poncharal, and W. A. de Heer, *J. Phys. Chem. Solids* **61**, 1025 (2000).
- [48] A. Thess, R. Lee, P. Nikolaev, H. Dai, P. Petit, J. Robert, C. Xu, Y. H. Lee, S. G. Kim, A. G. Rinzler, D. T. Colbert, G. E. Scuseria, D. Tománek, J. E. Fischer, and R. E. Smalley, *Science* **273**, 483 (1996).
- [49] M-F. Yu, B. S. Files, S. Arepalli, and R. S. Ruoff, *Phys. Rev. Lett.* **84**, 5552 (2000).
- [50] D. A Walters, L. M. Ericson, M. J. Casavant, J. Liu, D. T. Colbert, K. A. Smith, and R. E. Smalley, *Appl. Phys. Lett.* **74**, 3803 (1999).
- [51] J. R. Wood, M. D. Frogley, E. R. Meurs, A. D. Prins, T. Peijs, D. J. Dunstan, and H. D. Wagner, *J. Phys. Chem. B* **103**, 10388 (1999).
- [52] P. Poncharal, Z. L. Wang, D. Ugarte, and W. A. de Heer, *Science* **283**, 1513 (1999).
- [53] J.-P. Salvetat, G. A. D. Briggs, J.-M. Bonard, R.R. BACsa, A. J. Kulik, T. Stöckli, N.A. Burnham, L. Forró, *Phys. Rev. Lett.* **82**, 944 (1999).
- [54] A. Krishan, E. Dujardin, T. W. Ebbesen, P. N. Yianilos, and M. M. J. Treacy, *Phys. Rev. B* **58**, 14013 (1998).
- [55] A. D. Bozhko, D. E. Sklovsky, V. A. Nalimova, A. G. Rinzler, R. E. Smalley, J. E. Fischer, *Appl. Phys. A* **67**, 75 (1998).
- [56] M. R. Falvo, G. J. Clary, R. M. Taylor II, V. Chi, F. P. Brooks, Jr., S. Washburn, and R. Superfine, *Nature* **389**, 582 (1997).
- [57] E. W. Wong, P. E. Sheehan, and C. M. Lieber, *Science* **277**, 1971 (1997).

- [58] S. Iijima, C. Brabec, A. Maiti, and J. Bernholc, *J. Chem. Phys.* **104**, 2089 (1996).
- [59] M. M. J. Treacy, T. W. Ebbesen, and J. M. Gibson, *Nature* **381**, 678 (1996).
- [60] P. Calvert, *Nature* **357**, 365 (1992).
- [61] Z. Yao, C-C. Zhu, M. Cheng, J. Liu, *Compt. Mater. Sci.* **22**, 180 (2001).
- [62] V. N. Popov, V. E. van Doren, and M. Balkanski, *Phys. Rev. B* **61**, 3078 (2000).
- [63] G. Gao, T. Çağın, and W. A. Goddard III, *Nanotechnology* **9**, 184 (1998).
- [64] D. H. Robertson, D. W. Brenner, and J. W. Mintmire, *Phys. Rev. B* **45**, 12592 (1992).
- [65] B. I. Yakobson, C. J. Brabec, and J. Bernholc, *Phys. Rev. Lett.* **76**, 2511 (1996).
- [66] C. F. Cornwell and L. T. Wille, *Solid State Commun.* **101**, 555 (1997).
- [67] J. P. Lu, *Phys. Rev. Lett.* **79**, 1297 (1997).
- [68] G. V. Lier, C. V. Alsenoy, V. V. Doren, and P. Geerlings, *Chem. Phys. Lett.* **326**, 181 (2000).
- [69] E. Hernández, G. Goze, P. Bernier, and A. Rubio, *Appl. Phys. A* **68**, 287 (1999).
- [70] D. Sánchez-Portal, E. Artacho, J. M. Soler, A. Rubio, and P. Ordejón, *Phys. Rev. B* **59**, 12678 (1999).
- [71] D. Srivastava, M. Menon, and K. Cho, *Phys. Rev. Lett.* **83**, 2973 (1999).
- [72] T. Ozaki, Y. Iwasa, and T. Mitani, *Phys. Rev. Lett.* **84**, 1712 (2000).
- [73] G. Zhou, W. Duan, and B. Gu, *Chem. Phys. Lett.* **333**, 344 (2001).
- [74] Y. Xia, M. Zhao, Y. Ma, M. Ying, X. Liu, and L. Nei, *Phys. Rev. B* **65**, 155415-1 (2002).
- [75] L. G. Zhou, and S. Q. Shi, *Compt. Mater. Sci.* **23**, 166 (2002).
- [76] P. Zhang, P. E. Lammert, and V. H. Crespi, *Phys. Rev. Lett.* **81**, 5346 (1998).
- [77] E. Anglaret, S. Rols, and J-L. Sanvajol, *Phys. Rev. Lett.* **81**, 4780 (1998).
- [78] M. B. Nardelli, B. I. Yakobson, and J. Bernholc, *Phys. Rev. B* **57**, R4277 (1998).

- [79] B. I. Yakobson, *Appl. Phys. Lett.* **72**, 918 (1998).
- [80] E. Hernández, C. Goze, P. Bernier, and A. Rubio, *Phys. Rev. Lett.* **80**, 4502 (1998).
- [81] B. I. Yakobson, M. P. Campbell, C. J. Brabee, and J. Bernholc, *Comp. Mater. Sci.* **8**, 341 (1997).
- [82] J. M. Molina, S. S. Savinsky, and N. V. Khokhakov, *J. Chem. Phys.* **104**, 4652 (1996).
- [83] A. Lucas et al., *J. Phys. Chem. Solids* **54**, 587 (1993).
- [84] G. Overney, W. Zhong, and D. Tomanék, *Z. Phys. D: At. Mol. Clusters* **27** 93 (1993).
- [85] G. Adams et al., *Science* **256**, 1792 (1992).
- [86] M. Endo, *J. Mater. Sci.* **23**, 598 (1998).
- [87] H. O. Pierson, *Handbook of Carbon, Graphite, Diamond, and Fullerenes: Properties, Processing and Applications*, (Noyes Publications, Prak Ridge, NJ, 1993).
- [88] A. M. Rao, E. Richter, S. Bandow, B. Chase, P. C. Eklund, K. A. Williams, S. Fang, K. R. Subbaswamy, M. Melon, A. Thess, R. E. Smalley, G. Dresselhaus, and M. S. Dresselhaus, *Science* **275**, 187 (1997).
- [89] C. Özdoğan, G. Dereli, and T. Çağın, *Comp. Phys. Comm.* in print (2002).
- [90] F. W. Sears and G. L. Salinger, *Thermodynamics, Kinetic Theory, and Statistical Thermodynamics*, 3rd edition pp 302–362 (Massachusetts: Addison–Wesley 1986).

APPENDIX A

ACRONYMS



1-D	1-Dimensional
CNT	Carbon Nano Tube
DAC	Divide and Conquer
ICN	Inter Connection Network
LAPACK	Linear Algebra PACKage
LCAO	Linear Combination of Atomic Orbitals
LDOS	Local Density of States
MD	Molecular Dynamics
MIMD	Multiple Instruction Multiple Data
MISD	Multiple Instruction Single Data
MPI	Message-Passing Interface
MWCNT	Multi Wall Carbon Nano Tube
MWNT	Multi Wall Nano Tube
$O(N)$	Order-N

$O(N^2)$	Order- N^2
$O(N^3)$	Order- N^3
PC	Personel Computer
PBC	Periodic Boundary Conditions
PVM	Parallel Virtual Machine
SIMD	Single Instruction Multiple Data
SISD	Single Instruction Single Data
SM	Shared Memory
SWCNT	Single Wall Carbon Nano Tube
SWNT	Single Wall Nano Tube
TB	Tight-Binding
TBMD	Tight-Binding Molecular Dynamics

APPENDIX B

MAXWELL-BOLTZMANN VELOCITY DISTRIBUTION

B.1 The Distribution of Molecular Velocities

The first step is to calculate the partition function,

$$Z = \sum_j g_j \exp(-\mathcal{E}_j/kT) \quad (\text{B.1})$$

where \mathcal{E}_j is the energy and g_j is the degeneracy of each level.

$$\mathcal{E}_j = \frac{N_j^2 h^2 V^{-2/3}}{8m}, \quad n_j^2 = n_x^2 + n_y^2 + n_z^2 \quad (\text{B.2})$$

Total number of possible states in all energy levels up to and including the energy \mathcal{E}_j ,

$$G_j = \frac{1}{8} \left(\frac{4}{3} \pi n_j^3 \right) \quad (\text{B.3})$$

Total number of possible states between \mathcal{E}_j and $\mathcal{E}_j + \Delta\mathcal{E}_j$ (degeneracy of the macrolevel),

$$\Delta G_j = \frac{\pi}{2} n_j^2 \Delta n_j \quad (\text{B.4})$$

inserting the expressions for ΔG_j and \mathcal{E}_j , we have

$$Z = \sum_j \Delta G_j \exp(-\mathcal{E}_j/kT) = \frac{\pi}{2} \sum_j n_j^2 \exp\left(-\frac{h^2 V^{-2/3}}{8mkT} n_j^2\right) \Delta n_j$$

$$= \frac{\pi}{2} \int_0^\infty n_j^2 \exp\left(-\frac{h^2 V^{-2/3}}{8mkT} n_j^2\right) dn_j = V \left(\frac{2\pi mkT}{h^2}\right)^{3/2} \quad (\text{B.5})$$

The partition function therefore depends both on the temperature T and the volume V , which corresponds to the general extensive variable. The importance of the partition function Z is that in Maxwell-Boltzmann and classical statistics, all the thermodynamic properties of a system can be expressed in terms of $\ln Z$ and its partial derivatives. According to Maxwell-Boltzmann Distribution,

$$\Delta \mathcal{N}_j = \frac{N}{Z} \Delta G_j \exp(-\mathcal{E}_j/kT) \quad (\text{B.6})$$

where N is the total number of molecules with energies up to and including the energy \mathcal{E}_j ; $\Delta \mathcal{N}_j$ is the average occupation number of the macrolevel and

$$\mathcal{E}_j = \frac{n_j^2 h^2 V^{-2/3}}{8m} = \frac{1}{2} m v_j^2, \quad \Delta G_j = \frac{\pi}{2} n_j^2 \Delta n_j \rightarrow \Delta G_v = \frac{4\pi m^3 V}{h^3} n^2 \Delta v$$

It follows from these equations that, in velocity space,

$$\Delta \mathcal{N}_v = \frac{4N}{\sqrt{\pi}} \left(\frac{m}{2kT}\right)^{3/2} v^2 \exp\left(-\frac{mv^2}{2kT}\right) \Delta v \quad (\text{B.7})$$

The quantity \mathcal{N}_v represents the average total number of molecules with all speeds up to and including v , and $\Delta \mathcal{N}_v$ is the average number with speeds between v and v and Δv .

It is helpful to visualize the distribution in terms of 'velocity space'. Imagine that at some instant a vector v is attached to each molecule representing its velocity in magnitude and direction, and that these vectors are then transferred to a common origin, resulting in a sort of spiny sea urchin. The velocity of each molecule is represented by the point at the tip of the corresponding velocity vector. Fig. B.1 shows one octant of this velocity space. Geometrically

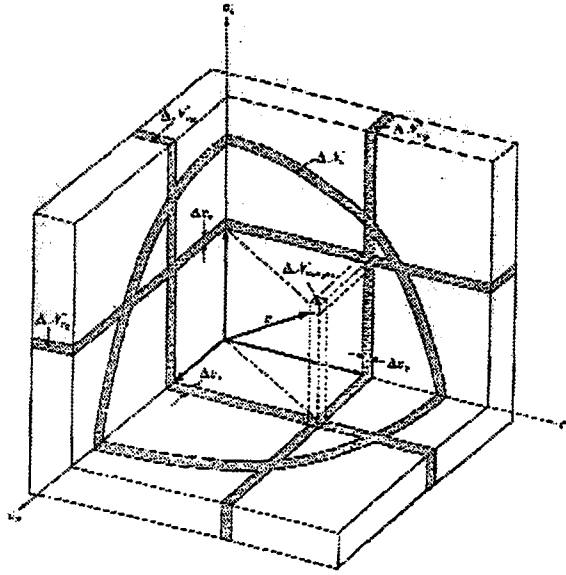


Figure B.1: Diagram of velocity space.

speaking, the quantity \mathcal{N}_v represents the average total number of representative points within a sphere of radius v , and $\Delta\mathcal{N}_v$ the number within a spherical shell of radius v and thickness Δv . The coefficient of $\Delta\mathcal{N}_v$ in Eq.(B.7), equal to the ratio $\frac{\Delta\mathcal{N}_v}{\Delta v}$, depends only on the magnitude of v , or on the speed. It is called the Maxwell-Boltzmann speed distribution function and is plotted as a function of v on Fig. B.2.

If velocity space is subdivided into spherical shells of equal thickness, the speed v_m at which the distribution function is a maximum is the radius of that spherical shell which includes the largest number of representative points. The speed v_m is called the most probable speed. To find its value, we take the first derivative of the distribution function with respect to v and set it equal to zero

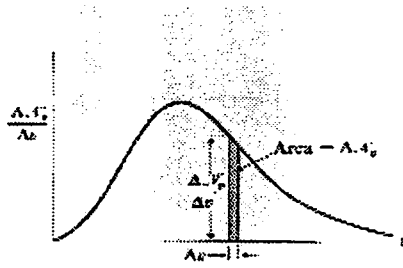


Figure B.2: Graph of Maxwell-Boltzmann speed distribution function.

$$dN_v/dv = 0.$$

$$v_m = \sqrt{\frac{2kT}{m}} \quad (\text{B.8})$$

The distribution function can now be expressed more compactly in terms of v_m ,

$$\Delta N_v = \frac{4N}{\sqrt{\pi}v_m^3} v^2 \exp\left(-\frac{v^2}{v_m^2}\right) \Delta v \quad (\text{B.9})$$

$$\frac{\Delta N_v}{\Delta v} = \frac{4N}{\sqrt{\pi}v_m^3} v^2 \exp\left(-\frac{v^2}{v_m^2}\right) \quad (\text{B.10})$$

Average or arithmetic mean speed is,

$$\begin{aligned} \bar{v} &= \frac{1}{N} \sum v \Delta N_v \\ &= \frac{4}{\sqrt{\pi}v_m^3} \int_0^{\infty} v^3 \exp\left(-\frac{v^2}{v_m^2}\right) dv = \frac{2}{\sqrt{\pi}} v_m = \sqrt{\frac{8kT}{\pi m}} \end{aligned} \quad (\text{B.11})$$

The root-mean-square speed is

$$\begin{aligned} v_{rms} = \sqrt{\bar{v}^2} &= \left(\frac{1}{N} \sum v^2 \Delta N_v\right)^{1/2} = \left(\frac{4}{\sqrt{\pi}v_m^3} \int_0^{\infty} v^4 \exp\left(-\frac{v^2}{v_m^2}\right) dv\right)^{1/2} \\ &= \frac{3}{2} v_m = \sqrt{\frac{3kT}{m}} \end{aligned} \quad (\text{B.12})$$

In summary, we have

$$v_m = \sqrt{\frac{2kT}{m}}, \quad v = \sqrt{\frac{2.55kT}{m}}, \quad v_{rms} = \sqrt{\frac{3kT}{m}} \quad (\text{B.13})$$

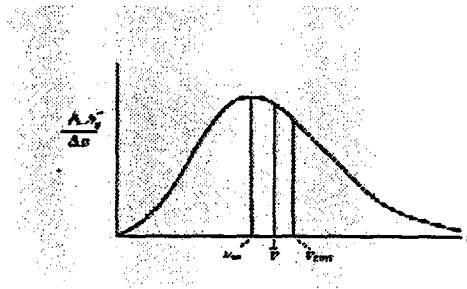


Figure B.3: Most probable (v_m), arithmetic mean (\bar{v}), and the root-mean-square (v_{rms}) speeds.

The three speeds are shown in Fig. B.3,

The relative magnitudes of the three, at a given temperature, are [90]

$$v_m : \bar{v} : v_{rms} \equiv 1 : 1.128 : 1.224.$$

B.2 Algorithm for Maxwell Velocity Distribution

– Setting initial velocities via randomly distribution of velocities around v_m

– According to the Kinetic Theory,

$$\frac{1}{2}mv^2 = \frac{3}{2}kT$$

It is needed to find the most probable velocity v_m , so using the relations,

$$\bar{v}^2 = \frac{3kT}{m}$$

$$v_{rms} = \sqrt{\bar{v}^2} = \sqrt{\frac{3kT}{m}}$$

$$v_m = \sqrt{\frac{2}{3}}v_{rms}$$

So, the expression for the most probable velocity v_m ,

$$v_m = \sqrt{\frac{2}{3}\bar{v}^2}$$

- Then normalization of this vector by dividing $\sqrt{3}$, that is the assumption of the radius of velocity space constituted by equal components in magnitude, giving the radius of the spherical shell which includes the largest number of representative points,
- Using a random number generator giving values $(-1, 1)$,

$$\text{Velocity Components} \equiv (v_{mean} - v_{mean} * \text{RandomNumber})$$

velocities (in all directions) distributed by using this procedure,

- Finding the averages values for each distributed velocity directions $\bar{v}_x, \bar{v}_y, \bar{v}_z$
- Dividing each components to radius vector which is, $((\bar{v}_x)^2 + (\bar{v}_y)^2 + (\bar{v}_z)^2)^{1/2}$, then finding direction cosines which are useful for scaling distributed velocities with respect to the given temperature
- Calculating kinetic energy and temperature with respect to the calculated v_m as,

$$\text{Kinetic Energy} \equiv \frac{1}{2}M\left(\frac{3}{2}v_m^2\right)$$

- Calculating the scaling factor,

$$(\text{Temperature given} / \text{Temperature calculated})^{1/2} \equiv \text{ScaleFactor}$$

- Redistributing the initial speeds with respect to scaling factor by multiplying each component by scale factor,

$$v_i = (|\vec{v}|) * ScaleFactor, \quad i = 1, 2, 3$$

- Subtracting from average values $v_i - \bar{v}_i$ gives differences from averages, these are new scales and adding to each component of each atom gives new speeds of each atom in each direction,
- Finding the averages for each distributed velocity directions $\bar{v}_x, \bar{v}_y, \bar{v}_z$ as,

$$v_i = \frac{1}{N} \sum_{\alpha}^N v_{\alpha}^i$$

- Finding the radius vector by,

$$v_m = ((\bar{v}_x)^2 + (\bar{v}_y)^2 + (\bar{v}_z)^2)^{1/2}$$

- Finding kinetic energy by,

$$Kinetic\ Energy \equiv \frac{1}{2} M \left(\frac{3}{2} v_m^2 \right)$$

- Finding calculated temperature,

$$TE_{calc} = \frac{KE_{calc}}{\frac{3}{2} k_B}$$

Since it has the same value with the given temperature, the initial velocities have been distributed successfully for each atom in all directions.

APPENDIX C

DETERMINATION OF ΔT

An equality for Δt can be found by using the equation;

$$x = (\Delta t)^2 * a = (\Delta t)^2 * F/m = (\Delta t)^2 * E/(x * m) \quad (C.1)$$

$$\Delta t = [x^2 * m/E]^{1/2} = ((10^{10} \text{ \AA})^2 * (1 \text{ amu} / 1.6605402^{-27}) / (eV/1.602^{-19}))^{1/2} \equiv \text{sec} \quad (C.2)$$

$$\text{sec} \equiv 9.822149929^{13} * (\text{\AA}^2 * \text{amu}/eV)^{1/2} = 9.822149929^{13} * \text{reducedunit}$$

$$\text{reducedunit} = 1.018050697^{-14} \text{ sec}$$

APPENDIX D

FLOWCHARTS OF THE PROGRAM

D.1 Sequential O(N) TBMD

-Initialization

-Creating Divide-and-Conquer Box

**-Diagonalizing the Hamiltonian Matrix to Find Initial Electronic
Density of States (eDOS) with respect to $O(N^3)$ Scheme**

-Divide and Conquer Scheme:

Computing Repulsive Forces and Energy, U_{rep}

From $i=1$ to Number of Cells

Computing O(N) Hamiltonian and diagonalization

Computing the band structure energy, E_{bs}

Calculating Chemical Potential for the Whole System

From $i=1$ to Number of Cells

Computing the Hellmann-Feynman Forces

-End of Divide and Conquer Scheme

-Computing Instantaneous Temperature, Kinetic Energy, Rescaling

Atomic velocities to Keep Temperature Constant

-Compute Total Energy per Atom, $E_T = U_{rep} + E_{bs} + E_{kin}$

-MD Loop, MD Time Step $\equiv 1$

Compute new positions $\vec{r}_i(n+1)$

Divide and Conquer Scheme

Compute new forces $\vec{F}_i(n+1)$ and accelerations $\vec{a}_i(n+1)$

Compute new velocities $\vec{v}_i(n+1)$

Computing Instantaneous Temperature, Kinetic Energy

Rescaling Atomic velocities to Keep Temperature Constant

Computing Pair Correlation Function and Radial Distribution Function

Computing Bond Angle Distribution and Atomic Coordination Number

Computing Bond Length Distribution

Compute Total Energy, $E_T = U_{rep} + E_{bs} + E_{kin}$

Saving Intermediate Configuration

Drawing Atomic Structure (PovRay),

$mds=mds+1$

-End of MD Loop, ($n \equiv$ MD time step; $i = 1, \dots, \text{Number of Atoms}$)

-Diagonalizing the Hamiltonian Matrix to Find Final Electronic

Density of States (eDOS) with respect to $O(N^3)$ Scheme

D.2 Parallel O(N) TBMD

-Master Node, Sending all necessary information to slaves

-Slave Node

-Divide and Conquer Scheme

Computing Repulsive Forces and Energy, U_{rep}

From $i=1$ to (Number of Cells/Number of Processors)

Computing O(N) Hamiltonian and diagonalization

Internode communication; Computing E_{bs}

Internode communication; Cal. Chemical Potential for the Whole System

From $i=1$ to (Number of Cells/Number of Processors)

Computing the Hellmann–Feynman Forces partially

Internode communication; Computing the Hellmann–Feynman Forces

End of Divide and Conquer Scheme

-Computing Instantaneous Temperature, Kinetic Energy, Rescaling

Atomic velocities to Keep Temperature Constant

-Compute Total Energy per Atom, $E_T = U_{rep} + E_{bs} + E_{kin}$

-MD Loop, MD Time Step $\equiv 1$

Compute new positions $\vec{r}_i(n+1)$

Internode communication; Updating Positions in each node

Divide and Conquer Scheme

Compute new forces $\vec{F}_i(n+1)$ and accelerations $\vec{a}_i(n+1)$

Compute new velocities $\vec{v}_i(n+1)$

Computing Instantaneous Temperature, Kinetic Energy

Rescaling Atomic velocities to Keep Temperature Constant

Computing Pair Correlation Function and Radial Distribution Function

Computing Bond Angle Distribution and Atomic Coordination Number

Computing Bond Length Distribution

Compute Total Energy, $E_T = U_{rep} + E_{bs} + E_{kin}$

Saving Intermediate Configuration

Drawing Atomic Structure (PovRay)

mds=mds+1

-End of MD Loop, ($n \equiv$ MD time step; $i = 1, \dots, \text{Number of Atoms}$)

VITA

Cem Özdoğan was born in Merzifon, Amasya on October 23, 1969. He received his B.S. degree in Physics from the Middle East Technical University in June 1994. He received his M.S. degree in Physics from the Middle East Technical University in June 1996. He worked as a research assistant from 1994 to 2001 in the department of physics, Kırıkkale University and Middle East Technical University. He is currently employed as instructor in the department of computer engineering, Çankaya University. His main areas of interest are electronic structure calculations, parallel computing and scientific computing.